Lithium Storage in Titania Films: Unification of Intercalation Electrode and Supercapacitor Concepts

Von der Fakultät Chemie der Universität Stuttgart
zur Erlangung der Würde eines

Doktors der Naturwissenschaften

(Dr. rer. nat.) genehmigte Abhandlung

Vorgelegt von

Chuanlian Xiao

aus Dalian, Liaoning, China

Hauptberichter:	Prof. Dr. Joachim Maier
Mitberichter:	Prof. Dr. Oliver Clemens
Prüfungsvorsitzender:	Prof. Dr. Frank Gießelmann

Tag der Einreichung:	22.05.2023
Tag der mündlichen Prüfung:	05.07.2023

Max-Planck-Institut für Festkörperforschung

Stuttgart

2023

To my family.

Erklärung über die Eigenständigkeit der Dissertation

Ich versichere, dass ich die vorliegende Arbeit mit dem Titel *Lithium Storage in Titania Films: Unification of Intercalation Electrode and Supercapacitor Concepts* selbständig verfasst und keine anderen als die angegebenen Quellen und Hilfsmittel benutzt habe; aus fremden Quellen entnommene Passagen und Gedanken sind als solche kenntlich gemacht.

Declaration of Authorship

I hereby certify that the dissertation entitled *Lithium Storage in Titania Films: Unification of Intercalation Electrode and Supercapacitor Concepts* is entirely my own work except where otherwise indicated. Passages and ideas from other sources have been clearly indicated.

Name/Name: Chuanlian Xiao

Unterschrift/Signed:

Datum/Date:

Contents

Zusammenfassung

Lithium-Batterien und Superkondensatoren, die beide auf electrochemischen Prozessen beruhen, sind unverzichtbare Komponenten in der heutigen mobilen und auf ständige Informationsverarbeitung angewiesenen Gesellschaft. Das grundlegende Konzept solcher Energiespeichertechnologien ist die Massenspeichung. In typischen Batterie-Interkalationselektroden wird die Kapazität durch den Einbau in das Volumen der elektroaktiven Partikel bestimmt. Dieser Prozess ist vergleichsweise gut untersucht und verstanden. Im Gegensatz dazu sind die Elektrodenprozesse von Superkondensatoren von der Speicherung an Grenzflächen dominiert, die experimentell auch intensiv bearbeitet werde. Die Bedeutung der Chemie der Ladungsträger (Defektchemie) ist jedoch insbesondere für die Grenzflächenspeicherung nicht hinreichend anerkannt. Daher werden Speicherung durch Volumeneinbau und Speicherung in Superkondensatoren meist als unabhängige Phänomene betrachtet, was diese beiden wichtigen Gebiete unnötigerweise getrennt erscheinen lässt.

Das Hauptthema der vorliegenden Arbeit ist daher die Vereinigung von Batterie- und Superkondensatorkonzepten mit Hilfe von TiO_2-Dünnfilmen als Musterbeispiel. Unser quantitatives Konzept der "job-sharing"-Speicherung wird dann zu einem Bild verallgemeinert, das Speicherung im Volumen wie auch in Raumladungszonen umfasst (Interkalationselektroden und Superkondensatoren).

Der erste Teil der Arbeit gibt einen Überblick über die klassische Raumladungstheorie und erweitert sie durch eine Diskretisierung der Raumladungszonen. Dies ist ein sinnvoller Ansatz, um große Raumladungspotentiale wie auch Nichtidealitäten in realistischen Festkörpersystemen wie den hier betrachteten Batteriesystemen zu behandeln. Ein Kontinuumsansatz ist nicht nur bezüglich interner Konsistenz fragwürdig, sondern auch wenn nahe der Grenzfläche sehr steile

Profile auftreten und analytische Korrekturen wenig hilfreich sind. In diesen Zusammenhang werden Raumladungsphänomene mittels Diskretisierung anstelle des analytischen Poisson-Boltzmann-Ansatzes untersucht. Die Kombination diskretisierter Modellierung mit eine Kontinuumsbeschreibung ergibt eine besonders leistungsfähige Methode, mit der Nichtidealitäten in den ersten Lagen (Variation der Struktur oder Dielektrizitätskonstante, elastische Effekte, Sättigungseffekte) direkt behandelt werden können. Zahlreiche praktisch relevante Beispiele von Funktionskeramiken werden diskutiert. Damit wird eine präziesere Definition und Abgrenzung von Elektroden- und Doppelschichtkapazität erzielt.

Der zweite Teil stellt den Hauptteil dar der Arbeit. Er befasst sich mit der Vereinigung von Volumen- und Grenzflächenspeicherung durch detaillierte Untersuchung des Lithiumeinbaus in Titandioxidfilme verschiedener Dicke auf unterschiedlichen Substraten. Dies ergibt ein umfassendes Bild der Ladungsträgerkonzentration als Funktion von Ortskoordinate, Zellspannung und Art des Substrats.

Zuerst wird die Herstellung und Charakterisierung der Materialien behandelt (TiO_2-Dünnfilme). TiO_2-Dünnfilme werden auf elektronen-akzeptierenden Substraten (Nb-dotierte $SrTiO_3$ (*N-ST*), undotiertes $SrTiO_3$ (*ST*), Fe-dotiertes $SrTiO_3$ (*F-ST*), Ruthenium) mit drei Methoden abgeschieden: atomic layer deposition (ALD), gepulste Laserdeposition (PLD), Molekularstrahlepitaxie (MBE). Die Filme werden mit Röntgenbeugung (XRD), Transmissionselektronenmikroskopie (TEM), Elektronenenergieverlustspektroskopie (EELS), Atomkraftmikroskopie (AFM) und Röntgenphotoelektronenspektroskopie (XPS) untersucht. Dies zeigt dass die abgeschiedenen TiO_2-Filme eine hohe Qualität und eine wohldefinierte Grenzfläche aufweisen. Die Filmdicke, einer der Schlüsselparameter, wird durch verschiedene Methoden (Röntgen-Reflektivität, TEM, Stiftprofilometrie) genau bestimmt.

Danach werden die Messungen der Batterie-Speicherkapazität der TiO_2-Dünnfilme durchgeführt. Sie werden durch Messungen des Wechselstromwiderstands und Gleichstommessungen mit DC-bias ergänzt, die Grenzflächenwiderstand und Grenzflächenkapazität liefern. Zusammen mit aberrationskorrigierter scanning-Transmissionselektronenspektroskopie (STEM) und Elektronenenergieverlustspektroskopie (EELS) werden somit unabhängige Informationen der Elektronen- und Lithiumverteilung erhalten.

Damit werden nicht nur Volumen- und Grenzflächenspeicherung präzise separiert, sondern sie können auch auf ein gemeinsames thermodynamische Konzept zurückgeführt werden. In der Tat kann das gesamte Profil einschließlich Volumen- und Grenzflächeneffekte durch Berücksichtigung nur weniger Materialparameter abgeleitet werden: die (freie) Energie der elektronischen Ladungsträger in TiO_2 und im Substrat wie auch die (freie) Bildungsenergie der Lithiumionen in TiO_2. Die Vereinigung der Konzepte von Interkalationselektrode und Superkondensator ergibt ein besseres Verständnis von elektrochemischen Energiespeichern, und mindert den Konflikt zwischen Energie- und Leistungsdichte, was insbesondere für nanoionische Systeme wichtig ist.

Abstract

Lithium intercalation batteries and supercapacitors are two indispensable components in nowadays' mobile, information-abundant society, which rely on electrochemical processes. The core concept of such energy storage technologies is mass storage. In typical insertion electrodes for batteries, the capacity is determined by bulk storage within the electroactive particles, which is comparatively well investigated and understood. In contrast, supercapacitor electrodes are dominated by interfacial storage at interfaces, which is well addressed experimentally. However, the charge carrier chemistry (defect chemistry) especially in the latter case is not fully acknowledged. Consequently, the intercalation storage and supercapacitive storage are usually considered as independent phenomena and the two important fields appear to be unnecessarily separated.

Therefore, the core of the present thesis is unifying battery and supercapacitor concepts using TiO_2 thin films as master example. Following and extending our quantitative concept of job-sharing storage, a generalized picture that includes bulk and space charge storage (intercalation electrode and supercapacitor storage) is developed.

The first part of the thesis reviews the classic space charge theory and extends it in terms of discrete modeling of space charge zones in solids, which is a sensible approach for handling pronounced space charge potentials as well as non-idealities in realistic solid state systems such as the battery system under concern in this thesis. In addition to issues of internal consistency, the continuum approach is questionable if extremely steep profiles close to the interface occur, and analytical corrections are not very helpful. In this context, the space charge behavior is studied in a discretized manner rather than by using the analytical Poisson-Boltzmann function. Combining discrete modeling with the continuum description provides a particularly powerful method, with the help

of which non-idealities in the first layers (variation in structure, elastic effects, saturation effects, changes in dielectric constant) are directly addressed. Various examples of practical value for functional ceramics are discussed. In this way a more precise definition and demarcation of electrode and double layer capacity is achieved.

The second part of the thesis, which is in fact the core part, investigates the unification of bulk storage and interfacial storage by carefully investigating the storage of lithium in titania films on various substrates as a function of thickness. The full picture in terms of charge carrier concentrations as function of spatial coordinate with cell voltage and substrate conditions as parameters is obtained.

First, materials (TiO_2 thin films) preparation and characterization are addressed. TiO_2 thin films on various electron-accepting substrates (Nb doped $SrTiO_3$ (*N-ST*), undoped $SrTiO_3$ (*ST*), Fe doped $SrTiO_3$ (*F-ST*), Ruthenium) were deposited utilizing three methods: atomic layer deposition (ALD), pulsed laser deposition (PLD) and molecular beam epitaxy (MBE). The substrates and the deposited films were characterized by x-ray diffraction (XRD), transmission electron microscopy (TEM), electron energy loss spectroscopy (EELS), atomic force microscopy (AFM) and X-ray photoelectron spectroscopy (XPS), which show that the grown TiO_2 films are of good quality with sharp interface. Film thickness (one of the key parameters) was determined precisely using various techniques (x-ray reflectivity, TEM, stylus profilometry).

Second, the battery storage capacity measurements of TiO_2 thin films are supplemented by bias dependent impedance measurements, yielding interfacial resistance as well as interfacial capacitance. Combining with aberration-corrected scanning transmission electron microscopy (STEM) and electron energy loss spectroscopy (EELS) measurements, independent information on electron and Li distribution is obtained.

As a result, not only bulk and boundary storage contributions are precisely deconvoluted, but they can be traced back to a common thermodynamic conception. In fact, the entire profile including interfacial and bulk effects is derived by taking account of only a few bulk materials parameters: the (free) energies of the electronic carriers in TiO_2 and the substrate as well as the formation (free) energy of the Li-ions in TiO_2. Unifying intercalation electrode and supercapacitor concepts provides a way of better understanding and mitigating the energy and power density conflict of storage devices, which becomes particularly important for nanoionic systems.

1
Introduction

1.1 Intercalation and Space Charge Storage

The importance of energy storage is becoming more and more prominent in the context of dramatic climate changes associated with high CO_2 emission. Simultaneously, the search for clean and efficient energy storage devices (e.g., lithium intercalation batteries and supercapacitors) has been increasing in the last decades. The core concept of the related electrochemical processes in energy storage devices is mass storage. Therefore, the understanding of mass storage is not only fundamentally important for comprehending storage processes but also technologically of relevance in guiding on developing powerful energy storage devices.

Lithium intercalation batteries are among the most significant technological advancements of recent decades and are vital for nowadays' energy household. They are particularly useful in applications related to powering portable electronic devices (cellphones, laptops, computers etc.), storing electricity from renewable sources (storage of wind/solar power), and as essential component in new hybrid electric vehicles (*1-3*). In addition, they are also being considered for grid-storage purposes due to their high capacities. The practical importance of these batteries was recognized with the awarding of the 2019 Chemistry Nobel Prize for the invention of the rocking chair battery, which uses Li-cobaltate and graphite as intercalation electrodes (*4*, *5*). Despite all of this, the charge carrier situation (point defect chemistry) of electrodes (the principles of defect-chemistry for treating mixed conductors) remains inadequately addressed (*6*).

The typical insertion electrodes for batteries are both ionically and electronically conductive. Ions penetrate from the electrolyte side into electrode, electrons from the current collector side. Ions and electrons are incorporated into electrodes, which allows the entire volume of the storage

electrode to be chemically capacitive (see Fig. 1.1). Most of the capacity is contributed by bulk storage within electroactive particles, providing a high energy density, while the corresponding power density is lowered owing to the necessary chemical diffusion process.

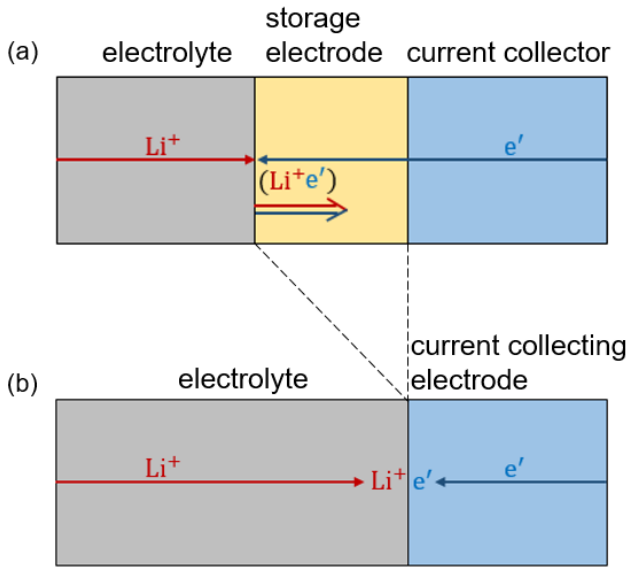

Fig. 1.1 Sketch of (a) bulk storage (in a predominantly electronically conducting electrode) and (b) supercapacitive storage (at electrolyte/current-collecting electrode interface). In the general case of a mixed conductor, both processes occur simultaneously.

Fig. 1.2 shows the potential distributions (the electric (ϕ), chemical (μ) and electrochemical potentials ($\tilde{\mu}$)) of a Li-based battery for single-phase electrodes and electrolyte (simplified battery cell) under open-circuit conditions, which also includes built-in space charge effects (electrode/electrolyte interfaces). For the details about the principles of constructing the profiles and the detailed discussions, one could refer to Refs. (*7*, *8*).

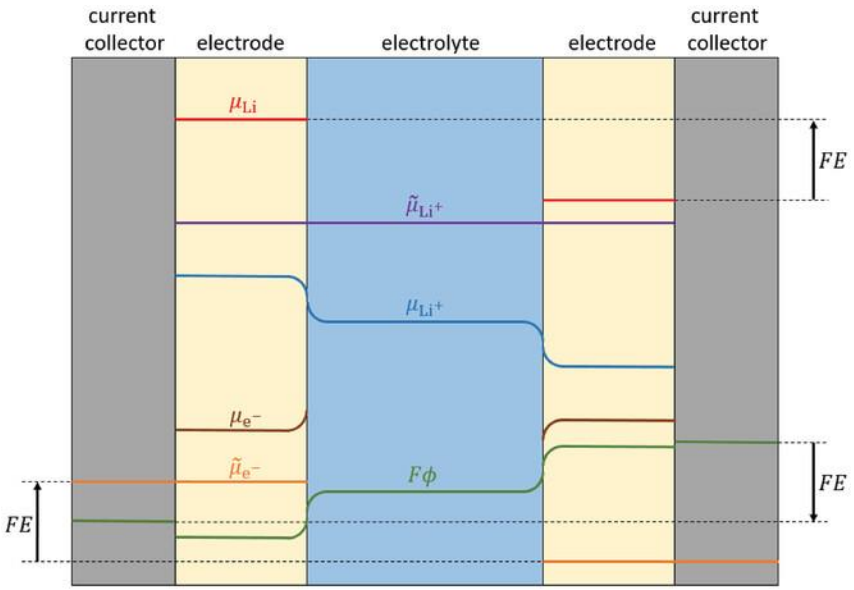

Fig. 1.2 Sketch of the chemical, electric, and electrochemical potentials in a simplified battery cell under open-circuit conditions, including built-in space charge effects. Electrolyte and electrodes are thermodynamically compatible. According to Ref. (*8*).

When discussing mechanisms of mass storage in solids (e.g., typical battery electrode), there are three storage modes in solids that need to be distinguished (Fig. 1.3, see Ref. (*6*)). The first mode is single phase storage (e.g., Li storage in TiS_2 or $LiCoO_2$), which is based on dissolution (as shown in Fig. 1.3a). The bulk storage occurs through the occupation of interstitial or vacant sites (by addition rather than by substitution), which is typically referred to as insertion (If these interstitial sites are between defined layers, it is known as intercalation). The second mode of storage occurs via phase transformations, comprising phase change reactions (such as $FePO_4/LiFePO_4$) and decomposition reactions (such as $LiCoO_2$ decomposing to Co and Li_2O on excessive lithiation, which is also referred to as a proper conversion reaction), a distinction that is important from a kinetic point of view. The third storage mode is referring to charge storage at higher-dimensional defects (in particular at interfaces), which is possible even in the case of an ideal abrupt two-phase contact ("job-sharing" mechanism, see section 1.2).

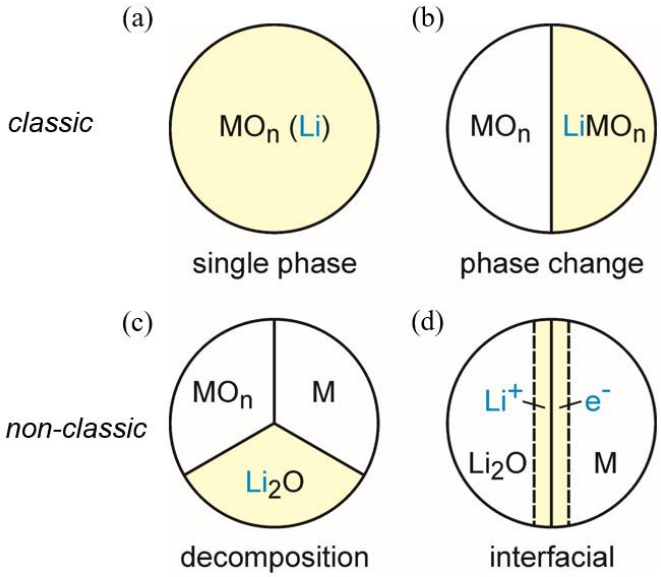

Fig. 1.3 The mass storage mechanisms. According to Ref. (*6*). The reason for distinguishing between (b) and (c) is the fundamentally different kinetics.

In terms of supercapacitors (*9*), the charging is restricted to the interface and no bulk chemical diffusion is required, leading to higher power densities but lower energy densities (*10-17*) (see Fig. 1.1), which is also well addressed experimentally by a different community. However, the principles of defect chemistry have been inadequately incorporated in addition to the systematical job-sharing storage study (see section 1.2). As a consequence of the lack of an adequate defect-chemical and nanoionic picture, the two storage modes are considered to be independent phenomena unnecessarily.

Supercapacitor electrodes are dominated by interfacial storage at interfaces. In its original form, supercapacitors rely entirely on electrical polarization, resulting in the formation of two opposing double layers at the two electrode-electrolyte interfaces. The electrode in this case serves solely as an electronic conductor, while mass conservation within the electrolyte is maintained. In fact, there exist variations of supercapacitive storage where a Faradaic electrode reaction takes place, in which only interfaces are affected (*18-23*). Such pseudocapacitors may exhibit even higher capacities.

1.2 Thermodynamics of Mass Storage at Interfaces

The concept of interfacial effects in solid-state ionics can be traced back to the 1970s. Liang (*24*) was the first to observe a conductivity increase in a LiI electrolyte when mixing it with some amount of insulating particles of Al_2O_3. The unusual conductivity behavior of such composite electrolytes was later explained by Maier through the concept of space charge (*25*), which is attributed to the local adsorption of Li^+ on the surface of Al_2O_3, leading to compensation by a high concentration of lithium ion vacancies in the space charge regions at the LiI/Al_2O_3 interfaces. This formed the starting point of a whole "zoo" of experimental and theoretical "anomalies" which are based on ionic redistribution phenomena at interfaces (*26*). In recent decades, the investigation of interfacial phenomena in terms of transport, and more recently also in terms of storage (*6*) has greatly advanced the progress of solid-state ionics.

If we consider the ensemble of electronically conducting and ionically conducting phases as a composite electrode (*6, 27*), excess storage can then be viewed similarly to composite electrolytes in terms of transport (*28*). Storage of lithium ($Li^+ + e^-$) can occur in a job-sharing manner in a composite electrode containing an electron conductor that cannot accommodate the Li-ions, and an ion conductor that cannot host the electrons. In other words, transport and accommodation of ions take place in one phase (ionic conductor), and that of electrons in the other phase (electronic conductor). As evidenced by various examples including Li_2O:Ru, LiF:Ni and $RbAg_4I_5$:C (*29-33*), such storage can be substantial and rapid. Evidence was derived primarily from impedance measurements and elucidation of activity dependence, and recently direct magnetometric evidence was reported (*34, 35*). A charge-discharge curve fully covering the deficient and excess parts of the storage can be measured for $RbAg_4I_5$:C. In fact, the job sharing mechanism provides a way to construct an artificial mixed conductor electrode that has the potential to achieve both high energy density and high power density (*27*) if the sizes involved are mesoscopic, which is analogously to artificial electrolytes obtained in the nanoionic CaF_2-BaF_2 system (*36*). In addition, the predicted finding that the Li_2O-Ru composite can also synergistically store hydrogen (*37*) via such job-sharing gives more obvious evidence. More importantly, this conception enables us to treat storage thermodynamics and kinetics within the framework of point-defect chemistry.

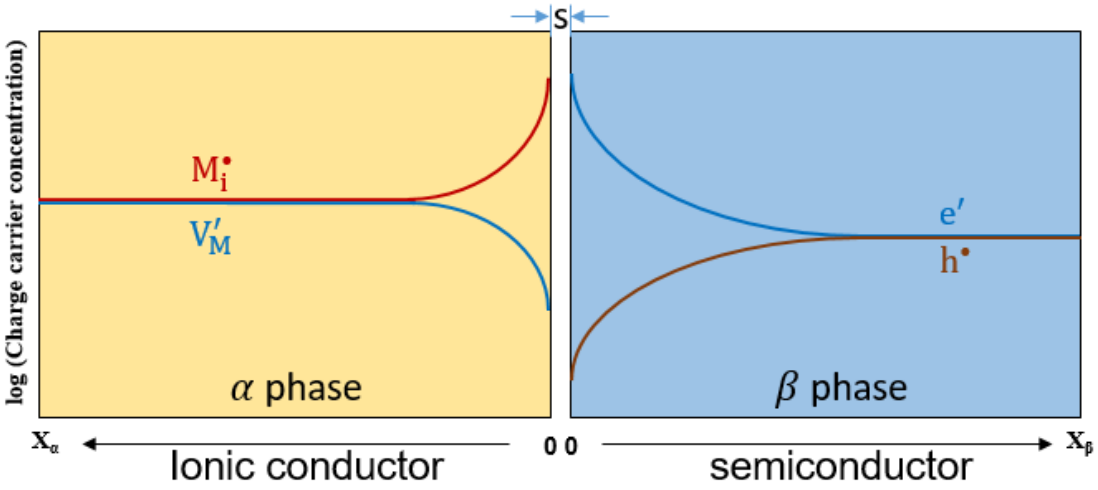

Fig. 1.4 Schematic of interfacial storage at a weakly disordered ionic conductor / weakly disordered semiconductor junction.

Let us consider an abrupt junction of two phases: phase α (weakly disordered ionic conductor with metal ion interstitials $M_i^{\cdot}$ and metal ion vacancies V_M' as charge carriers) and phase β (weakly disordered semiconductor with electrons e' and holes $h^{\cdot}$ as charge carriers) (Fig. 1.4). The point defects are described using the Kröger-Vink notation where dots and dashes refer to relative charges. For simplicity, only monovalent defects ($M_i^{\cdot}, V_M', e', h^{\cdot}$) are focused on and their respective concentrations are denoted as c_i, c_v, c_n, and c_h, respectively.

When Frenkel defects in phase α are considered, then

$$M_M + V_i \leftrightharpoons M_i^{\cdot} + V_M' \tag{1.1}$$

where M_M and V_i represents a cation occupying its regular site and a vacancy located at the interstitial site, respectively. Then a mass action law applies with Frenkel constant K_F (for dilute conditions)

$$K_F = c_i(x_\alpha)c_v(x_\alpha) \tag{1.2}$$

On the other hand, we need to consider the equilibrium of electronic disorder in phase β (semiconductor with electrons and holes), then

$$Nil \leftrightharpoons e' + h^{\cdot} \tag{1.3}$$

Neglecting activity coefficients, an analogous mass action law is applied

$$K_B = c_n(x_\beta)c_h(x_\beta) \tag{1.4}$$

Regarding the actual interface, a simpler approximation would be to consider a region without charge and a linear electrical potential change (cf. Refs. (*38, 39*)). Over the charge free zone an electrochemical equilibrium comprising defects in both phases holds

$$M \leftrightharpoons M_i^{\cdot}(x_\alpha = 0) + e'(x_\beta = 0) \tag{1.5}$$

The electrochemical equilibrium follows from the balance of the electrochemical potentials ($\tilde{\mu}_m$) of each species *m*

$$\tilde{\mu}_M = \tilde{\mu}_{M_i^{\cdot}} + \tilde{\mu}_{e'} \tag{1.6}$$

Then a third mass action law is obtained if we still consider the dilute situation

$$\frac{c_i(0)c_n(0)}{a_M} = K_M \times \exp\left(\frac{-F(\phi_\alpha(0) - \phi_\beta(0))}{RT}\right) \tag{1.7}$$

where a_M is the activity of species *M*, K_M mass action constant for *M* storage, and $(\phi_\alpha(0) - \phi_\beta(0)) = \Delta\phi_0$ the electrical potential drop over the charge free contact zone.

Coupling with Poisson's equation and global electroneutrality, the storage capacity Q as a function of activity (voltage) can be predicted as

$$a_M = \frac{\left(Q + \sqrt{Q^2 + 8\varepsilon_\alpha\varepsilon_0 RT\sqrt{K_F}}\right)^2 \left(Q + \sqrt{Q^2 + 8\varepsilon_\beta\varepsilon_0 RT\sqrt{K_B}}\right)^2}{64K_M\varepsilon_\alpha\varepsilon_\beta(\varepsilon_0 RT)^2} e^{\frac{FsQ}{\bar{\varepsilon}\varepsilon_0 RT}} \tag{1.8}$$

where $\bar{\varepsilon}$ is the mean relative permittivity of the two phases. For other types of contacts, different power laws (storage capacity Q as a function of activity) can be derived in an analogous way (i.e., coupling Poisson's equation and global electroneutrality with equilibrium of defect reactions). (For more details, please see Refs. (*7, 40*)).

The essence of the present thesis aims at fully understanding bulk and boundary charge carrier chemistry, which allows us to unify intercalation electrode and supercapacitor conceptions by considering equilibrium storage as a function of position. In Chapter 2, the classic space charge

theory is reviewed and its shortcomings are discussed. The extensions of space charge theory in terms of discrete modeling of space charge zones in solids are addressed, which is a sensible approach for handling pronounced space charge potentials as well as non-idealities in realistic solid-state systems such as the battery system under concern in this thesis. Chapter 3 covers experimental details of preparation and characterization of model material (TiO_2 thin films).

The core part (unification of intercalation electrode and supercapacitor concepts) will be presented in Chapter 4, where results from electrochemical measurements (electrochemical storage measurements: thickness dependence, different storage degrees, substrate effects; electrochemical impedance measurements) supplemented by independent electron microscope measurements (STEM and EELS) are discussed and shown to lead to a common picture of bulk and boundary effects and thus of intercalation and supercapacitive storage conceptions. The electrochemical and thermodynamic analysis is fully corroborated by advanced electron microscopy, which maps electron as well as ion distribution. The conclusion and perspective will be discussed in Chapter 5. Not only may the unification of two concepts be fundamentally important and the basis of a synergistic bringing together different scientific communities, but also of synergistically exploiting mutual advantages of intercalation electrodes and supercapacitors as regards power and energy density.

2

Space Charge Theory

2.1 Literature Background: Classic Space Charge Theory

Whenever interfaces in charge-carrier containing systems are involved, electroneutrality is broken and individual charge carrier redistribution, be it electronic or be it ionic, occurs (at the cost of and balanced by a back-driving electric field).

The investigation of space charge zones typically involves the use of the classic continuum model known as the Gouy-Chapman model, which was originally developed for liquid electrochemistry. The interface between a surface (e.g., metal surface) and liquid electrolyte (including counterions) results in charge separation, which competes with thermal effects favouring a more uniform distribution of ions. The accumulation of counterions near the electrode surface, along with the depletion of co-ions (with an associated electric field), is known as the electric double layer (EDL) (Fig. 2.1).

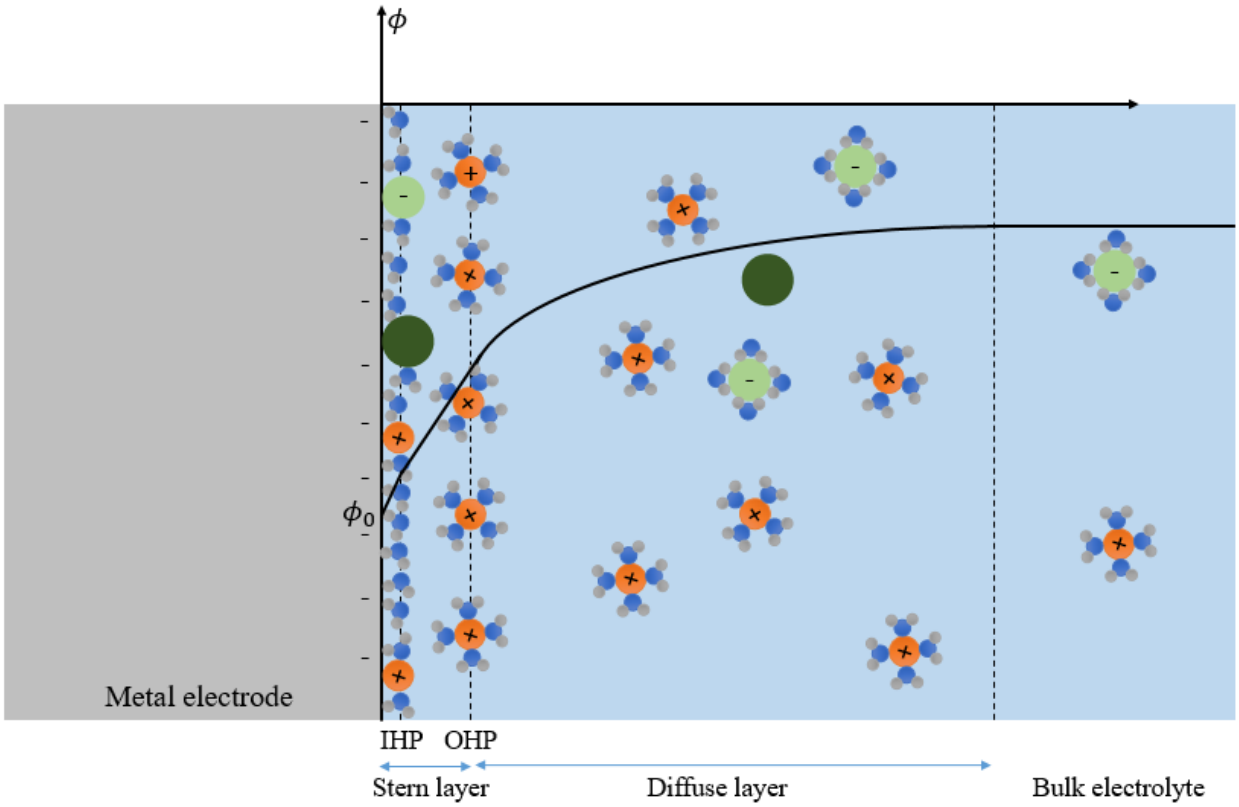

Fig. 2.1 Classical mean-field description of the electrical double layer. Schematic description of the Gouy–Chapman–Stern model. IHP stands for the inner Helmholtz plane, OHP for the outer Helmholtz plane. The orange, light green and dark green spheres represent the cations, the anions and neutral species, respectively.

Fig. 2.2 summarizes the main timeline of space charge theory. The concept of classic EDL was first introduced by Helmholtz in 1853 (*41*), who proposed a model to describe the distribution of charges at the interface between a conductor and electrolyte solution as a parallel - plate capacitor (with equal but opposite charges, Helmholtz layer). One plate corresponds to the conductor surface with negative charge, while the other one corresponds to the plate containing all the positive charge, between which the potential decreases linearly (*41*, *42*). The Helmholtz model often provides a reasonable estimate for the EDL, and, therefore, commonly serves as a useful rule of thumb in practical application. In early twentieth century, Gouy and Chapman independently described the inhomogeneous distributions of ionic species near an electrode surface in 1910 (*43*) and 1913 (*44*), respectively, using the Poisson-Boltzmann (PB) theory (interplay of electrostatics and thermal randomization), which leads to a potential that decays exponentially as one moves away from the surface. Consequently, the charges are not restricted to a single layer, but instead spread out over

a finite thickness, which is commonly referred to as the diffuse layer. This mean-field description makes certain assumptions, including that (1) the surface is uniform laterally, and the distribution of charges can be represented by their average position in the plane of the interface; (2) the charged surface is sharp; (3) water behaves as a homogeneous dielectric medium; (4) ions are point charges and interact solely through Coulombic forces; and (5) there are no interactions between ions. One decade later, Debye and Hückel proposed a linearized solution to the P-B distribution (*45*), which is valid for small potentials. Despite its assumptions of low potentials, it can still well predict the behavior of highly charged surfaces due to counterions condensing near the surface, effectively reducing the surface charge.

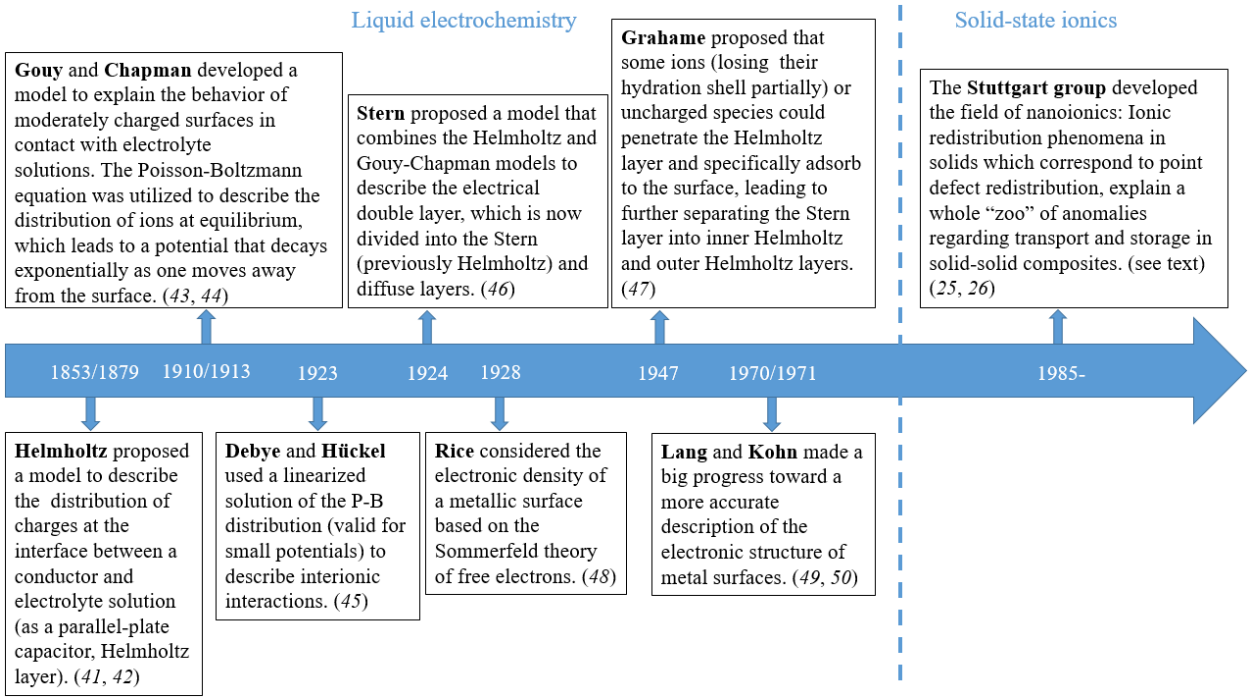

Fig. 2.2 Timeline of space charge theory in liquid electrochemistry and solid-state ionics.

One year later, Stern proposed a model that combines the Helmholtz and Gouy-Chapman models to describe the electrical double layer, which is now divided into the Stern (previously Helmholtz) and diffuse layers (*46*), because the Gouy-Chapman model was inadequate in explaining capacitance measurements at high charges or potentials. This model takes into account the finite size of ions and their possible hydration. After another two decades, Graham extended the Stern model by proposing that some ions (losing their hydration shell partially) or uncharged species

could penetrate the Helmholtz layer and specifically adsorb to the surface (*47*), leading to further separating the Stern layer into inner Helmholtz and outer Helmholtz layers (Fig. 2.1). They are the locus of the centers of the specifically adsorbed ions and the locus of the centers of the non-specifically adsorbed hydrated ions, respectively.

Regarding the electrode side, Rice firstly considered the electronic density of a metallic surface based on the Sommerfeld theory of free electrons in 1928 (*48*). After decades, Lang and Kohn made a big progress toward a more accurate description of the electronic structure of metal surfaces (*49*, *50*) (see Fig. 2.3).

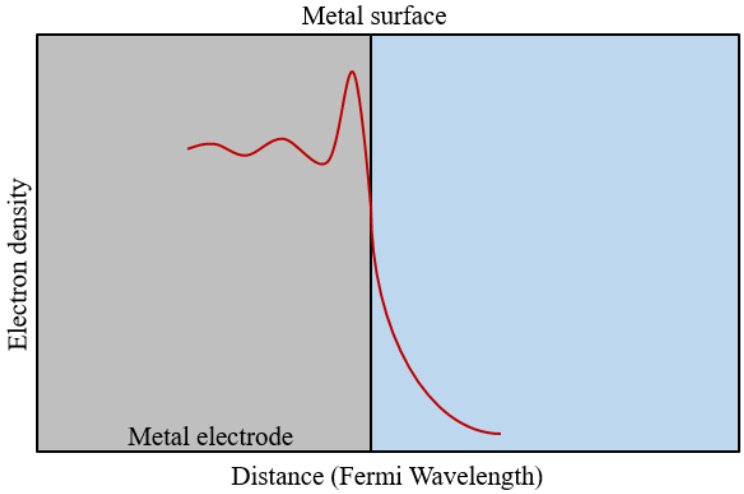

Fig. 2.3 Sketch of charge density near metal surface.

Such space charge situations are ubiquitous, which does not only hold for rather classic systems in the field of semiconductors (*51*) or liquid state electrochemistry (*52*). It has also been shown to be of great relevance for solid-state ionics. As mentioned in Chapter 1 (introduction of mass storage at interfaces), Maier explained the unusual conductivity behavior of Liang's observation (*24*) (LiI/Al_2O_3) through the concept of space charge (*25*), which comes the starting point of a whole "zoo" of experimental and theoretical "anomalies" which are same on ionic redistribution phenomena at interfaces (*26*). In recent decades, it is practically relevant in the context of solid electrolytes (interfaces with electrodes (*53*), grain boundaries (*54*), composite electrolytes (*28*)) or of mixed conductors, which could be used for storage (*55*), sensing (*56*), catalysis (*57*) and many other purposes. In the case of storage electrodes, one deals with grain boundaries, contacts to electrolyte or the respective passivation layers and contacts with current collectors (*27*). Space

charge effects can not only explain various interfacial phenomena, they can also be used to generate beneficial effects. Such effects can refer to resistive, but also storage anomalies (*27*, *28*).

The space charge effects have gained significant attention in recent years due to their essential role in electrochemical energy storage and chemical conversions. As a result, it has become a focal point of both fundamental and applied research in a variety of fields, including chemistry, physics, materials chemistry and various engineering disciplines.

2.2 Discrete Modeling of Ionic Space Charge Zones in Solids

Over the last century, significant research has been focused on investigating the behavior of charged interfaces in contact with electrolytes. While in some instances, these classic models have proven to be sufficient, in many cases, they have been quantitatively inaccurate or qualitatively unsuitable. The shortcomings of the classic continuous models are discussed in the following text.

2.2.1 Introduction

The generalized thermodynamic contact picture, as shown in Fig. 2.4, considers both ionic and electronic redistribution and their coupling via the chemical potential of components. This is mirrored by, e.g., oxygen partial pressure over oxides (*58*); Li-activity in battery electrodes (*29*) etc.

When considering full equilibrium, the combination of Poisson's equation and Boltzmann distribution leads – in the continuum picture – to Gouy-Chapman profiles (*40*) (while depletion of mobile majority carriers in doped systems leads to Mott-Schottky profiles (*7*)). However, the profiles can be very steep if the interfacial effects are pronounced particularly in the first case, and very often the majority of the charge decays within a distance that is on the order of the interatomic spacing, reflecting the overstretching of the continuum approach. In fact, in the continuum model, the total charge stored in the space charge layer (Q) is proportional to the square root of the concentration of the outmost position ($x = 0$ in Fig. 2.4a) rather than to the concentration in the outmost layer ($x' = 0$ in Fig. 2.4b). Discrepancies are obvious not only for space charge conduction (*59*) but also for space charge storage (*40*). Fig. 2.5 gives a striking example in the case

of interfacial storage, where the power law between the amount of stored charge and the activity of the component fails qualitatively in the continuum picture in contrast to discrete modeling (*40*). These differences emphasize that there is no straightforward match between reality and continuum models. More importantly, elastic, structural or saturation effects as well as permittivity variations in realistic solid system cannot easily be involved in the continuum approach.

It is also well-known from liquid electrochemistry that the calculated space charge capacitance is much smaller than the measured one and needs to be corrected by a rigid capacitance contribution that is more or less based on the finite atomic spacing of charge and counter charge (Fig. 2.4a) (see e.g., Ref. (*52*)).

In addition, another fundamental weakness of the classic theory comes from the inconsistency of the Poisson-Boltzmann equation. As shown in Refs. (*60, 61*) the results of the Poisson-Boltzmann equation contradict the superposition principle of electrostatics (potentials due to individual ions can be linearly superimposed to yield the potential due to an assembly of ions) which originates from the linear Poisson's equation. The problems are remedied in the Debye-Hückel approximation $e^{\pm\psi} \approx 1 \pm \psi$, i.e. for small ψ, whilst otherwise there is an inconsistency in combining the non-linear Boltzmann equation with the linear Poisson-equation (*60*).

The deeper reason of the inconsistency is the identification of the mean potential appearing in Poisson's equation (potential not changed by a spy-particle) with the potential of mean force appearing in the electrochemical potential and thus in the Boltzmann expression (potential referring to the distribution that self-consistently includes the particle). The inconsistency is also revealed by the fact that the Debye and the Güntelberg charging processes lead to different results. The differences disappear at low potentials since here interactions are negligible. The differences between both types of potentials may also become less relevant at very high field as there the contribution of the particle is expected to be less relevant according to Ref. (*65*).

As the Taylor expansion of the Poisson-Boltzmann equation shows, the validity of the exponential solution extends to greater ψ for symmetrical electrolytes as here the quadratic terms cancel.

More accurate descriptions of concentrated electrolytes are given by Mayer et al. (*62*), and Allnatt et al.(*63-65*), but may become soon very intransparent and not manageable. In this thesis, the classic Poisson-Boltzmann equation is accepted but treated in a discrete manner to be more

realistic and to leave the room for structural modifications. For more details the reader is referred to literature (*60-70*).

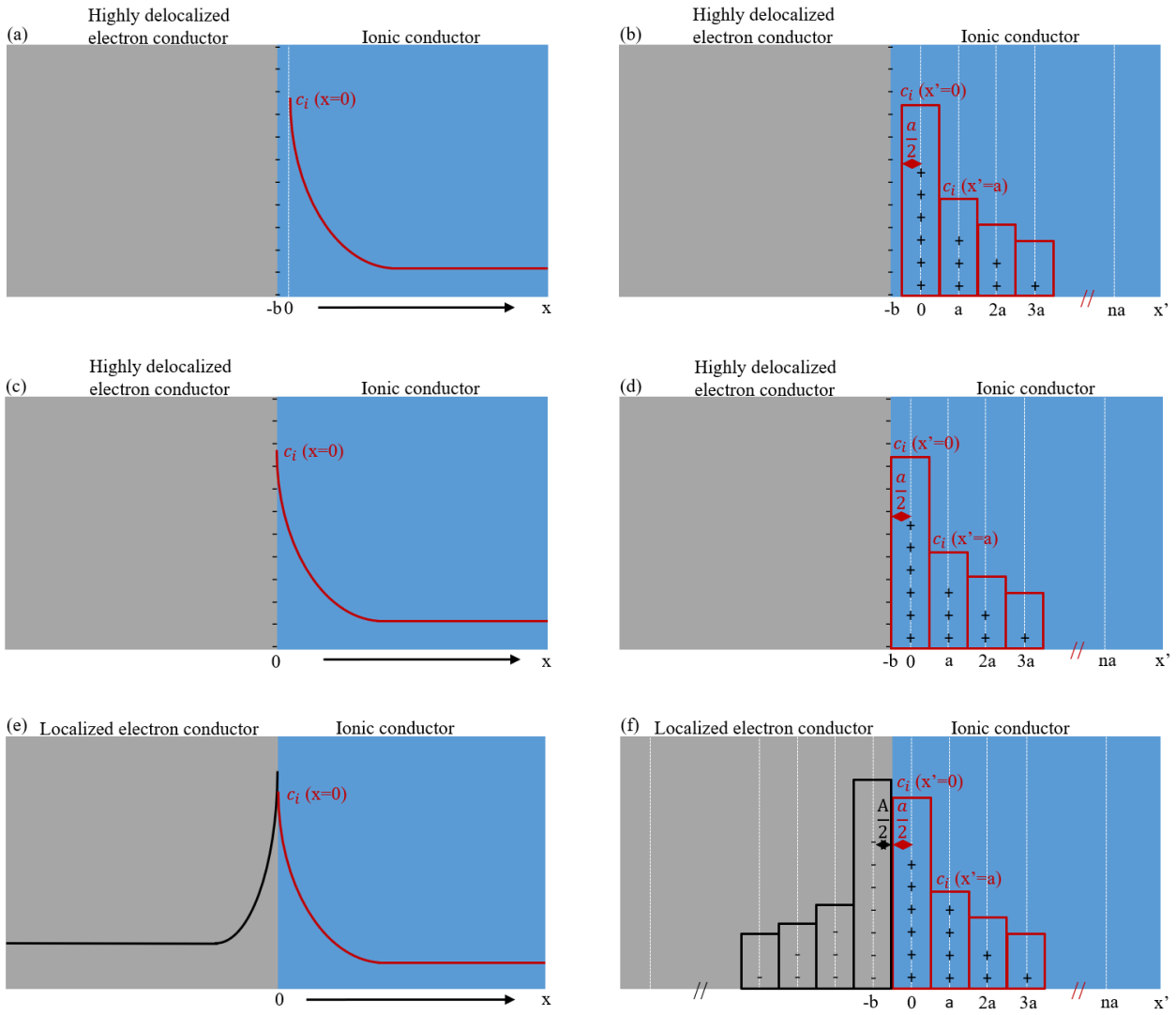

Fig. 2.4 Sketch of (a), (c), (e) continuum model and (b), (d), (f) discrete model. (a), (b), (c), (d) contact between a highly delocalized electron conductor and an ion conductor; (e), (f) contact between a localized electron conductor and an ion conductor. Note the different coordinates x and x' denoting the zero-points in the continuum and in the discrete model, respectively. b is the distance between the two adjacent discretely charged layers, its minimum value is $\frac{a}{2}$ in the case of delocalized electron conductor and $\frac{a+A}{2}$ in the case of localized electron conductor where a, A refer to the atomic size in the ion conductor and localized electron conductor, respectively.

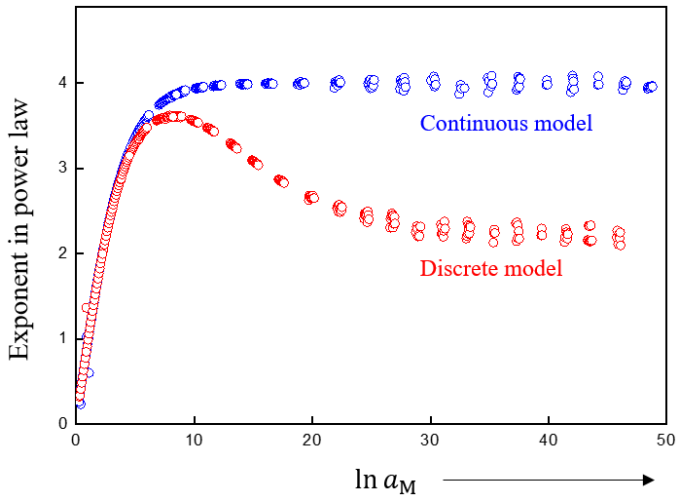

Fig. 2.5 Comparison of continuum and discrete model for dissociative storage of the component M (e.g., Li, Na) (for conditions discussed in Ref. (*40*)). While the continuum model predicts for large storage a power law between M-activity a_M (reflected e.g. by the cell voltage) and stored charge amount with the exponent 4, the discrete model predicts the correct value of 2 corresponding to the fact that for large storage essentially the first layer is responsible.

Essentially two main scenarios have been treated in solid-state ionics: (i) ion redistribution at constant composition as occurring in heterogeneous electrolytes such as LiI:Al_2O_3 composites (*24*) or CaF_2-BaF_2 heterolayers (*36*), and (ii) the occurrence of ionic space charges compensated by electronic ones in the case of job-sharing storage relying on compositional variations (*40*). The most general case involves the redistribution of ions and electrons in both phases that are in contact. Selected literature examples are LiF/TiO_2 (*53*), $SrTiO_3$-grain boundaries (*58*), TiO_2-dislocations (*71*), $RbAg_4I_5$/C (*32*).

Here the dissociative storage of metal components such as Li, Na or Ag at the contact of an ion conductor with a metallic electron conductor is chosen as a master example (similar to the classically discussed electrolyte/electrode interfaces), and the space charge profiles are modeled by discrete quasi 1D simulations. The advantage of this battery-related example is that it also includes the chemical potential of the respective component as parameter. Equivalently one can consider oxygen ion depletion or accumulation at a perovskite interface as a function of position with the oxygen partial pressure as parameter. The important work of Armstrong and Horrocks (*39*) is followed as far as the modeling technique is concerned. This approach (discretization perpendicular to the interface) captures the major points while discretization in two or three

dimensions would only reveal additional insight into other questions such as crystallographic matching or image force effects, that are, though important, beyond the interest of this study. As in the continuum Poisson-Boltzmann equation, a coarse-grained electric potential is used in order to be independent of quantum-mechanical details (*72*).

The intention of this study is to demonstrate that substantial progress in the field of space charge theory is expected to come from such discretization, rather than relying on corrections to the overstretched Gouy-Chapman function (*73-80*). Because of the extreme worth of the continuum approach in terms of its simplicity, the approach is also useful for developing corrections (based on the discretization) that enable Gouy-Chapman considerations to remain applicable, as well as for developing criteria that determine when they fail.

The next section sets out the numerical procedure. Moreover, effects on capacitance and resistance are described whereby special emphasis is laid on the small-signal evaluation. Though this is not the most typical case where the continuum approach fails, it is extremely helpful for the illustration as the analysis is straightforward. The third part shows that how corrections to the idealized assumptions (constant structure, constant dielectric constant, no site saturation) can be implemented and even advantageously combined with the continuum description for the flatter part of the profiles by using realistic input data, e.g., from DFT.

2.2.2 Modeling Procedure

The Poisson-Boltzmann equation is applied as the relevant continuum description.

The curvature of the electric potential ϕ in a medium is, according to Poisson's equation, connected with the effective charge density ρ as well as the corresponding dielectric constant $\varepsilon\varepsilon_0$ according to

$$\nabla^2\phi = -\frac{\rho}{\varepsilon\varepsilon_0} = -\frac{F}{\varepsilon\varepsilon_0}\sum_m z_m c_m \tag{2.1}$$

The abbreviations z_m and c_m stand for the charge number and the concentration (number of moles per volume) of species m; F is the Faraday constant.

If the charge carrier concentration is described by a Boltzmann distribution (the local concentration is proportional to the bulk concentration $c_{m\infty}$ and the exponential of the electric potential difference with respect to the bulk value ϕ_∞) and by identifying this potential with the one in Poisson's equation, the well-known Poisson-Boltzmann equation is obtained

$$\nabla^2\phi = -\frac{F}{\varepsilon\varepsilon_0}\sum_m z_m c_{m\infty} e^{\frac{-Fz_m(\phi-\phi_\infty)}{RT}} \tag{2.2}$$

For a monovalent ion conductor with two types of dilute charge carriers ($+$ and $-$) with semi-infinite boundary conditions (a case which is concentrated on in the following), the integral of Eq. (2.2) becomes

$$\nabla\phi(x) = \frac{F}{\varepsilon\varepsilon_0}\int_x^\infty (c_+(x) - c_-(x))\,dx$$

$$= \frac{Fc_\infty}{\varepsilon\varepsilon_0}\int_x^\infty (e^{\frac{-F(\phi(x)-\phi_\infty)}{RT}} - e^{\frac{F(\phi(x)-\phi_\infty)}{RT}})\,dx \tag{2.3}$$

where c_+ and c_- refer to the local concentrations of the dilute charge carriers. Owing to electroneutrality in bulk, $c_\infty \equiv c_{+\infty} = c_{-\infty}$.

In discretized form Eq. (2.3) reads

$$\phi_j = \phi_{j-1} - \frac{RT(\Delta x')^2}{F\lambda^2}\sum_{k=j}^{\infty}\sinh\left(\frac{F(\phi_k - \phi_\infty)}{RT}\right) \tag{2.4}$$

where $\lambda = \sqrt{\frac{\varepsilon\varepsilon_0 RT}{2F^2 c_\infty}}$ is the Debye length.

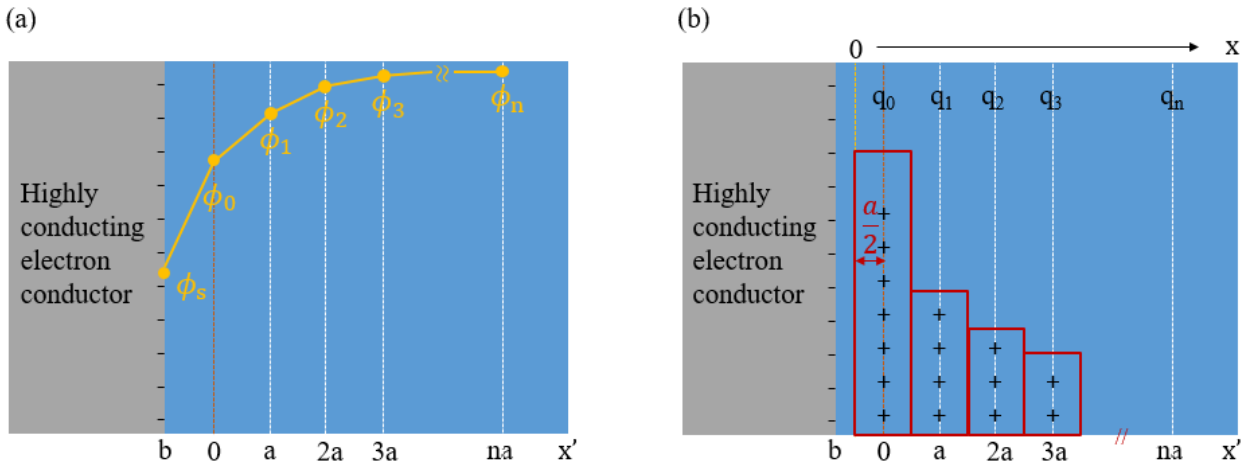

Fig. 2.6 Sketch of (a) potential profile, (b) charge distribution in discrete model (contact between a highly delocalized electron conductor and an ion conductor). The negative counter charge concentrates on the very surface of the highly delocalized electron conductor.

In Fig. 2.6, the discrete model (*39*) is illustrated with two key features: First, $\nabla\phi$ (slope in Fig. 2.6a, i.e. electric field) changes values only on each lattice plane where charge carriers are located, remaining invariant in between the planes. (See Poisson equation, $\nabla^2\phi \propto \rho$. If $\rho = 0$, $\nabla\phi$ is constant.) Such a feature is different from the continuum model in which $\nabla\phi$ varies continuously because ρ is thought to be nonzero within the whole space charge region. Second, as suggested in Eq. 2.4, the slope between plane j and $j-1$ is proportional to the stored charge summing up from plane j to the bulk, resulting in an increase as the interface is approached (Fig. 2.6a). Fig. 2.6b represents the situation in terms of charge distribution: While in the discrete case one can assign a charge to a specific layer (Fig. 2.6b), in the continuum approach one has to be aware of smearing the charge density out by $\pm\frac{a}{2}$ around the position in which the atoms sit which are vertically separated by a. This is the reason why it is necessary to distinguish between x and x' as defined in Fig. 2.4. The rationale as to why the continuous profile best starts at $x' = -\frac{a}{2}$ (and hence $x - x' = \frac{a}{2}$) will be explained later. Since the details of the discrete models are not belonging to the core part of the text, only the major results are given. For derivations, the reader is referred to the Appendix and the respective paper (*81*).

2.2.3 Results and Discussion

2.2.3.1 Idealized Model

Fig. 2.4b, d, f sketches the discrete charge distribution of a contact between an electron conductor and a solid ion conductor. It considers two extreme situations: the highly conducting electron conductor, where the electronic counter charge concentrates on the very surface of the electron conductor (Fig. 2.4a, b, c, d); in the second case, the contact of a poor electron conductor and an ion conductor is considered where both types of charges are strictly localized (Fig. 2.4e, f) and poorly screened. On both sides, an electric double layer is formed by the separation of charges. If b is the distance between the two adjacent discretely charged layers, its minimum value is $\frac{a}{2}$ in the first and $\frac{a+A}{2}$ in the second case where A is the atomic size in the localized electron conductor. Therefore, it is pertinent to distinguish between the extreme cases of a highly delocalized electron conductor and an electron conductor where the electrons are localized at the polyvalent cations. For the sake of simplicity, the fact is ignored that according to the jellium model the electron density of a metal can be smeared out around the very surface with an extent of a fraction of the Fermi-wavelength (typ. by $\sim 2\,\text{Å}$) (*49*). In the following the discrete charge distribution is calculated, and compared with solutions from the Poisson-Boltzmann equation providing the same total charge and calculated conductance and capacitance differences. The highly delocalized electron conductor case is considered as the electronic part of our master example. In order not to complicate the description, the layers that contain an equal amount of singly-charged cations and anions with the charge carriers being cation and anion vacancies are considered. When disorder is referred to Frenkel disorder instead of Schottky disorder, then charges have to be inserted in between the lattice planes.

Regarding conductance and resistance, in a measurement parallel to the interface it is the conductance $Y^{\parallel}$ (conductance per area) that is of significance (for more details, see Appendix II). In terms of space charge capacitance, the effects can be significant. This is because the centroid of the diffuse charge which determines the space charge capacitance, differs, in particular if the screening length is large. Let us first recapitulate the important point (*82*) that

$$\frac{\varepsilon}{C_{\text{SC}}} = \mathcal{L} \tag{2.5}$$

where $\varepsilon = \varepsilon_r \varepsilon_0$, C_{SC} the space charge capacitance (per area) and $\mathcal{L}$ the centroid, which is calculated in the discrete model as

$$\mathcal{L}(x') = \frac{\sum_i x_i' q_i}{\sum_i q_i} \tag{2.6}$$

and in the continuum model as

$$\mathcal{L}(x) = \frac{\int x\rho(x)dx}{\int \rho(x)dx} \tag{2.7}$$

Eq. (2.6) follows directly from Poisson's equation (*82*). Obviously $\mathcal{L}$ shifts by Δ if x or x_i' is shifted by Δ. In Eq. (2.6), q_i denotes the area-specific charge at the i-th plane (positioned at x_i'), while Q will represent the integrated charge per area. In Eq. (2.7), ρ is the continuous charge density and x the position coordinate in the continuous model which is – owing to the atomic size – shifted with respect to x' by $-\frac{a}{2}$, i.e. $x' + \frac{a}{2} = x$.

Appendix III illustrates this for a few simple situations.

Owing to basic electrostatics, the total interfacial capacitance of the semi-infinite configuration represented in Fig. 2.4b can be expressed as

$$\frac{1}{C} = \frac{d(\phi_S - \phi_\infty)}{dQ} = \frac{d(\phi_S - \phi_0)}{dQ} + \sum_{i=0}^{\infty} \frac{d(\phi_i - \phi_{i+1})}{dQ}$$

$$= \frac{d(\phi_S - \phi_0)}{dQ} + \sum_{i=0}^{\infty} \frac{d(\phi_i - \phi_{i+1})}{dQ_{i+1}} \frac{dQ_{i+1}}{dQ} \tag{2.8}$$

where

$$Q_{i+1} = Q - \sum_{k=0}^{i} q_k = \sum_{k=i+1}^{\infty} q_k$$

The evaluation for our assumption leads to

$$\frac{1}{C} = \frac{a}{\varepsilon}\left(\frac{b}{a} + \left(1 - \frac{dQ_0}{dQ}\right) + \left(1 - \frac{dQ_0}{dQ} - \frac{dQ_1}{dQ}\right) + \cdots\right) \tag{2.9}$$

The first term allows for an interfacial spacing of $b \neq a$.

By identifying the last term with Eq. (2.5), the result can be then represented by the well-known relation

$$\frac{\varepsilon}{C} = \frac{\varepsilon}{C_{\mathrm{H}}} + \frac{\varepsilon}{C_{\mathrm{SC}}} \tag{2.10}$$

with $C_{\mathrm{H}} = \frac{\varepsilon}{b}$ as Helmholtz capacitance.

To compare the discrete with the continuum model, it is very illustrative to first use the well-known exponential limit of the Poisson-Boltzmann equation that follows for $|\psi| \ll 1$.

Using Eq. (2.10) with $\frac{1}{C_{\mathrm{SC}}} = \frac{\mathcal{L}_d}{\varepsilon}$, the final rather precise result can be obtained as

$$\frac{1}{C} = \frac{b}{\varepsilon} + \frac{\lambda - \frac{a}{2}}{\varepsilon} \tag{2.11}$$

(Regarding derivation details, see Appendix IV and the respective paper (*81*))

The above conclusion that an adequate continuous picture, for which the total charge coincides with the discrete one, implies an origin shift by $-\frac{a}{2}$ and delivers a straightforward interpretation. A shift between $\mathcal{L}_d$ and $\mathcal{L}_c$ by $\frac{a}{2}$ means that on an absolute scale the two centroids take identical positions. Unsurprisingly, for very small λ this cannot be the case and in fact the centroid correction tends towards zero rather than $\frac{a}{2}$. $\mathcal{L}_c$ is then small and even more so $\mathcal{L}_d$ as well as the difference between both. As the exponential solution is then no longer applicable, the full G-C solution has to be inspected.

Indeed, as Fig. 2.7 shows, one then also recognizes the transition from $\frac{a}{2}$ to 0. Since this correction becomes small when on the other hand the centroid is close to the boundary, and since the correction becomes less important if λ increases, taking $b + \lambda$ as effective difference in the double layer capacitance is a good approximation, yet Eq. (2.11) is perceptibly more precise.

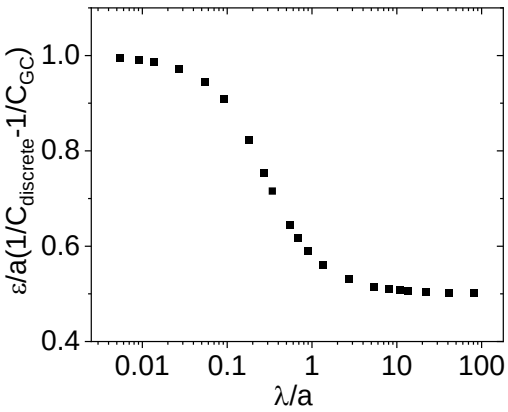

Fig. 2.7 Normalized Helmholtz correction (discrepancy between discrete result and Gouy-Chapman result) as a function of Debye length λ when the full Poisson-Boltzmann equation (a=b is assumed) is inspected. For large λ, the correction with respect to the full geometrical correction is due to the $\frac{a}{2}$-shift of the centroids. This figure shows the transition of Helmholtz correction from $\frac{a}{2}$ to a with decreasing λ.

Such investigations are particularly interesting when non-idealities such as variations of the local (free) energy to form a carrier near the interface (more precisely deviations of μ^0 from the bulk value), saturation effects and permittivity variation are considered. The case of permittivity variation is given as an example in next section. The derivation details and other examples of non-idealities are given in Appendix.

2.2.3.2 Realistic Model: Permittivity Variation

There are essentially three points resulting in variation of the dielectric constant at the interface region, which are not independent: 1) At high fields (as they occur close to the boundary) dipoles tend to be oriented, and the change of polarization with applied field is small (field saturation). A quantitative relation has been given by Booth (*83*, *84*) (see also the recommendable paper by Wang and Pilon (*85*)). 2) Polarization is less pronounced due to special interfacial effects. 3) The other side may not dielectrically contribute, which affects the effective permittivity. In a Gouy-Chapman picture these effects lead to a lower dielectric constant (*86-88*).

Fig. 2.8 investigates the ε-variation effects with $\Delta\mu^0 = 0$ and absence of site saturation. As an example ε in the first layer is taken to be 1 and from second layer on bulk-values (ε =10) are

applied. In this case, the centroid shifts slightly towards the interface direction and in our example the capacitance decreases from 8.6 μF/cm^2 to 3.1 μF/cm^2 according to

$$\frac{1}{C} = \frac{b}{\varepsilon_1} + \frac{a}{\varepsilon_1} + \frac{\mathcal{L} - a}{\varepsilon_{bulk}} \tag{2.13}$$

where ε_1 is referring to the dielectric constant in the first layer adjacent to an interface.

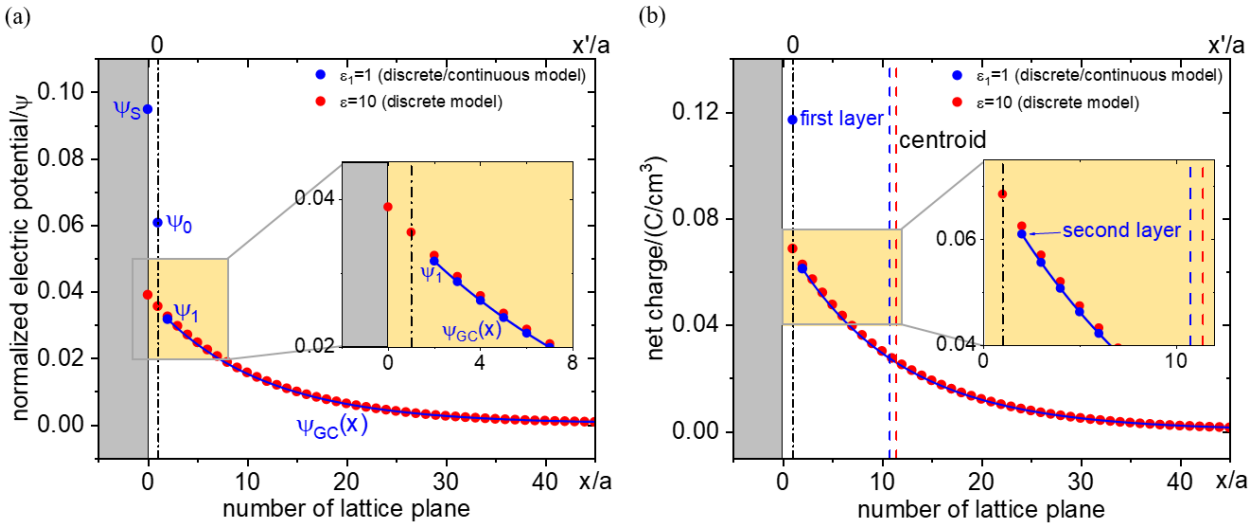

Fig. 2.8 The profiles of (a) electric potential and (b) charge carrier concentration shown as a function of number of lattice plane. The blue data shows the model with ε-variation in the first layer adjacent to the interface. The blue curve shows the continuum model from second layer on. The red data shows the discrete model without ε-variation. Blue and red dashed lines in (b) indicate the positions of centroid for both cases (with or without ε-variation). Black dash-dotted line is referring to the position of first layer. Simulation parameters: lattice spacing $\Delta x'$=0.1 nm; $\phi_s - \phi_\infty$=-1 mV; c_∞=1 ×10^{-5} mol/cm^3; μ^0 is constant; T=298 K; ε at the first adjacent layer is taken to be 1, which differs from the bulk value ($\varepsilon_{bulk} = 10$). From second layer on the bulk values for ε are applied. $\mathcal{L}(\varepsilon = 10) = 1.04$ nm and $\mathcal{L}(\varepsilon_1 = 1;\ \varepsilon_{bulk} = 10) = 0.97$ nm. $C(\varepsilon = 10) = 8.6$ μF/cm^2 and $C(\varepsilon_1 = 1;\ \varepsilon_{bulk} = 10) = 3.1$ μF/cm^2. Note the slight difference between red dots and blue line for $x' \geq a$.

For very small $\mathcal{L}$, ε-variation can have a considerable influence on the capacitance, which leads to a reduction of capacitance by approximately one order of magnitude in this situation. On the other hand, ε-variation in the first layer gives rise to a negligible capacitance change in the case of very large $\mathcal{L}$.

2.3 Conclusion

In this Chapter, discrete modeling of space charge zones in solids is presented, which is a sensible approach for handling pronounced space charge potentials as well as non-idealities in realistic solid state system. A variety of shortcomings and unrealistic assumptions necessary for the validity of the Gouy-Chapman solution for ionic space charges can be overcome by such 1D discrete modeling or a combination of 1D discrete modeling and continuum approach. Moreover, the details on the difference between space charge capacitance and measured capacitance are also revealed by discretization. This discrepancy is not completely removed by a Helmholtz correction, in more precise terms also an inherent small shift of the centroid of charge has to be considered.

A particularly useful application of this approach is the explicit implementation of crystallographic details and non-idealities close to the interface, even though it does not remedy the inherent inconsistency problem of the Poisson-Boltzmann equation. In the discretized zone, knowledge (from atomistic modeling or experiments) about non-idealities (such as energetic variations owing to structural or elastic effects, variations in the dielectric permittivity or saturation effects) can be included in a straightforward way.

Examples treated refer to variations in the energy levels, dielectric constant and exhaustion effects. MgO and $SrTiO_3$ examples (Appendix V) clearly show how discretization is utilized to handle non-idealities in realistic solid-state system by inserting calculated data (e.g., from DFT). Pronounced space charge effects and non-idealities are ubiquitous in solid state, for example in the electrochemical storage systems under concern in this thesis (TiO_2). As far as the core part of the thesis is concerned, namely the spatial distribution of the stored charge in titania, details of the discretized model are not important. Rather the significance of single-layer storage will be stressed whenever necessary.

3

Materials Preparation and Characterization

3.1 Materials and Methods: Thin Film Deposition

3.1.1 Atomic Layer Deposition (ALD)

Atomic layer deposition (ALD) is a type of chemical vapor deposition (CVD) based on sequential utilization of multiple vapor-phase precursors. Most ALD reactions involve two such precursors. The substrate is exposed to gaseous precursors as a series of sequential, non-overlapping pulses, rather than being present simultaneously in the reaction chamber as in other CVD methods. Molecules of the first precursor are chemically adsorbed at the surface; then flowing the second precursor causes a self-limiting reaction; the reaction terminates when all the reactive sites on the surface are consumed.

In this thesis, a Cambridge Nanotechnology Savannah atomic layer deposition system (Veeco) was utilized to deposit TiO_2 thin films. Tetrakis-dimethylamido-titanium (TDMAT, Sigma-Aldrich Chemie GmbH) and H_2O were used as the precursors. The deposition process is shown schematically as Fig. 3.1. First, precursor 1 (TDMAT) was pulsed into the reaction chamber and chemically adsorbed on the surface of the substrates (0.5 wt% Nb doped $SrTiO_3$ (*N-ST*, from SurfaceNet and CrysTec, (100) orientation, 10×10 mm, one side polished), sapphire (from CrysTec, (0001) orientation, 10×10 mm, one side polished), MgO (from CrysTec, (100) orientation, 10×10 mm, one side polished) and Ru on *N-ST* substrates). Regarding Ru substrate preparation, Ru was sputtered on top surface of 0.5 wt% *N-ST* (Ru target, Testbourne, 57 mm dia. x 1.5 mm thick, 99.95% Pure) by DC sputtering (Emitech K575X) at room temperature in a glovebox. Then all the gas phases (reaction by-products and remaining TDMAT molecules) were purged out, and precursor 2 (H_2O) was injected into the chamber. Finally all gas phases were

purged out, leaving one TiO_2 monolayer on the surface. The H_2O reaction with TDMAT can be described by the following equation:

$$Ti(NMe_2)_4\,(g) + 2\,H_2O\,(g) \rightarrow TiO_2\,(s) + 4\,HNMe_2\,(g)$$

The growth conditions were optimized by varying the pivotal parameters of ALD process: temperature, type of precursors, pulse duration, and purge duration. The typical deposition temperature is 100-250 °C and the general pulse duration and purge duration are 10-200 ms, 5-30 s, respectively. The purge time also depends on temperature and pumping rate. After a series of control experiments, suitable growth conditions were identified. For example, when the growth temperature is 200 °C, a pulse time of 200 ms for TDMAT cycle and 15 ms for H_2O cycle and a purge time of 10 s for TDMAT cycle and 10 s for H_2O cycle are sufficient (Fig. 3.1b). Uniform TiO_2 thin films of different thicknesses were obtained by varying the number of cycles. Then the deposited TiO_2 films were annealed at 300 °C for 2 h under argon atmosphere.

Nb_2O_5 thin films were deposited on 0.5 wt% *N-ST* by ALD (Cambridge Nanotechnology Savannah atomic layer deposition system (Veeco)) at 150 °C and plasma-enhanced ALD (PE-ALD, Sentech ALD with Real-time Monitoring) at 400 °C. In the Cambridge Nanotechnology Savannah ALD system, Tris(diethylamido)(tert-butylimido)niobium(V) (TBTDEN, Sigma-Aldrich Chemie GmbH) was used as the precursor. A pulse time of 6 s and a purge time of 15 s for TBTDEN cycle were applied, following two steps H_2O pulse (pulse: 30 ms, purge: 10 s; pulse: 30 ms, purge: 30 s). Regarding the Sentech PE-ALD system, Tris(diethylamido)(tert-butylimido)niobium(V) (TBTDEN, DOCKWEILER CHEMICALS GmbH) in a bubbler cylinder was used as the precursor, which was pulsed into the chamber for 1 s, following a 15 s purge. Then Oxygen Plasma (200 W, 20 Pa, 150 sccm) was applied for 10 s, afterwards the system was purged for 1 s. The as-grown Nb_2O_5 films were annealed at 750 °C for 2 h under argon atmosphere.

ALD shows tremendous advantages in comparison to other thin-film deposition techniques. It can be used to produce even sub-10 nm films with precise thickness control. It also exhibits excellent conformal coverage on three-dimensional complex structures. In addition, the impurity contamination is low due to the self-limited surface reaction mechanism and low-temperature processing (*89, 90*). ALD was performed in the Scientific Facility Nanostructuring Lab (NSL).

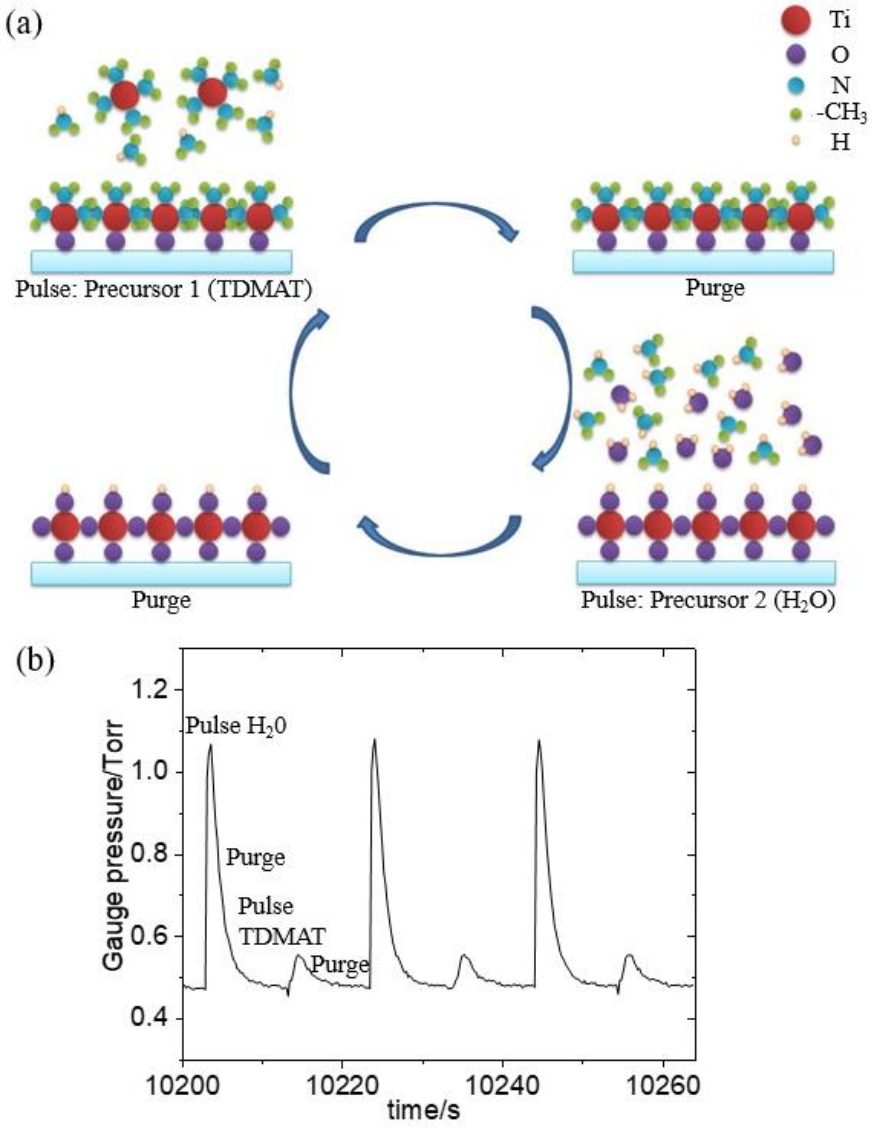

Fig. 3.1 (a) Schematic representation of anatase TiO_2 thin film growth by atomic layer deposition (ALD); (b) Gauge pressure vs. time during ALD process.

3.1.2 Pulsed Laser Deposition (PLD)

With regard to PLD, anatase TiO_2 was deposited on pure and differently doped *ST* substrates (from SurfaceNet and CrysTec, (100) orientation, 10 × 10 mm) at 630 °C under an O_2 pressure of 0.3 mbar. The TiO_2 target was prepared by isostatically pressing TiO_2 powders and sintering the as-pressed TiO_2 pellet. The frequency of the laser is 5 Hz and the energy density is 1.6 J/cm^2. The thickness of films is controlled by the pulse number. Then the temperature was decreased to 450 °C

and the sample was kept at 450 °C under pressure of 1 bar for 30 min annealing treatment after deposition. Afterwards, the sample was cooled down to room temperature. PLD was performed in the Scientific Facility “Thin Film Technology”.

3.1.3 Molecular Beam Epitaxy (MBE)

Regarding MBE, the growth temperature is 630 °C and the pressure ($P_{O_2+O_3}$) is 1.7×10^{-5} Torr. Ti metal (Sigma-Aldrich) was used as the target. Reflection high-energy electron diffraction (RHEED) and Low-energy electron diffraction (LEED) set-ups are equipped in the MBE system. RHEED and LEED data were recorded during film deposition, which are very useful for confirming the quality of deposited films. High quality anatase TiO_2 thin films on pure and differently doped *ST* substrates (from SurfaceNet and CrysTec, (100) orientation, 10×10 mm) were deposited by MBE. MBE was performed in the Scientific Facility “Thin Film Technology”.

3.2 Materials and Methods: Substrate and Thin Film Characterization

3.2.1 X-Ray Diffraction (XRD) and X-Ray Reflectivity (XRR)

All XRD data collections in grazing incidence configuration for thin films and for reflectivity measurements were carried out on a PANalytical diffractometer of the Emperian Series (Cu K_α radiation, 40 kV, 40 mA), equipped with a parallel beam mirror and a PIXcel 3D detector.

Regarding reflectivity measurements, interference occurs between the X-rays reflected from the surface of thin film and the interface between thin film and substrate, which leads the reflectivity profile to an oscillation feature (*91*). The thickness of thin film was obtained based on the curve of periodical oscillation in intensity. The extracted oscillation curve can be operated by Fourier transformation in order to obtain the thickness of a thin film.

Measurements of thin films (common $\theta - 2\theta$ mode) were conducted under Bragg-Brentano configuration using programmable divergence slits, anti-scatter slits and a PIXcel 3D detector.

In terms of measurements at elevated temperature, samples were mounted in a high-temperature oven chamber (HTK 1200N from Anton Paar) with argon flowing.

For data processing and analysis (diffraction and reflectivity data), PANalytical software packages HighScore Plus and Reflectivity were used.

3.2.2 Stylus Profilometry

Stylus profilometers (Dektak 8 Veeco) was utilized to measure the thickness of thin films, which consists of a detector and a sample stage. A probe with a radius of 5 μm was used to scan the surface of the samples and the height profile as a function of position was obtained by physically scanning a stylus with specified contact force along the surface for a specified distance. A feedback system was applied to keep the cantilever with a specific amount of torque on it, which is known as the 'setpoint'. The surface can be reconstructed according to the changes in the Z position of the cantilever.

The resolution depends on the scanning parameters, such as the radius of stylus, scan speed and force. The scanning parameters for this work are shown in Table 3.1.

Fig. 3.2 shows the procedure of sample preparation for profilometry. First the 0.5 wt% Nb doped $SrTiO_3$ substrate (*N-ST*) (from SurfaceNet and CrysTec) or sapphire/MgO substrate (from CrysTec) was cleaned by deionized water, acetone (BASF, Art: 50488858) and then ultrasonic cleaning in isopropanol (BASF, Art: 50489068) was applied for further cleaning, after which Kapton tape was adhered to the edges of *N-ST*/sapphire/MgO substrate before deposition. After the deposition process, the Kapton tape was removed and the deposited TiO_2 thin film stayed on the center of substrate.

The prepared sample was moved to the platform of profilometer and scanned by a stylus with a radius of 5 μm, which is shown as Fig. 3.3. Eight different positions were scanned for every sample and the average value was considered as the thicknesses of the films (Table 3.2).

Stylus Profilometry was performed in the Scientific Facility Nanostructuring Lab (NSL).

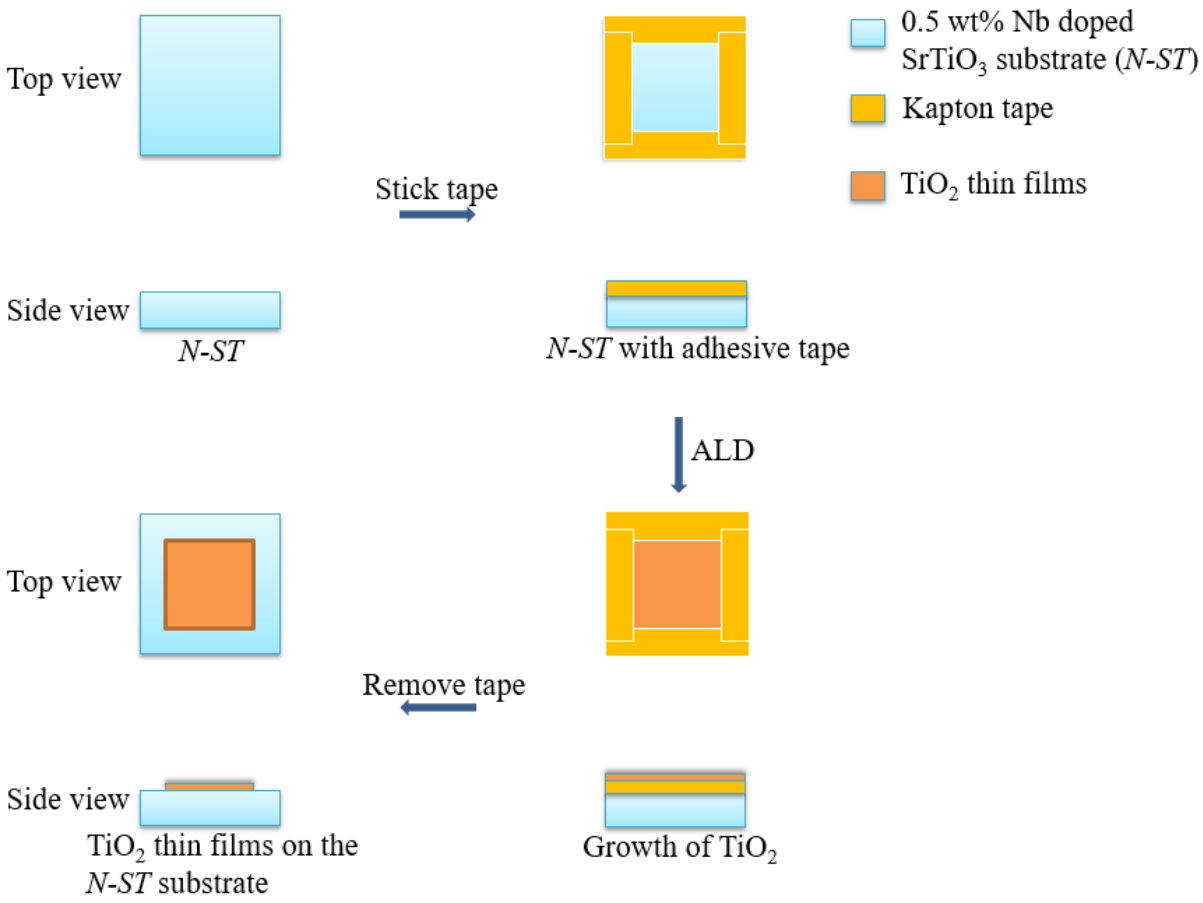

Fig. 3.2 Schematic representation of sample preparation for profilometry.

Table 3.1 Scanning parameters of profilometry.

Parameters	Value & mode
Scan Type	Standard Scan
Radius of Stylus	5 µm
Scan Length	600 µm
Scan Duration	30 s
Force	15 mg
Profile	Hills & Valleys

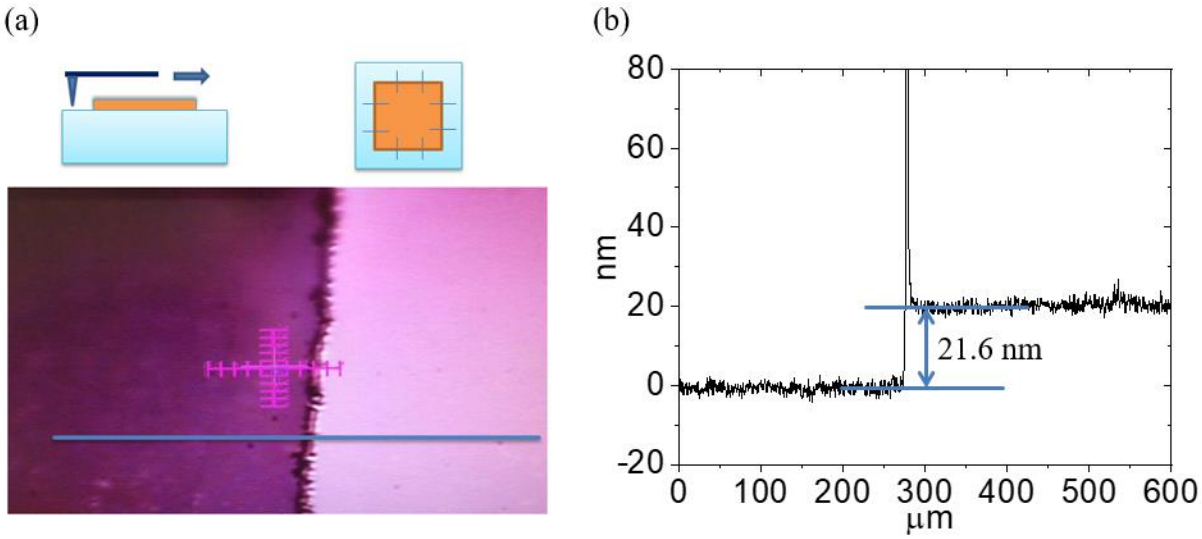

Fig. 3.3 (a) Schematic representation of scanning samples by a stylus. (b) Height profile as a function of position.

3.2.3 Atomic Force Microscope (AFM)

Bruker Dimension ICON AFM was used for AFM measurements, which was operated under PeakForce Tapping™ mode.

In contrast to conventional tapping mode AFM where the cantilever oscillates at or near its resonance frequency, in PeakForce Tapping™ a force/distance curve is acquired in every point. For this, the cantilever oscillates with a frequency in the range of 1-2 kHz, far below its resonance frequency. When the cantilever approaches, it will first experience attractive forces. For smaller tip/sample distances, these are overlaid by repulsive forces. At a certain force set point the tip is retracted again. Due to this very controlled tip trajectory, it is much easier to automatically adjust all imaging parameters including the force set point and the feedback loop. Additionally, it gives qualitative and even quantitative (if well calibrated) insight into mechanical properties like adhesion, dissipation and modulus of the surface on a local scale.

AFM was performed in the Scientific Facility "Interface Analysis".

3.2.4 X-Ray Photoelectron Spectroscopy (XPS)

XPS measurements of Ru substrate were performed on a Kratos Axis Ultra system equipped with a monochromatized Al K_α X-Ray source. For depth profiling, a scanning MiniBeam III Argon ion sputter gun (from Kratos) with a beam energy of 4.0 keV and an emission current of 20 mA was used. XPS data were analyzed with the CasaXPS software (version 2.3.23PR1.0 by Casa Software Ltd). The first sample was exposed to air and then transferred to the XPS chamber. A second sample was prepared in a glove box under Ar atmosphere ($O_2 \leq 0.1$ ppm, $H_2O \leq 0.1$ ppm) and transferred to the XPS chamber in an airtight transfer tool under Ar atmosphere. After first measurement of each sample, the native oxide layer was removed by an Argon ion beam (10 min), following a second measurement.

XPS is an X-Ray based technique to identify the chemical compounds and the related binding energies by measuring kinetic energies of the ejected electrons from the photoelectric effect. XPS is a surface-sensitive tool (few nm depending on the material) since only the electrons close to the surface can escape without the energy loss.

XPS was performed in the Scientific Facility "Interface Analysis".

3.2.5 Focused Ion Beam (FIB): TEM-lamella Preparation

For the preparation of the TEM samples, a FEI Scios dual beam instrument equipped with a Ga source has been used. The samples were transferred inside a sealed capsule from a glove box with Ar atmosphere ($O_2 \leq 0.1$ ppm, $H_2O \leq 0.1$ ppm) to the FIB vacuum chamber without air contact. The FIB milling steps were performed at 30 kV Ga beam, for thinning 5 kV was used and the final polishing step was done with a 2 kV Ga beam. The final thickness of the TEM lamellae was below 50 nm. The procedure of TEM-lamella preparation in the FIB is given as Fig. 3.4. Experimental details can be found in literature (*92*). The final FIB samples were mounted to TEM holders in a glove box and transferred to TEM in the protective environment using a Melbuild vacuum transfer holder.

FIB was performed in the “Stuttgart Center for Electron Microscopy (StEM)”.

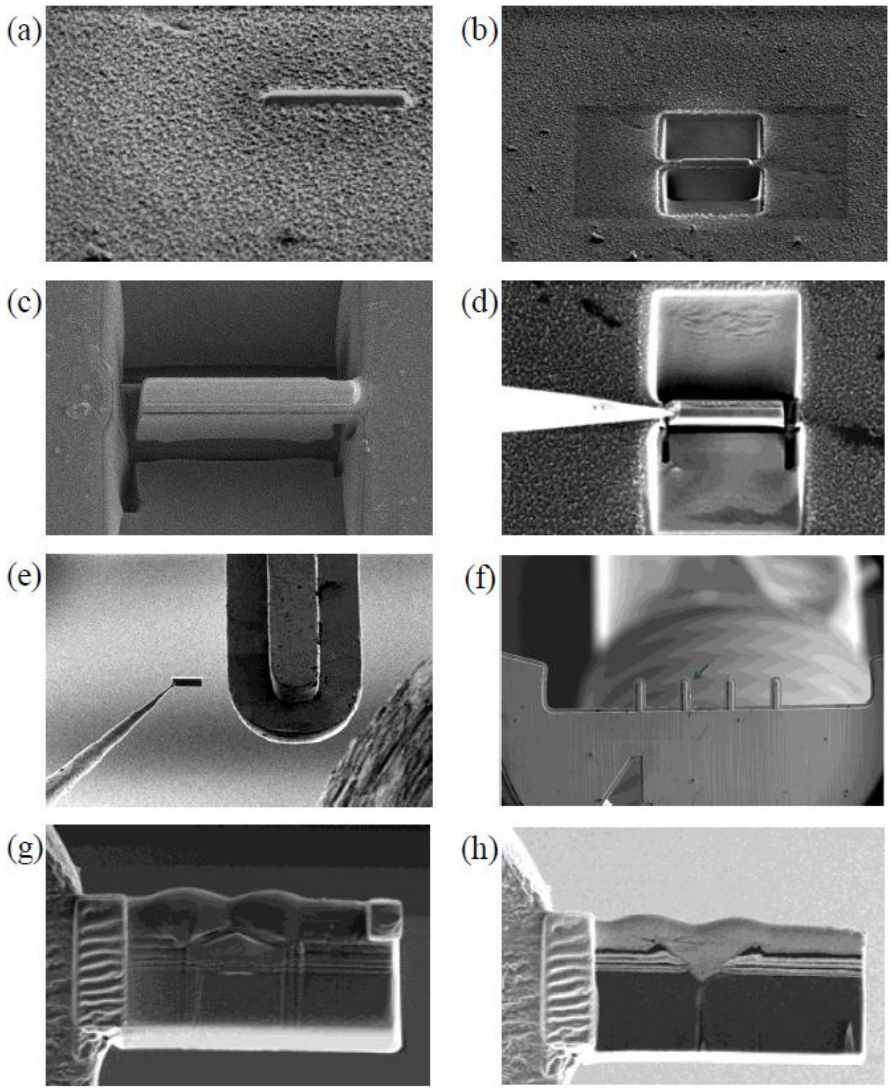

Fig. 3.4 TEM-lamella preparation in the FIB. (a) Protection layer deposition; (b) Rough wedge cutting on two sides; (c) Cut-out; (d) Lift out (SEM view); (e) Transfer to grid (FIB view); (f) Specimen preparation on the grid; (g), (h) Final thinning (reduction of beam current for thinning and reduction of acceleration voltage for final polishing step by step).

3.2.6 Scanning Transmission Electron Microscopy (STEM) and Electron Energy Loss Spectroscopy (EELS)

STEM studies were conducted using a spherical aberration-corrected STEM (JEM-ARM200F, JEOL Co. Ltd.) equipped with a cold-field emission gun and a DCOR probe Cs-corrector (CEOS

GmbH) operated at 200 kV. The HAADF-STEM images were obtained by an ADF detector with a convergent semi-angle of 20.4 mrad and collection semi-angles of 70−300 mrad. Simultaneously, ABF results were acquired by a BF detector with a collection semi-angle of 11-22 mrad. In order to make precise measurements of lattice constants, ten serial frames were acquired with a short dwell time (2 μs/pixel), aligned, and added afterward to improve the signal-to-noise ratio (SNR) and to minimize the image distortion of STEM images. EELS acquisition has been performed with a Gatan GIF Quantum ERS imaging filter equipped with a Gatan K2 Summit camera and a CCD camera with a convergent semi-angle of 20.4 mrad and a collection semi-angle of 111 mrad. EELS spectrum imaging was performed with a dispersion of 0.5 eV/channel for the simultaneous acquisition of signals of the Ti-$L_{2,3}$, O-K and Sr-$L_{2,3}$ edges. EELS line scans were conducted using a K2 camera with a dispersion of 0.1 eV/channel and 0.25 eV/channel to acquire EELS spectra of Li-K, O-K and Ti-$L_{2,3}$ edges for further fine structure analysis (See Fig. 3.5 for the corresponding energy resolution). The raw spectrum image data were denoised by applying a principal component analysis (PCA) with the multivariate statistical analysis (MSA) plugin (HREM Research Inc.). For calculating the Ti valence state, the electron energy-loss near-edge structure of Ti-$L_{2,3}$ was analyzed using a multiple linear least-squares fitting algorithm based on the measured Ti-$L_{2,3}$ edges of standard samples with Ti^{4+} ($SrTiO_3$) and Ti^{3+} ($LiTiO_2$).

STEM and EELS were performed in the “Stuttgart Center for Electron Microscopy (StEM)”.

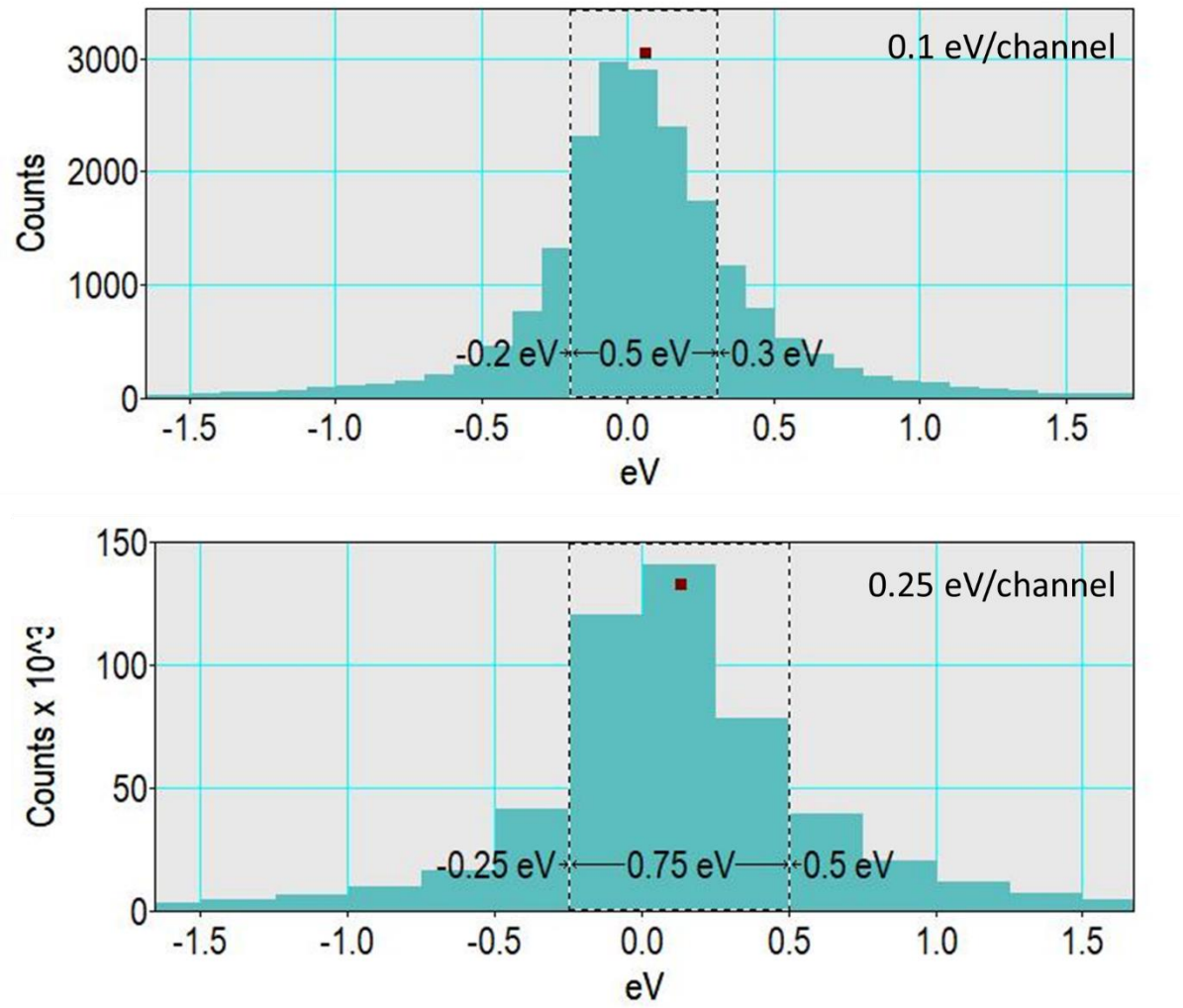

Fig. 3.5 EELS zero-loss peaks acquired with the dispersion of 0.1 eV/channel and 0.25 eV/channel. The energy resolution can be determined as the full-width at half-maximum of the zero-loss peak.

3.3 Results and Discussion

RHEED and LEED data were recorded during film deposition (MBE) as shown in Fig. 3.6 and Fig. 3.7, respectively. The superstructure is clearly identified according to the diffraction patterns. Both RHEED and LEED data evidence that the deposited films are of good quality.

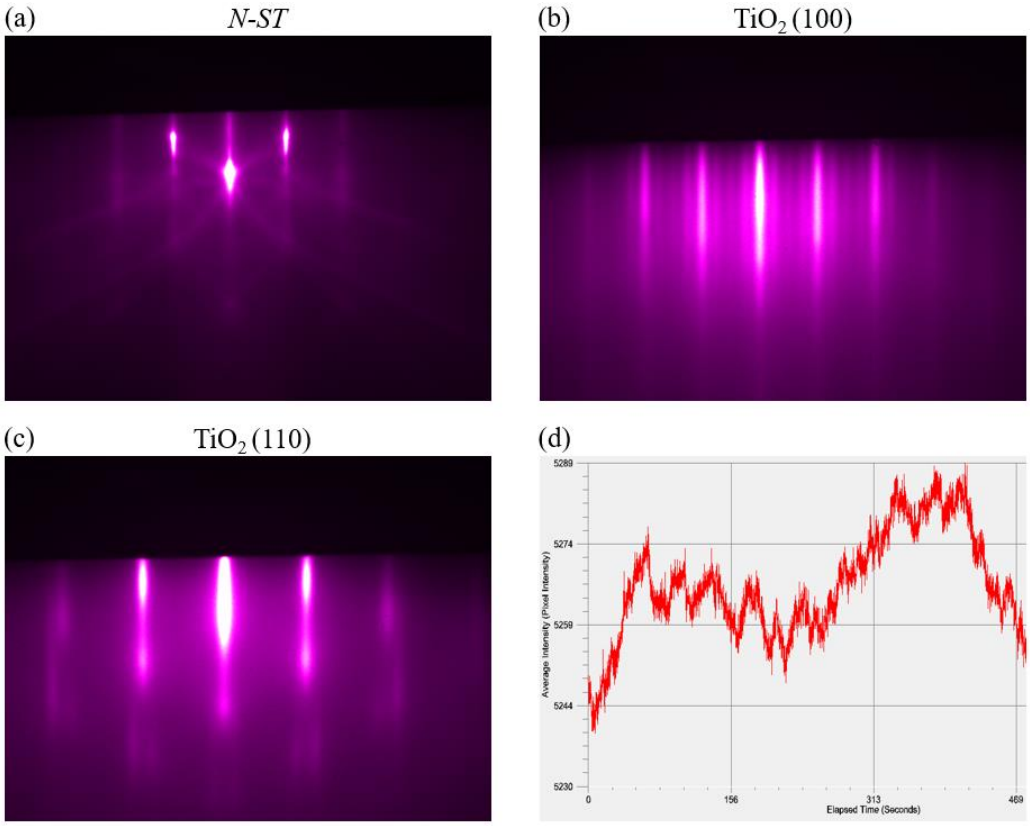

Fig. 3.6 Reflection high-energy electron diffraction (RHEED) of (a) 0.5 wt% Nb doped $SrTiO_3$ (*N-ST*), (b) deposited TiO_2 with (100) orientation (the superstructure is clearly identified), and (c) (110) orientation. (d) Average intensity as function of elapsed time.

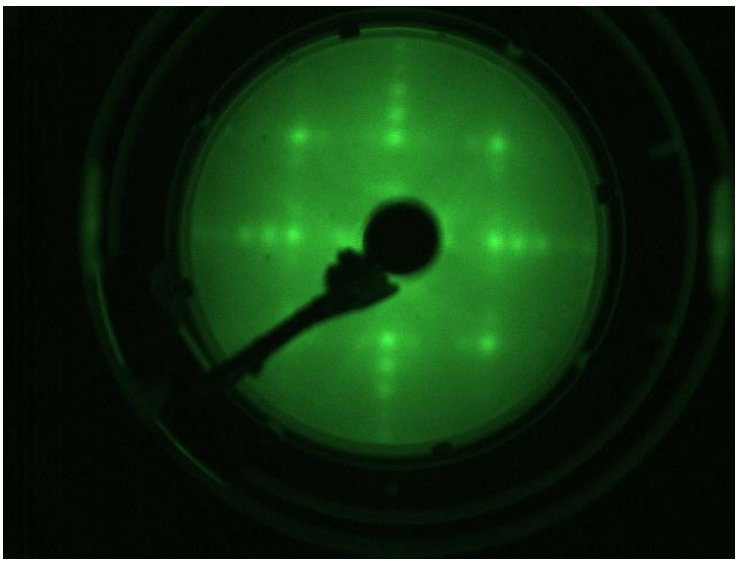

Fig. 3.7 Low-energy electron diffraction (LEED) of TiO_2 (deposited by MBE) on 0.5 wt% Nb doped $SrTiO_3$ (*N-ST*).

X-Ray Diffraction (XRD) and X-Ray Reflectivity (XRR)

In-situ GIXRD results of a TiO_2 (*T*) thin film on sapphire substrate (Fig. 3.8), which was deposited by ALD, show that all the peaks belong to the anatase phase indicating the desired pure anatase was obtained (as-grown or after 300 ℃ annealing). The diffraction intensity of the film after 2 h annealing treatment is higher than that from as-grown film, which demonstrates the improvement of crystallinity after annealing. From 2 h on, the peaks intensity stays identical giving evidence that 2 h annealing treatment is sufficient.

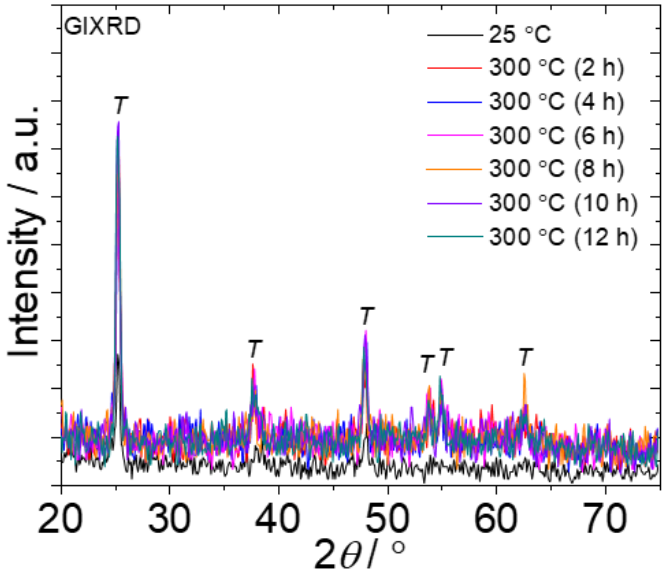

Fig. 3.8 In-situ GIXRD measurements of TiO_2 (*T*) thin film on sapphire substrate (deposited by ALD) during annealing treatment.

TiO_2 (*T*) thin films (deposited by ALD) on 0.5 wt% *N-ST* substrate were characterized by XRD ($\theta - 2\theta$ mode and GIXRD mode) and XRR. Only a single peak (Fig. 3.9 (a), (b)) from anatase appears for both diffraction modes, indicating that (004) orientation (c-direction) is dominant. The thicknesses of the two TiO_2 thin films are obtained as 23.7 nm, 12.1 nm, respectively, based on the clear periodical oscillation curves (XRR, Fig. 3.9 (c)). XRD and XRR results evidence high quality of TiO_2 thin films.

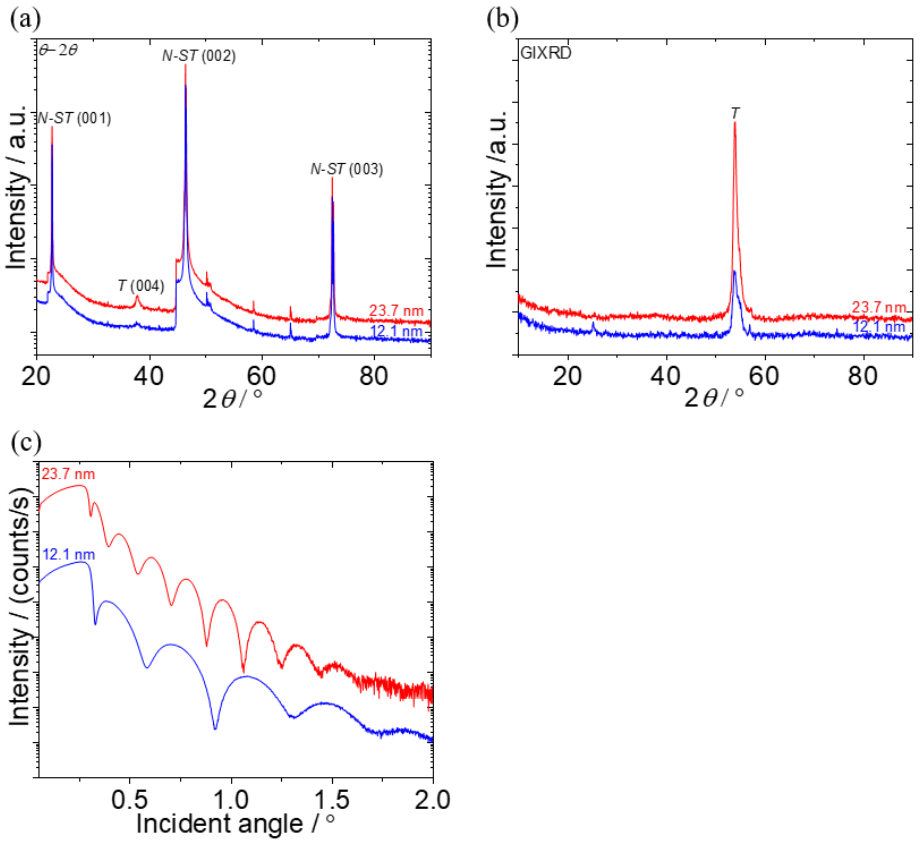

Fig. 3.9 XRD and XRR measurements of two TiO_2 (*T*) thin films on 0.5 wt% *N-ST* substrates deposited by ALD. (a) XRD patterns (normal scan, $\theta - 2\theta$ mode); (b) GIXRD patterns; (c) XRR results.

Similarly, GIXRD results of TiO_2 (*T*) thin films (on *N-ST* substrates) deposited by PLD and MBE (Fig. 3.10 (a), (b), (d), (e)) show only a single peak from anatase (same as ALD films), which indicates that (004) orientation (c-direction) is dominant. The thicknesses of the TiO_2 thin films are obtained as 21.1, 9.7, 8.0, 5.3 nm for PLD films and 8.6 nm for MBE films, respectively, based on XRR results. In addition, TiO_2 (*T*) thin films deposited on differently doped *ST* substrates by PLD (Fig. 3.11) exhibit equally good quality. The identical features (diffraction and reflectivity data) of two measurements (on *N-ST* and *F-ST* substrates) confirm the reliability of film deposition.

All TiO_2 thin films on various substrates (differently doped *ST* and Ru substrates) deposited by the three deposition techniques (ALD, PLD, MBE) exhibit high quality, which is essential for the quantitative analysis of storage capacity measurements.

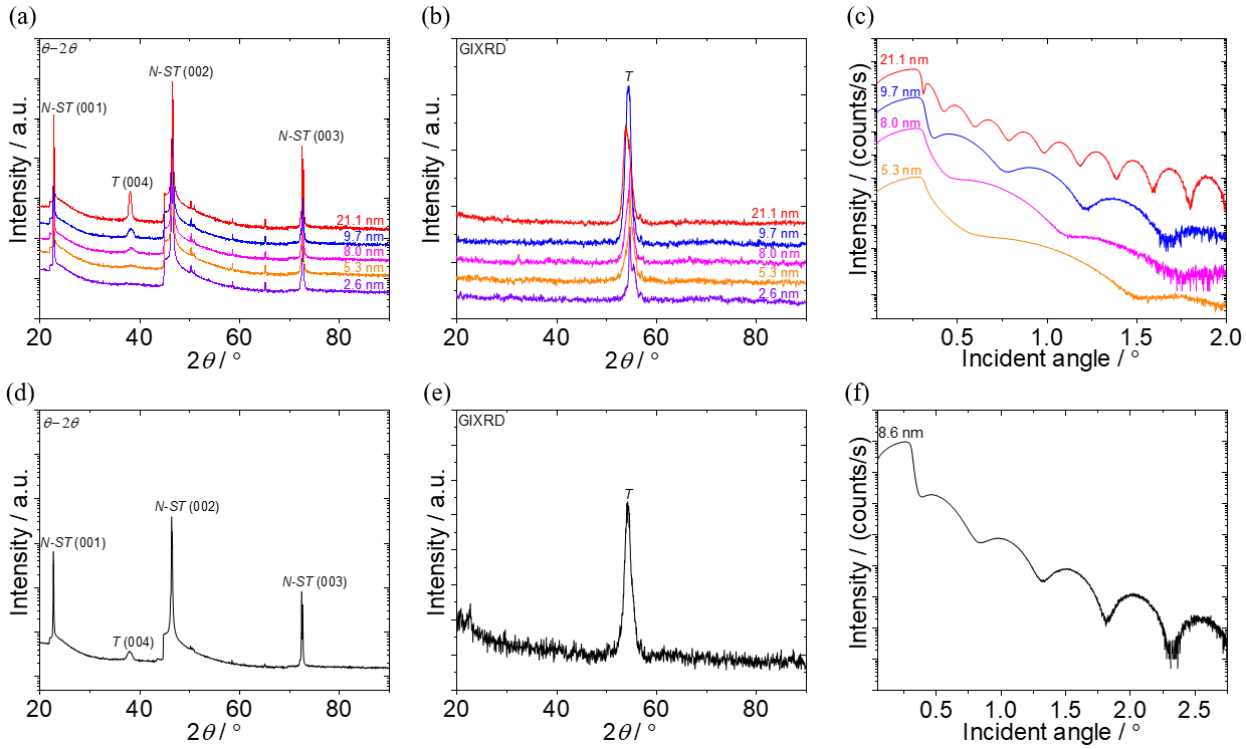

Fig. 3.10 XRD and XRR measurements of TiO_2 (*T*) thin films on *N-ST* substrates deposited by PLD (a), (b), (c) and MBE (d), (e), (f). (a), (d) XRD patterns (normal scan, $\theta - 2\theta$ mode); (b), (e) GIXRD patterns; (c), (f) XRR results. Only a single peak (a), (b) from anatase appears for both diffraction modes (same as ALD films), indicating that (004) orientation (c-direction) is dominant.

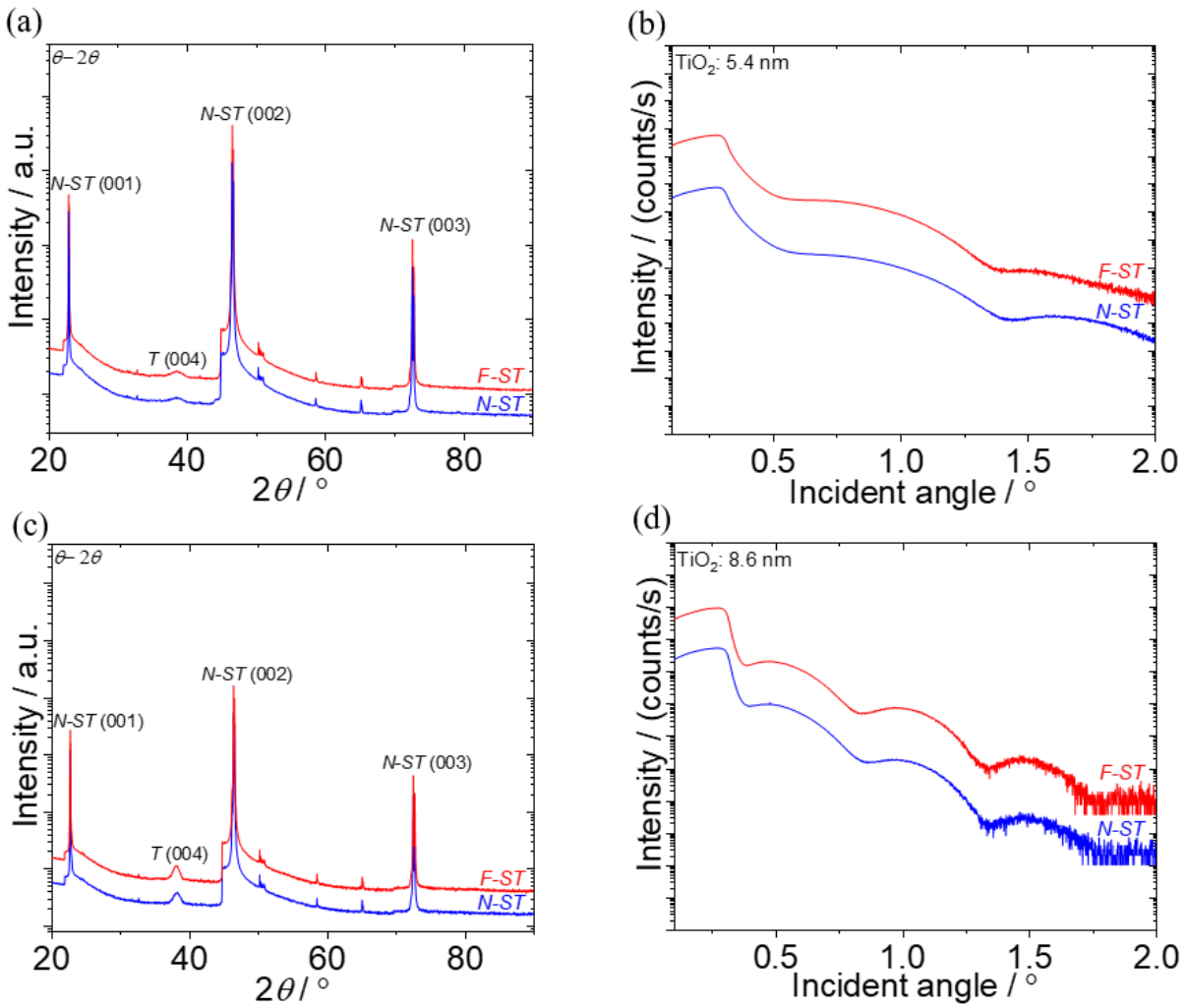

Fig. 3.11 XRD and XRR measurements of TiO_2 (*T*) thin films on *N-ST* and *F-ST* substrates deposited by PLD (same growth condition). (a), (c) XRD patterns (normal scan, $\theta - 2\theta$ mode); (b), (d) XRR results. Only a single peak (a), (c) from anatase appears indicating (001) orientation (c-direction) is dominant. The thicknesses of both (*T* on *N-ST* and *F-ST* substrates) are obtained as 5.4 nm (b), 8.6 nm (d), respectively, based on the periodical oscillation curves.

Film thickness

The above-mentioned XRR measurements provide precise and reliable thickness data of TiO_2 thin films. To verify the reliability, two additional techniques (stylus profilometry and TEM) were utilized to measure the thickness. Regarding stylus profilometry, the measurement details are given in "Materials and Methods" section. Eight different positions were scanned for every sample and the average measured values were considered as the thicknesses of the films (Table 3.2). The standard deviation is less than 0.5%.

Table 3.2 Thickness measured by profilometry

Number of cycles	Measured thickness [nm]								Average [nm]	Standard deviation [nm]
250	12.4	12.3	12.3	10.6	11.4	11.1	12.3	11.7	12.0	0.4
500	21.9	21.2	20.3	20.6	21.5	20.3	20.6	21.4	21.6	0.3
750	32.5	33.4	33.8	32.4	33.9	32.9	33.3	33.2	32.9	0.4
1000	41.9	40.4	41.2	40.1	42.1	40.1	40.8	40.8	41.4	0.5
1500	67.6	68.6	66.1	66.8	68.7	68.0	66.6	66.6	67.1	0.5
3000	144.1	144.7	144.7	142.3	144.8	142.1	144.5	144.7	144.4	0.3
7500	413.5	411.3	413.2	413.2	411.2	409.2	412.5	411.3	412.4	1.1

Simultaneously, TEM measurements provide very precise results. Fig. 3.12 summarizes the thickness determined by XRR, TEM and stylus profilometry. All three techniques give consistent results, indicating reliable and accurate film thickness control (ALD, PLD) and thickness measurement, which is vital for storage capacity analysis. The thickness shows linear relation with cycle number (ALD samples, based on 37 samples) and pulse number (PLD samples, based on 14 samples). The corresponding growth rates are applied to calculate the thicknesses of extremely thin films (e.g., below 5 nm).

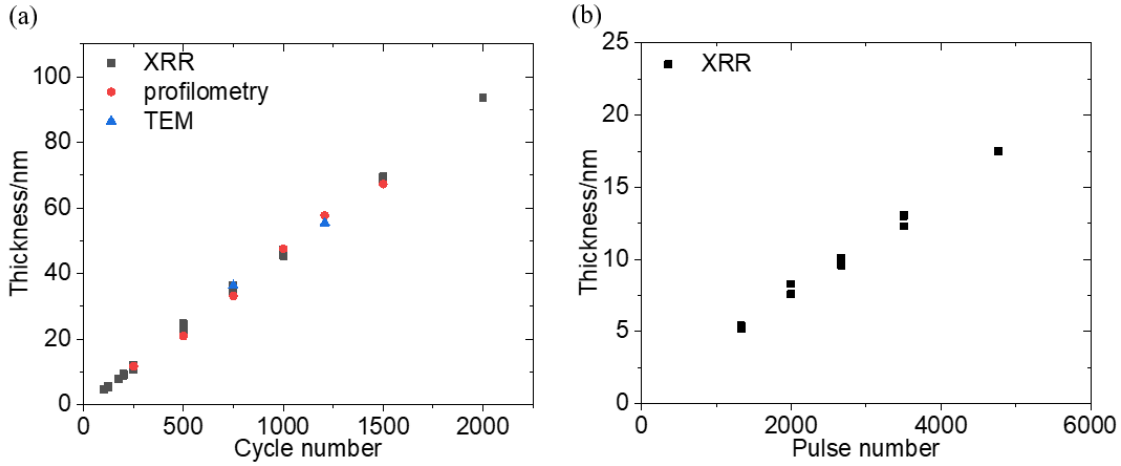

Fig. 3.12 Thickness measurements of TiO_2 films deposited by (a) ALD (thickness vs. cycle number) and (b) PLD (thickness vs. pulse number). X-Ray reflectivity (XRR), TEM, stylus profilometry are used to determine the thickness very precisely.

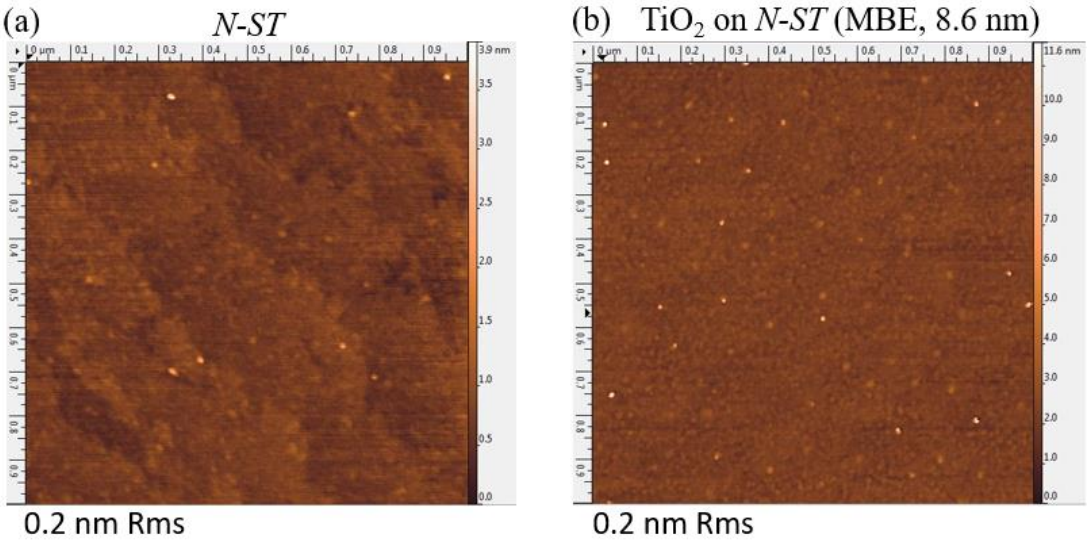

Fig. 3.13 AFM measurements of (a) *N-ST* and (b) TiO_2 on *N-ST* (deposited by MBE, thickness: 8.6 nm).

Fig. 3.13 shows one example of AFM measurements of *N-ST* and TiO_2 on *N-ST* (deposited by MBE), which indicates a high quality TiO_2 thin film with a mean roughness of 0.2 nm. Fig. 3.14 shows one example of atomic-resolution HAADF-STEM images of TiO_2 on *N-ST* (deposited by MBE), which confirms that the grown TiO_2 films are of good crystalline quality with atomically sharp interface, which is crucial for further electrochemical measurements.

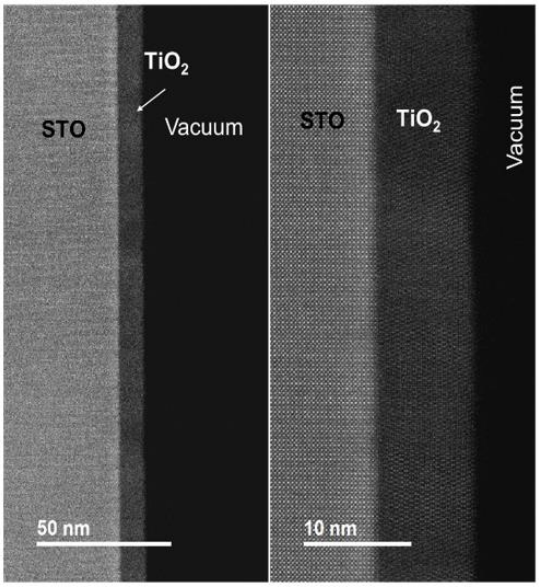

Fig. 3.14 Atomic-resolution HAADF-STEM images of TiO_2 on *N-ST* (deposited by MBE).

XPS data (Ru substrate) analysis

The surface chemistry of sputtered Ru substrate was characterized by XPS, which is vital to design accurate electrochemical measurements to deconvolute bulk and boundary storage contributions. First, the oxygen signal was observed for both samples (with or without air exposure) during the initial survey. After 10 min sputtering, the oxygen signal was completely gone for both samples but during the detailed measurements a bit of oxygen re-adsorbed on the sputtered area (Fig. 3.15 and Fig. 3.16).

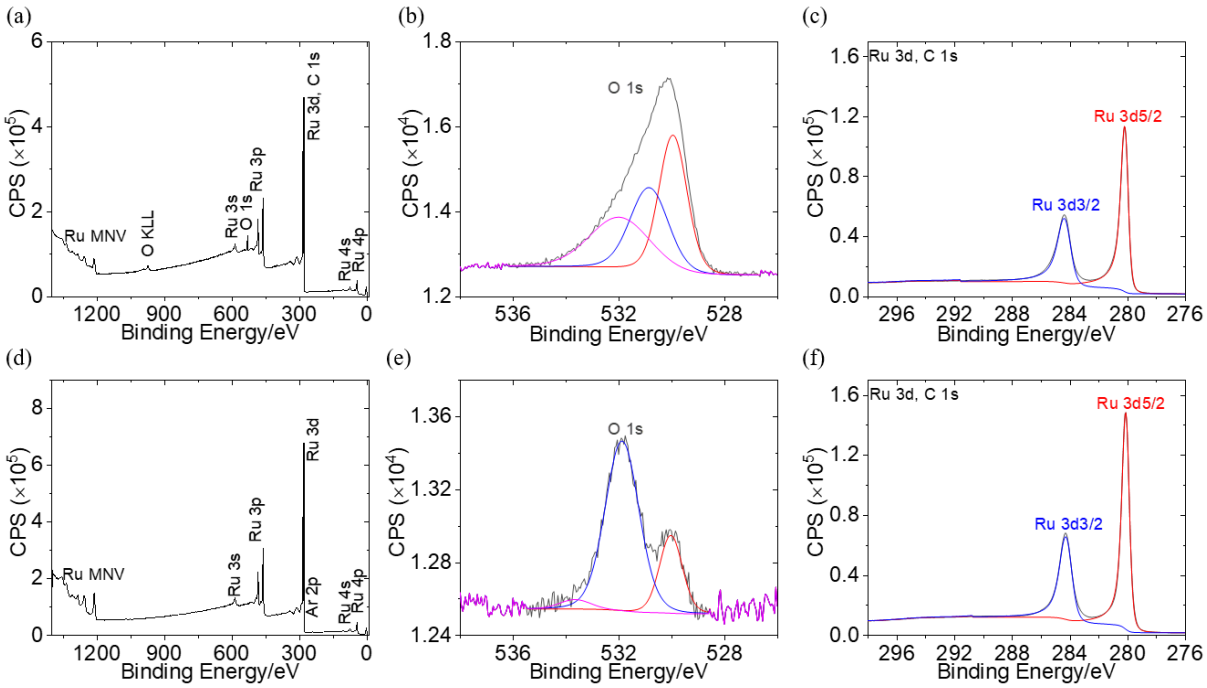

Fig. 3.15 XPS results of Ru substrate. (a), (b), (c) before sputtering; (d), (e), (f) after 10 min Ar sputtering. The sample was exposed to air before measurement and then transferred to the XPS chamber.

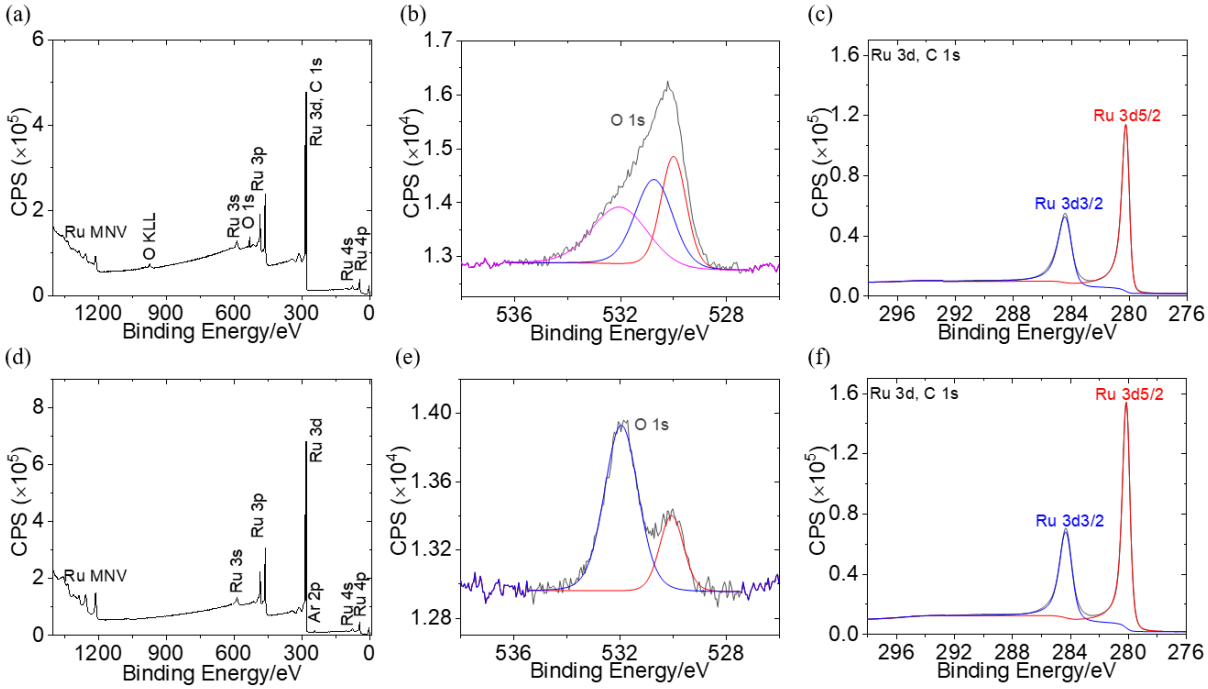

Fig. 3.16 XPS results of Ru substrate. (a), (b), (c) before sputtering; (d), (e), (f) after 10 min Ar sputtering. The sample was prepared in a glove box under Ar atmosphere ($O_2 \leq 0.1$ ppm, $H_2O \leq 0.1$ ppm) and transferred to the XPS chamber in an airtight transfer tool under Ar atmosphere.

The thickness of the surface oxide layer of the Ru substrate was estimated from the area of the Ru component before (I) and after sputtering (I_0) after a Tougaard background subtraction and using the following equation:

$$I/I_0 = \exp(-d/IMFP)$$

where d is the oxide thickness, and the inelastic mean free path (IMFP) was calculated with QUASES-IMFP calculator (http://www.quases.com/products/quases-imfp-tpp2m/). The calculations were performed for both Ru 3d and Ru 3p peak areas in order to get a better estimate on the error. The thickness of the surface oxide layer can be approximately estimated to be 0.5-0.7 nm for both samples (with or without air exposure, see Fig. 3.15 and Fig. 3.16, Table 3.3a, 3.3b and Table 3.4a, 3.4b).

Tables 3.3 and 3.4 give the peak areas, the kinetic energies and the IMFP for RuO_2 and RuO_4 and the estimated thicknesses from these values. Since the exact composition and structure of the

natural oxide is unknown, both RuO_2 and RuO_4 have been used to estimate the thickness of the layer of the oxidized Ru on top.

Regarding the Ru oxidation state on the surface oxide layer, RuO_2 is likely the predominant species according to literature and our measurements. Looking into the literature the binding energy of RuO_2 is only 0.6 eV higher than the one of Ru metal. Since Ru metal is quite asymmetric and the amount of oxidized Ru is rather low, this cannot be easily distinguished. However the binding energy shift for RuO_3 and RuO_4 compared to Ru is significantly larger - 2.4 eV and 3.2 eV, respectively. This should be visible in the XPS. Since any signature 3 eV above the main Ru peaks is not seen (Fig. 3.15 and Fig. 3.16), RuO_3 or RuO_4 would be excluded.

The two samples (with or without air exposure) show identical surface chemistry (an oxidic monolayer on the surface), which indicates that the oxide layer is stable at room temperature prohibiting further oxidation (owing to sluggish oxygen diffusion).

Table 3.3a The area of the Ru component (Ru 3d) before (I) and after sputtering (I_0), and the calculated thickness of the surface oxide layer of Ru substrate. The sample was exposed to air before measurement and then transferred to the XPS chamber.

	Ru 3d (E_{kin}=1200 eV)			
	IMFP (RuO_2)	IMFP (RuO_4)	I	Io
	1.98 nm	2.53 nm	241618	320658
Thickness	0.55 nm	0.72 nm		

Table 3.3b The area of the Ru component (Ru 3p) before (I) and after sputtering (I_0), and the calculated thickness of the surface oxide layer of Ru substrate. The sample was exposed to air before measurement and then transferred to the XPS chamber.

	Ru 3p (E_{kin}=1015 eV)			
	IMFP (RuO_2)	IMFP (RuO_4)	I	Io
	1.74 nm	2.22 nm	191102	257634
Thickness	0.52 nm	0.66 nm		

Table 3.4a The area of the Ru component (Ru 3d) before (I) and after sputtering (I_0), and the calculated thickness of the surface oxide layer of Ru substrate. The sample was prepared and transferred without air exposure.

	Ru 3d (E_{kin}=1200 eV)			
	IMFP (RuO_2)	IMFP (RuO_4)	I	Io
	1.98 nm	2.53 nm	244086	318640
Thickness	0.53 nm	0.67 nm		

Table 3.4b The area of the Ru component (Ru 3p) before (I) and after sputtering (I_0), and the calculated thickness of the surface oxide layer of Ru substrate. The sample was prepared and transferred without air exposure.

	Ru 3p (E_{kin}=1015 eV)			
	IMFP (RuO_2)	IMFP (RuO_4)	I	Io
	1.74 nm	2.22 nm	186037	254830
Thickness	0.55 nm	0.70 nm		

4

Lithium Storage in TiO_2 Films

4.1 Introduction

In this chapter (the core part of the thesis), to accomplish the main goal of deconvoluting bulk and interfacial storage and unifying supercapacitor and battery electrode concepts, TiO_2 thin films of high quality were utilized as model system.

Binary transition metal oxides (TMO) have been well-studied as battery electrode materials (*93*). Inserted Li^+ ions can be accommodated in and diffuse via interstices in the lattice, while donated electrons can be accommodated by changes in the transition metal valence state (*55*). TiO_2 has proven to be a particularly useful model material for investigating fundamental issues related to Li transport and storage (*53, 71, 94-99*). Several polymorphs of TiO_2 such as rutile (*95*), anatase (*100, 101*), and TiO_2(B) (*102-104*), which can host lithium, have been explored as possible negative electrode materials for lithium ion batteries (LIBs). The titania modification that is referred to in the thin films in this study is anatase, which has a tetragonal structure (space group $I4_1/amd$, number 141). It is well studied in terms of mechanism and performance of Li storage. Anatase is kinetically stable over a wide temperature range. In addition, anatase shows a modest volume change (~4%) (*105*) during the lithiation/delithiation process. The defect chemistry of anatase is well-understood (*53, 55, 98*). In particular, it has been shown that Li ions occupy interstitial positions in the bulk up to a concentration of at least δ=0.5 ($Li_\delta TiO_2$) compensated by conduction electrons in the Ti d orbitals (Ti^{3+}) (*106*). In $Li_{0.5}TiO_2$, based on theoretical calculations (*107, 108*) the Li ions are thought to be randomly located in half of the available interstitial octahedral sites.

The electrochemical measurements (battery storage capacity and bias dependent impedance measurements) and advanced electron microscopy measurements (STEM and EELS) were performed based on the aforementioned anatase TiO_2 thin films.

4.2 Materials and Methods

4.2.1 Electrochemical Experiments

Storage capacity measurements:

Electrochemical test cells were assembled in an argon-filled glove box ($O_2 \leq 0.1$ ppm, $H_2O \leq 0.1$ ppm), with the deposited TiO_2 thin film (10 × 10 mm) as working electrode, lithium metal disc (1.5 mm thick × 14 mm dia.,) cut from lithium metal foil (Alfa Aesar, 1.5 mm (0.06 in) thick × 19 mm (0.75 in) wide, 99.9% (metal basis), packing under argon) as the reference electrode. 1.0 M lithium hexafluorophosphate ($LiPF_6$) solution in a 1:1 vol/vol mixture of ethylene carbonate (EC) and dimethyl carbonate (DMC) was utilized as the electrolyte (Sigma-Aldrich, battery grade) and Whatman® glass microfiber (Grade GF/D) was used as separator. The stainless steel disc and spring were removed from the cells in order to decrease the background capacity. In addition to the typical cells consisting of TiO_2 thin film electrode inside, dummy cells (without TiO_2 thin films, only substrates) were also assembled for control experiments. To further reduce the background capacity, all the area of electrochemical test cells (except the sample) was blocked using an insulating layer (Kapton Tape).

The electronic conductivity of the lower donor doped, pure or acceptor doped *ST* is poor. Therefore, the samples need to be coated by carbon except the top surface (TiO_2 thin film, see Fig. 4.1b). A Leica ACE 600 sputter coater was used for carbon coating.

The true concentration of $LiPF_6$ electrolyte was measured by inductively coupled plasma optical emission spectroscopy (ICP-OES). In ICP-OES analysis, the dissolved sample was introduced into the inductively generated argon plasma via an atomizer system and excited. The emitted radiation was transferred to the ICP spectrometer where it was split into the individual wavelengths and evaluated. The intensities of the spectral lines were measured with CCD semiconductor detectors. Calibration was carried out with multi-element solutions mixed from standard solutions or single-element solutions.

Galvanostatic charge/discharge experiments of batteries were operated in a fixed potential window between 1.0-1.6 V to 3.0 V (versus Li) by using high-resolution Keithley source meters (Keithley 236 source measure unit, Keithley 237 high voltage source measure unit, Keithley 617

programmable electrometer, Keithley 2400 system source meter, Keithley 2634B system source meter, Keithley 2604B system source meter, Keithley 220 programmable current source and Keithley 6514 system electrometer) at room temperature. The capacity values of TiO_2 thin film were measured accurately under constant current (200 nA, 500 nA). The use of very thin films (1 – 15 nm) under rather low rates (extremely small currents) allows for reaching equilibrium within the times of measurements. The dummy cell capacity was measured and subtracted very precisely, which is vital for decoupling bulk and interfacial storage capacity accurately.

Bias dependent impedance measurements:

Electrochemical Impedance Spectroscopy (EIS) was employed to measure the interfacial resistance as well as interfacial capacitance. First, electrochemical test cells were assembled as mentioned above, which were kept at certain voltage for at least 3 weeks. Li contents in TiO_2 thin films can be controlled by varying voltage. Then the electrochemical test cell was disassembled in an argon-filled glove box ($O_2 \leq 0.1$ ppm, $H_2O \leq 0.1$ ppm). Ru was sputtered on both sides of the lithiated sample (Fig. 4.10) by DC sputtering (Emitech K575X, Ru target, Testbourne, 57mm dia. x 1.5mm thick, 99.95% Pure) and the prepared sample was transferred to the specially designed test cell (Fig. 4.10), which is airtight allowing argon flowing during measurement. All these operations were done in an argon-filled glove box ($O_2 \leq 0.1$ ppm, $H_2O \leq 0.1$ ppm). Then the measurement cell was placed in a thermostat in order to control temperature precisely. The measurements were conducted with a Novocontrol Alpha-A analyzer (Novocontrol Techologies, Germany, 2-wire measurement, 10^6 to $10^{-1} - 10^{-2}$ Hz, 0.01 V amplitude) applying various biases.

EIS induces a small voltage perturbation of varying frequency to yield a linear current response which is mathematically translated to the complex impedance (details about this technique can be found in Refs. (*7*) and (*109*)). At least two spectra were acquired at each condition (bias voltage) to confirm reproducibility. Impedance spectra were analyzed using ZView (Scribner Associates, Inc., USA, Version 3.5.c) by a respective equivalent circuit consisting of resistors (R), capacitors (C) and/or constant phase elements (CPE).

4.2.2 Electron Microscope Experiments (STEM and EELS)

The instruments information and experimental details have already been given in Chapter 3. One key point for lithiated samples emphasized here is that all bulk samples (especially lithiated samples) were transferred inside a sealed capsule from a glove box with Ar atmosphere ($O_2 \leq 0.1$ ppm, $H_2O \leq 0.1$ ppm) to the FIB vacuum chamber without air contact. The final FIB samples were mounted to TEM holders in a glove box ($O_2 \leq 0.1$ ppm, $H_2O \leq 0.1$ ppm) and transferred to TEM in the protective environment using a Melbuild vacuum transfer holder. All samples were kept in an inert environment and not exposed to air from electrochemical experiments to final TEM and EELS investigations.

4.3 Results and Discussion

4.3.1 Electrochemical Storage

The lithium uptake of TiO_2-films (the local storage capacity) as a function of film thickness was measured carefully for various electron-accepting substrates. The measurement set-ups are shown in Fig. 4.1. In addition to bulk lithium storage with a typical bulk value, the TiO_2 interface to an electron conductor such as doped $SrTiO_3$ (*ST*) or Ru can take up excess lithium through a space charge effect, leading to values beyond the bulk value. The interfacial storage in anatase has also been studied in terms of nanoparticles at different rates (*19, 55*).

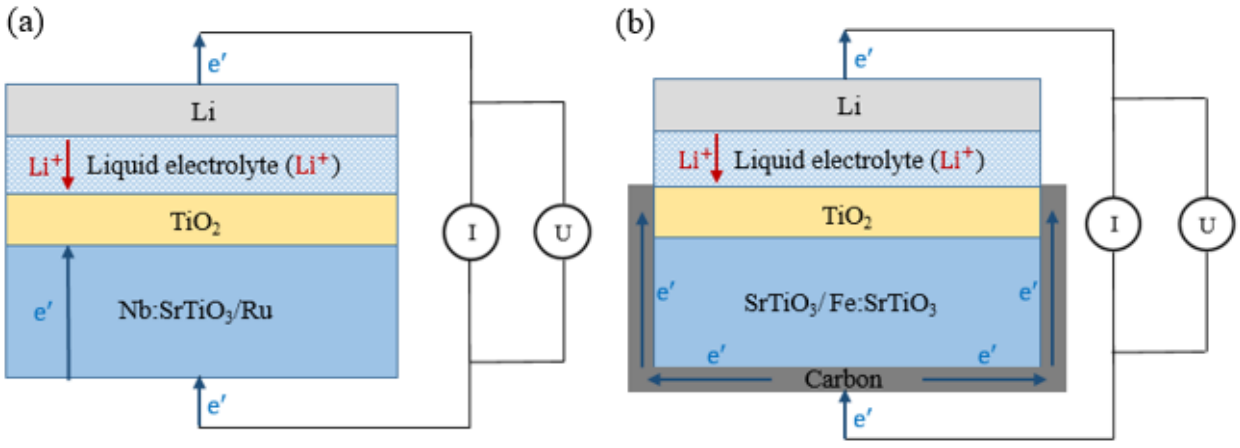

Fig. 4.1 Measurement set-ups: (a) storage experiment with a conductive substrate; (b) storage experiment with a non-conductive substrate.

4.3.1.1 Thickness Dependence

The storage capacity of TiO_2 on 0.5 wt% *N-ST* substrates as function of thickness was precisely measured (Fig. 4.2). The study of capacitance as function of thickness allows for separating bulk and boundary contributions, analogous to thin film studies of parallel conductances as function of thickness. In equilibrium, a straight line is expected with a slope that indicates the bulk storage capacity and an intercept that gives the excess boundary contribution. The battery storage capacity (the area (a) specific capacity (Q/a)), which depends linearly on the thickness (L), can be expressed as

$$Q/a = Q_{int}/a + q_{bulk}L = Q_{int}/a + c_{bulk}FL = Q_{int}/a + (\delta/V)FL \qquad (4.1)$$

whereby q_{bulk} denotes the neutral bulk charge density that is given by the L-independent bulk defect concentration δ/V where $\delta\ (= n_{Li}/n_{Ti})$ denotes the molar fraction and V the molar volume.

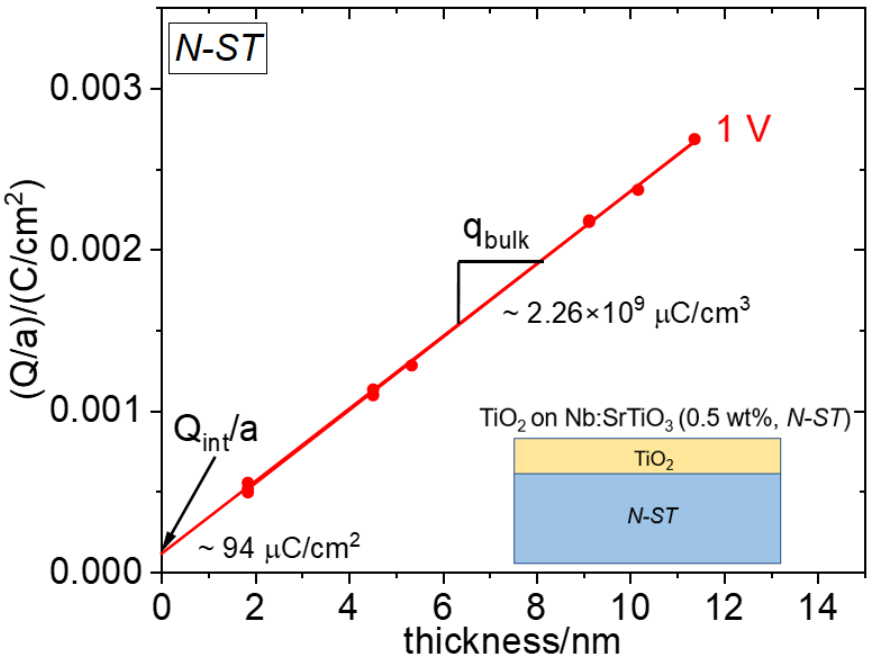

Fig. 4.2 Thickness dependent storage measurement: Area-specific capacity (Q/a) as function of thickness (TiO_2 on 0.5 wt% *N-ST* substrates). The bulk storage capacity (the slope) is $2.26(\pm 0.02) \times 10^9\ \mu C/cm^3$ and the interfacial storage capacity (the intercept) is $94(\pm 15)\ \mu C/cm^2$ in the case of 1 V versus Li. TiO_2 films were deposited by atomic layer deposition (ALD).

Fig. 4.2 presents a collection of representative storage experiments of titania thin films (on 0.5 wt% *N-ST* substrates) as a function of thickness. The Li-uptake of a dummy cell has been carefully measured and subtracted. The bulk storage capacity (the slope) is $2.26(\pm 0.02) \times 10^9\ \mu\mathrm{C/cm^3}$. Extrapolating the capacity values to zero thicknesses gives the interfacial storage capacity (the intercept) of $94(\pm 15)\ \mu\mathrm{C/cm^2}$. The measured bulk and boundary contributions correspond to typical values for anatase (*19, 106, 110*). Even though the boundary storage capacity is relatively high, it is not inconsistent with monolayer result. As a consistency check, the limit of a fully occupied first layer in titania within a discrete picture (*81*) is assumed. A maximum value of $850\ \mu\mathrm{C/cm^2}$ is estimated since two interstitial sites per Ti are available (*106*). In reality, the limiting factor may be to accumulate the equivalent amount of electrons in the substrate.

To estimate the amount of stored electrons in the *ST* substrate, a Gouy-Chapman profile is considered. The equilibrium space charge profile can be written as (*7*)

$$\frac{\mathrm{d}^2 \ln \zeta_n}{\mathrm{d}\xi^2} = \frac{1}{2}(\zeta_n - \zeta_n^{-1}) \tag{4.2}$$

where the parameter ζ is the concentration enhancement (the concentration relative to that in the bulk (c_∞)), i.e. $\zeta_n = \frac{c_n(x)}{c_{n\infty}}$, and ξ is the local coordinate normalized to the Debye length ($\xi = \frac{x}{\lambda}$).

In the case of pronounced space charge effects, the depleted positive charge becomes unimportant for the charge density very rapidly. Then the simplified space charge profile can be obtained as

$$\frac{\mathrm{d}^2 \ln \zeta_n}{\mathrm{d}\xi^2} = \frac{1}{2}\zeta_n \tag{4.3}$$

Using $\ln \zeta_n = \ln a + b \ln(1 + c\xi)$, the electron concentration can be obtained as

$$c_n(x) = \frac{c_{n0}}{\left(1 + \sqrt{\frac{c_{n0}}{c_{n\infty}}}\frac{x}{2\lambda}\right)^2} \tag{4.4}$$

Clearly, c_{n0} is a formal value and may be greater than the realistic value in a discrete picture. c_{n0} can be estimated from equating the integral over the first layer with the first-layer result of a discrete picture (*81*). (c'_{n0}: single layer model $105\ \mu\mathrm{C/cm^2}$, each Ti takes up one electron, see Fig. 4.3)

$$\int_a^0 c_n(x)dx = ac'_{n0}$$

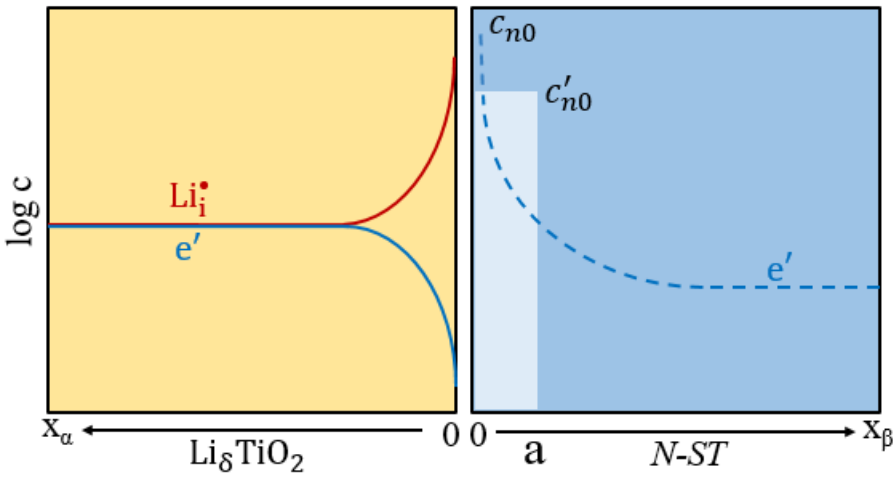

Fig. 4.3 Schematic representation of charge storage in *ST* substrate. (Gouy-Chapman profile and single-layer model in a discrete picture.)

where a is the lattice parameter of *ST*. Then the following equation can be obtained

$$2\lambda\sqrt{c_{n0}c_{n\infty}}\left[1-\left(1+\sqrt{\frac{c_{n0}}{c_{n\infty}}}\frac{a}{2\lambda}\right)^{-1}\right]=ac'_{n0} \tag{4.5}$$

The only unknown c_{n0} can be obtained when $c_{n\infty}$ and λ are given. The screening length for the *ST* substrate is a few to tens of nanometers, depending on the dopant content. The total stored charge can be calculated by integration of concentration from 2λ to 0.

$$Q=\int_{2\lambda}^0 c_n(x)dx=2\lambda\sqrt{c_{n0}c_{n\infty}}\left(1-\frac{1}{1+\sqrt{\frac{c_{n0}}{c_{n\infty}}}}\right) \tag{4.6}$$

For the realistic situation, $c_{n0}\sim 5c'_{n0}$, gives a maximum stored charge Q of 140 $\mu C/cm^2$, which indicates the measured value to be on the safe side.

In addition, partial association (of Li^+ and e^-) across the double-layer is probable (*19*, *98*) ("pseudocapacitive contributions"), which will make the rather high value more expectable. Partial association is already expected in the bulk (*98*). In the space charge zones, part of the associated defects split at the expense of the overall amount of the neutral species (*111*, *112*).

In the context of this study, it is remarkable that not only bulk and boundary storage can be accurately separated, but that they can be traced back to a common thermodynamic framework, namely the generalized defect-chemical concept (*28*), which is reflected in the spatial distribution of ionic and electronic charge carriers. The entire Li^+ profile can be quantitatively given as a function of the positional coordinate (x) with temperature, pressure, doping content (C) and Li-activity a_{Li} (cell voltage) as control parameters. The relevant materials parameters are the defect-chemical mass action constants, which rely on the energetic properties of the electrode and substrate. For dilute conditions at given temperature and pressure:

$$c_{Li^+} = \mathrm{fct}\left(x, a_{Li}, C;\ \mu^0_{eon}(\mathrm{substrate}), \mu^0_{eon}(TiO_2), \mu^0_{ion}(TiO_2)\right) \tag{4.7}$$

where the μ^0- parameters are the standard chemical potentials of the respective charge carriers (here referring to conduction electrons and interstitial Li-ions).

This important point will be discussed later. In the next two sections the two most important parameters (Li-activity (different degrees of storage) and doping content (substrate effects)) will be addressed.

4.3.1.2 Different Degrees of Storage

Fig. 4.4 presents the results of area-specific storage capacity (Q/a) as function of thickness at different degrees of storage (from 1.6 V to 1.0 V versus Li, TiO_2 on 0.5 wt% *N-ST* substrates). Fig. 4.4a gives the results for bulk (slope) and boundary values (intercept) for seven different equilibrium voltages, which increase with increasing Li-activity. As both bulk and boundary values depend differently on the Li activity (Fig. 4.4b), the ratio of the two storage capacities, which are linked to each other, varies with Li content. The power laws for Q as a function of the lithium activity (power: *N*) are different for bulk ($N \geq 1/2$) and for boundary ($N \leq 1/4$) from the dilute thermodynamic framework, which will be addressed in detail later. The *N*-values, measured and displayed in Fig. 4.4a, are evident to surpass the dilute limit (0.035 for the bulk and 0.021 for the boundary), due to the expected crystallographic and electronic saturation effects, leading to a flattening of the $Q(a_{Li})$ curve. Saturation will set in earlier for the boundaries owing

to the dilute exponents, and the tendency for the ratio is expected to be reversed, which is indeed seen in Fig. 4.5.

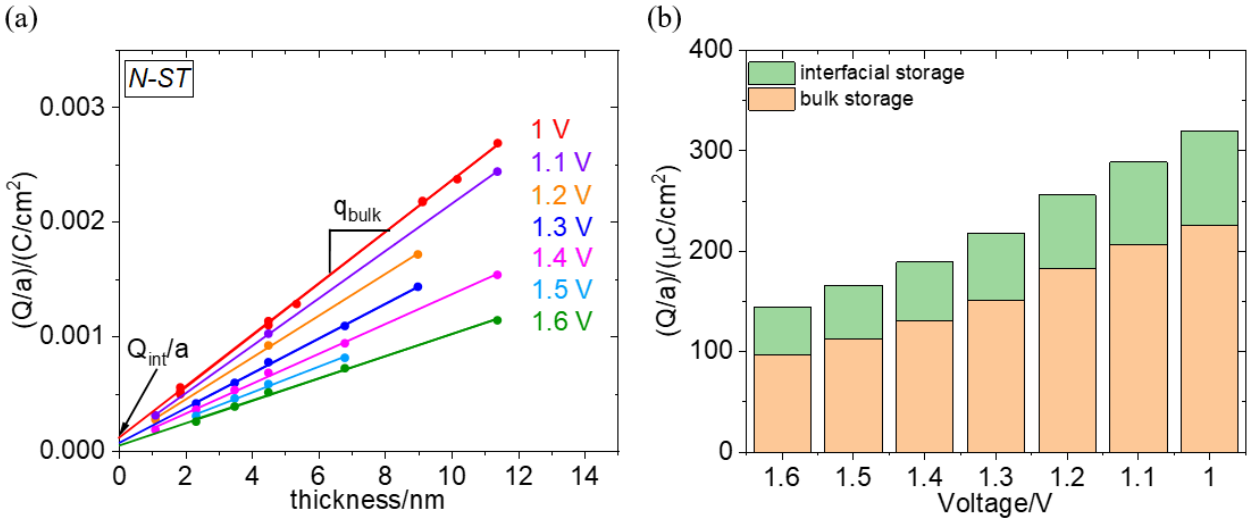

Fig. 4.4 Storage measurement: (a) Area-specific capacity (Q/a) as function of thickness at different degrees of storage (TiO_2 on 0.5 wt% *N-ST* substrates). The bulk storage capacities (the slopes) are 2.26, 2.07, 1.83, 1.51, 1.30, 1.13, $0.97 \times 10^9\ \mu C/cm^3$ and the interfacial storage capacities (the intercepts) are $94, 82, 75, 66, 59, 54, 48\ \mu C/cm^2$ in the case of 1 V to 1.6 V versus Li, respectively. (b) Interfacial (Q_{int}/a) and bulk ($q_{bulk}L$, normalized to 1 nm) storage capacity as function of voltage (Li-activity). TiO_2 films were deposited by atomic layer deposition (ALD).

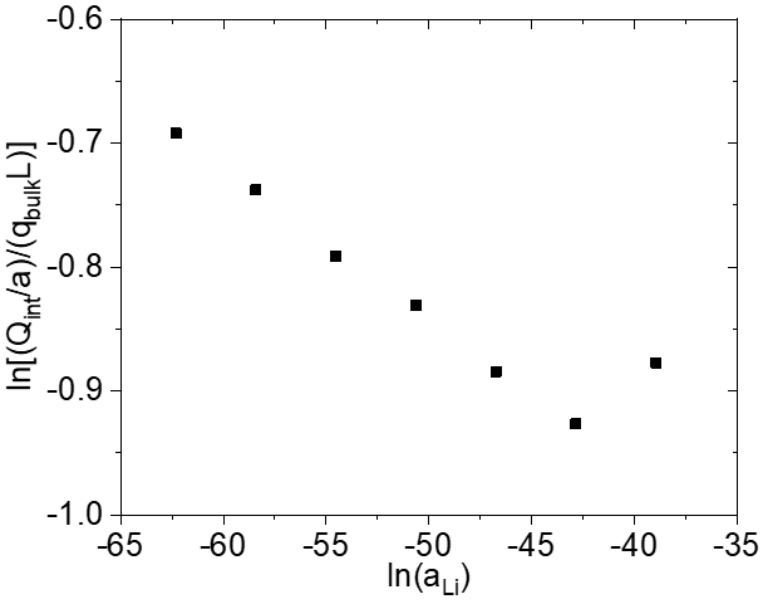

Fig. 4.5 The ratio of boundary and bulk storage as function of Li-activity (degree of storage). (TiO_2 on 0.5 wt% *N-ST* substrates). The numerical value of the gradient indicates non-dilute situations.

4.3.1.3 Substrate Effects

The effect of the electronic situation in the substrate, which affects the Li-uptake in TiO_2, will be addressed in this section. The mass action law for the bulk storage indicates that the Li-uptake should decrease with increasing electron concentration already present in the material ($c_{n\infty}$) for similar chemistry (similar mass action constants), due to the amount of active electrons being given by $c_n(x) = c_{n\infty} + (Q(x)/F)$ (entropic effect, see following detailed discussion). This effect is particularly relevant when it comes to interfacial storage using differently doped *ST* substrates (C). As a result, the capacity should increase from more highly donor doped *ST* to lowly doped, from donor doped to undoped, from undoped to acceptor doped (Fe doped $SrTiO_3$ (*F-ST*)). This is impressively corroborated by experimental results (Fig. 4.6) displaying the same sequence for the interfacial capacities. The bulk storage capacity stays constant due to same Li-activity. Regarding higher donor doped *ST*, the typical set-up (Fig. 4.1a) was used, while a slightly different measuring set-up had to be used (Fig. 4.1b) due to the poor electron conductivity of the pure or acceptor doped *ST*. High doping contents may also effect the incorporation energetically (mass action constant), which is discussed in the following paragraph.

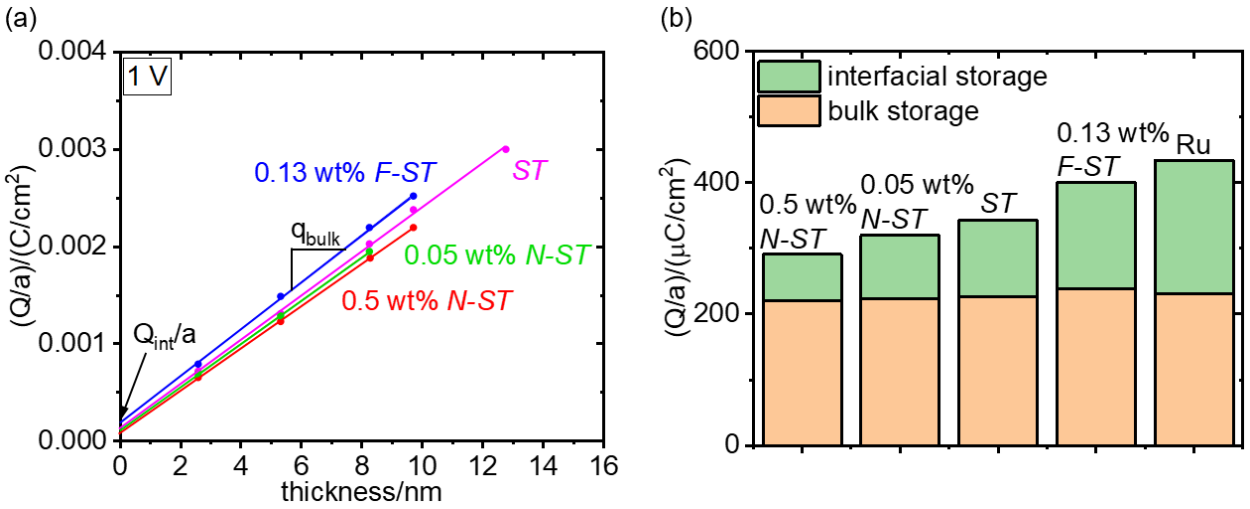

Fig. 4.6 Storage measurement: (a) Area-specific capacity (Q/a) as a function of thickness for differently doped substrates (0.13 wt% *F-ST*, *ST*, 0.05 wt% *N-ST* and 0.5 wt% *N-ST* substrates) at 1V. The bulk capacities (the slopes) are 2.40×10^9, 2.27×10^9, 2.23×10^9 and 2.20×10^9 $\mu C/cm^3$ and the interfacial storage capacities (the intercepts) are 161, 116, 97 and 71 $\mu C/cm^2$ for 0.13% *F-ST*, *ST*, 0.05 wt% *N-ST* and 0.5 wt% *N-ST* substrates, respectively. (b) Interfacial (Q_{int}/a) and bulk ($q_{bulk}L$, normalized to 1 nm) storage capacity for different substrates (pure and differently doped *ST* substrates as well as Ru substrate). TiO_2 films were deposited by pulsed laser deposition (PLD) and molecular beam epitaxy (MBE).

Not surprisingly, the highest interfacial storage capacities are obtained if *ST* is replaced by Ru, because Ru has expectedly a more favorable heterogeneous mass action constant, essentially due to the lower energy for accepting excess electrons ($\mu^0_{eon}(substrate)$), resulting from the noble character of the metal. The atom density of hexagonal close-packed Ru substrate is 1.58×10^{15} cm^{-2}. The stored charge is calculated to be 250 $\mu C/cm^2$ if each Ru atom at first layer takes up one electron, which exceeds the value measured (Figs. 4.6b, 4.7). The results for Ru may be complicated by an oxidic monolayer (as observed in XPS), which would be expected to undergo a local conversion reaction (*113*). Since the capacity of the dummy cell was subtracted (i.e., same cell without TiO_2), the results should nonetheless be reliable.

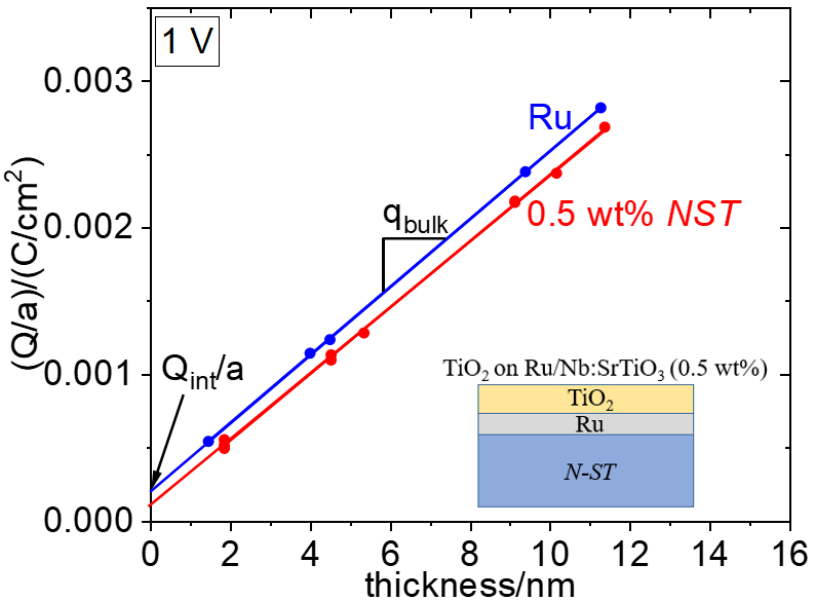

Fig. 4.7 Storage measurement: Area-specific capacity (Q/a) as function of thickness for different substrates (Ru and 0.5 wt% *N-ST* substrates) at 1 V. The bulk storage capacities (the slopes) are 2.31×10^9, 2.26×10^9 $\mu C/cm^3$ and the interfacial storage capacities (the intercepts) are 203 and 94 $\mu C/cm^2$ for Ru and 0.5 wt% *N-ST*, respectively. TiO_2 films were deposited by atomic layer deposition (ALD).

To highlight the effect of the substrate (S) with respect to the capability to accommodate electrons and hence to help interfacial storage, it suffices to consider small storage and to ignore the electric potential drop. Applying the mass action law for

$$\mathrm{Li} + V_i(\mathrm{TiO_2}) \rightleftharpoons \mathrm{Li}_i^{\cdot}(\mathrm{TiO_2}) + \mathrm{e}'(\mathrm{S}) \tag{4.8}$$

referring to the outermost sites yields

$$a_{\mathrm{Li}} \cdot K_{het} = c_{i0}(\mathrm{TiO_2}) \cdot c_{n0}(\mathrm{S}) \tag{4.9}$$

For simplicity, Gouy-Chapman layers are considered

$$Q \propto \sqrt{c_{i0}(\mathrm{TiO_2})} = \sqrt{c_{n0}(\mathrm{S})} \tag{4.10}$$

It follows that

$$a_{\mathrm{Li}} \cdot K_{het} \propto Q^4 \tag{4.11}$$

For the same K_{het} and the same a_{Li}, Q is fixed if the background defect (index ∞) is neglected. If this is not the case e.g., for the substrate side, then $c_n(x) = c_{n\infty} + (Q(x)/F)$, whereby $c_{n\infty}$ is not

negligible. Then Q must be smaller for given a_{Li} and K_{het}. This is directly seen from Eq. (4.9). If e.g., $c_{n0} \simeq c_{n\infty}$, then $c_{n0}(\mathrm{S})$ is almost unchanged and Q very small.

In order to drive this point home, a simple example characterized by a single-layer storage on both sides is considered, assuming identical dielectric constants and dilute conditions. (Note that this is not a realistic example since single-layer storage implies non-dilute conditions.) (*114*) Li^+ bulk concentration on the TiO_2 side is neglected, but the bulk electron concentration on the substrate side is taken account of, that is fixed by the donor content (C). Then the condition $Q(\mathrm{TiO_2}) = Q(\mathrm{S})$ means that

$$c_{n0}(\mathrm{S}) - C = c_{i0}(\mathrm{TiO_2}) \tag{4.12}$$

Combination with Eq. (4.9) leads to $c_{n0}(\mathrm{S})(c_{n0}(\mathrm{S}) - C) = a_{\mathrm{Li}}K_{het}$, with the solution

$$c_{n0}(\mathrm{S}) = \frac{C}{2} + \sqrt{\frac{C^2}{4} + a_{\mathrm{Li}}K_{het}}$$

or

$$Q \propto c_{n0}(\mathrm{S}) - C = \sqrt{\frac{C^2}{4} + a_{\mathrm{Li}}K_{het}} - \frac{C}{2}$$

If C is very large, $Q \simeq 0$. If C is negligible $Q(C = 0) \equiv Q_0 = \sqrt{a_{\mathrm{Li}}K_{het}}$. The effect of C on Q is best seen if C is not negligible but small compared to $2\sqrt{a_{\mathrm{Li}}K_{het}}$, then the square root term can be expanded and the following relation can be obtained as first approximation.

$$\frac{Q}{Q_0} \simeq 1 - \frac{C}{2\sqrt{a_{\mathrm{Li}}K_{het}}} \tag{4.13}$$

Apart from this entropic effect, an energetic effect also needs to be considered. If the substrate is heavily doped or even chemically changed, then K_{het} has to vary since

$$K_{het} \propto \exp - \frac{\mu_i^0(\mathrm{TiO_2}) + \mu_n^0(\mathrm{S})}{RT} \tag{4.14}$$

A lower electronic level ((free) energy) in the substrate ($\mu_n^0(S)$) severely increases K_{het} and hence Q at given a_{Li}. This is the case where *ST* is replaced by Ru. More accurately, the density of states in the conduction band of the substrate becomes important.

In this section, electrochemcial measurements of TiO_2 thin films as fucntion of thickness were performed, with the nature of the substrates and the degree of storage as control parameters. As a result, bulk and boundary contributions have been precisely deconvoluted and a generalized thermodynamic picture is obtained. Before moving to the electrochemical impedance sections, two more points are emphasized here.

First, Nb_2O_5 has also been investigated in a similar way, as a comparison to the TiO_2 model system. As shown in Fig. 4.9, the interfacial storage capacity of Nb_2O_5 films is lower than that of TiO_2 films. One possible reason is that bulk storage capacity of Nb_2O_5 is much higher than of TiO_2. It is not favorable to take up extra Li. The other possibility is that the contact of Nb_2O_5 with *N-ST* leads to a higher Nb content in *ST* (at least close to the contact). The effective donor doping content is then higher than 0.5 wt% at surface layer, leading to less interfacial storage.

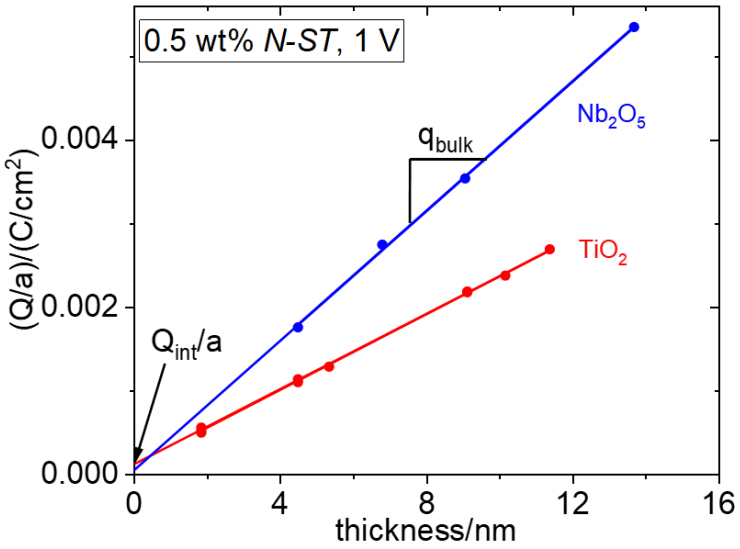

Fig. 4.8 Storage measurement: Area specific capacity (Q/a) as function of thickness for TiO_2 and Nb_2O_5 thin films (on 0.5 wt% *N-ST* substrates). The bulk storage capacities (the slopes) are $2.26, 3.87 \times 10^9\ \mu C/cm^3$ and the interfacial storage capacities (the intercepts) are $94, 41\ \mu C/cm^2$ for TiO_2 and Nb_2O_5 thin films, respectively.

In order to clarify the reliability and accuracy of the presented measurements and data analysis, more experimental details/results are given and explained as follows:

1. The electrochemical measurement cells were operated in the potential window 3 V - 1 V. Therefore, solid electrolyte interphase (SEI) formation is not expected (*115*, *116*), which should have a negligible influence on the analysis of storage capacity. Experimentally, SEI is not observed by TEM.

2. Should interfacial charging of electrolyte/positive electrode (substrate or TiO_2) play a role, it is expected that the double layer capacity of the dummy cell (electrolyte/substrate interface) is higher than that of the measurement cell (with TiO_2 thin films, electrolyte/TiO_2 interface), which could lead to an even higher interfacial storage value.

3. Reliable and precise storage capacity measurement is key for deconvoluting bulk and interfacial storage. The optimized measurement details are given in “Materials and Methods” section. Some measurements were repeated up to 5 times using different films to confirm data reproducibility. For example, five dummy cells (with *ST* substrate) were measured using a current of 200 nA under a potential window of 3 V - 1 V, giving a capacity of $(230 \pm 13)\ \mu C$ (the scatter is less than six

percent, see Table 4.1). All the other dummy cells (0.5 wt% *N-ST*, at different voltages) give capacities with a less than seven percent scatter (Table 4.2). Similarly the electrochemical cells (with TiO_2 films) were measured reliably with a scatter of less than four percent (e.g., Fig. 4.9 and Table 4.3a, b, c). As Fig. 4.9 (see also Table 4.3a, b, c) shown, for each thickness (including pure substrate), at least two samples were measured, which are almost identical, indicating the reliability of storage capacity measurements. Overall, considering the three contributions for the errors: a) reproducibility and precision of the measurements (the error is less than 4%), b) accuracy of the linear regression, and c) subtraction of the blank value (the error is less than 7%). As a result, the determination of the interfacial contribution has a sufficient significance (average less than 30%). The bulk contribution shows a minor inaccuracy of about 1-3% (Table 4.4a, b, c).

4. As discussed in Chapter 3, TiO_2 thin films were deposited by three methods (ALD, PLD and MBE). ALD turned out to be appropriate only for highly donor doped substrates (0.5 wt% *N-ST*). In terms of lowly donor doped, un-doped and acceptor doped *ST* substrates, there is always an amorphous layer between substrate and TiO_2 thin films (Fig. 4.10). PLD and MBE turned out to be the adequate techniques to prepare TiO_2 thin films on all *ST* substrates (highly donor doped, lowly donor doped, un-doped and acceptor doped *ST* substrates). In this thesis, TiO_2 thin films deposited by the same method were used to investigate a single effect whenever it is possible. (e.g., the films deposited by ALD were used for the study of effect of different storage degrees and the ones deposited by PLD for the substrate effects study). When the storage capacity results are compared, the bulk values are identical; the boundary values differ to some degree (the values from ALD samples are a bit higher than those from PLD samples). This is expected as the quality and detailed nature of the surface depend on it. Whenever there was the possibility to compare under same conditions, it was found that the variation is within the inaccuracy for a given method.

In addition, thickness control and measurement are equally important. All three techniques (XRR, profilometry, TEM) give consistent results of deposited films (Fig. 3.12 and Table 3.2). GIXRD and XRR results evidence high quality of TiO_2 thin films (on differently doped *ST* substrates) and confirm the reliability of film deposition (Figs. 3.9 - 3.11).

5. In the voltage range of interest, RuO_x on the surface of Ru metal should be converted to Ru and Li_2O so that in addition to Ru/TiO_2 interfaces, one has to consider Ru/Li_2O interfaces. The latter contribution should cancel in the subtraction of the dummy results.

Table 4.1 Dummy cell capacity of differently doped *ST* substrates at 1 V.

Capacity/μC					Average/μC
0.5 wt% *N-ST*	0.1 wt% *N-ST*	0.05 wt% *N-ST*	*N-ST*	0.13 wt% *F-ST*	
221	225	234	251	217	230 ± 13

Table 4.2 Dummy cell capacity of 0.5 wt% *N-ST* at different voltages (1.4 - 1.6 V).

Dummy cell	Capacity/μC		
	1.4 V	1.5 V	1.6 V
1	45	37	30
2	44	37	30
3	40	33	27
4	41	34	28
Average	42.4 ± 2.6	35.1 ± 2.2	28.7 ± 1.7

Table 4.3a Storage capacity of TiO_2 films (deposited by ALD) of different thicknesses (on 0.5 wt% *N-ST*) at 1 V. The error is less than 4%.

TiO_2 thickness	Capacity/μC		
	1.9 nm	4.5 nm	9.1 nm
Sample 1	490	1130	2170
Sample 2	510	1090	2180

Table 4.3b Storage capacity of TiO_2 films (deposited by ALD) of different thicknesses (on 0.5 wt% *N-ST*) at 1.2 V. The error is less than 2%.

TiO_2 thickness	Capacity/μC at 1.2 V		
	N-ST	1.1 nm TiO_2	4.5 nm TiO_2
Sample 1	59	330	973
Sample 2	62	328	979

Table 4.3c Storage capacity of TiO_2 films (deposited by ALD) of different thicknesses (on 0.5 wt% *N-ST*) at 1.6 V. The error is less than 2%.

TiO_2 thickness	Capacity/μC at 1.6 V		
	N-ST	3.5 nm TiO_2	4.5 nm TiO_2
Sample 1	30	414	533
Sample 2	30	409	529
Sample 3	27		
Sample 4	28		

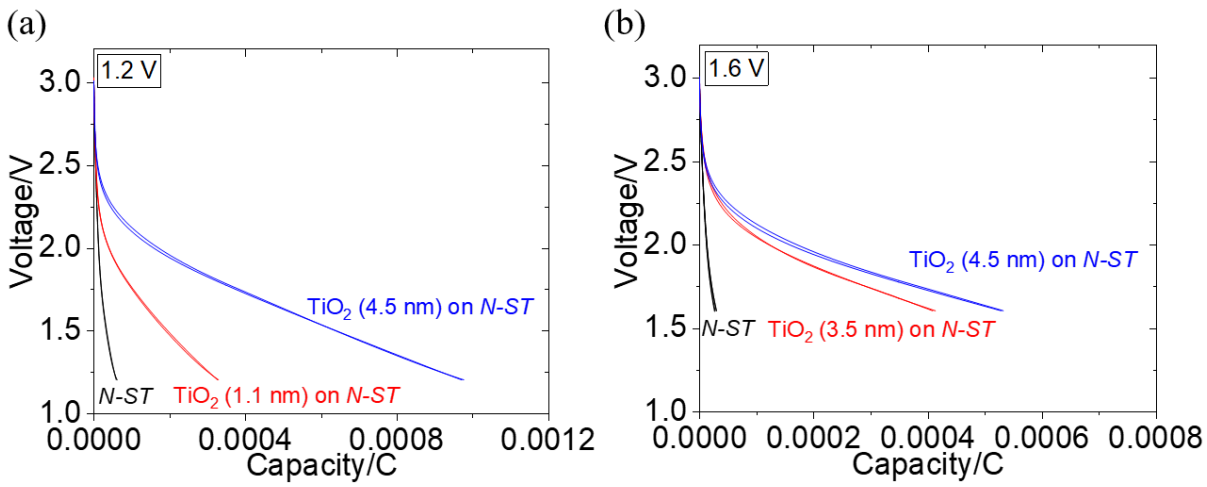

Fig. 4.9 Discharge curves (voltage vs. capacity) of dummy cell (with 0.5 wt% *N-ST*) and TiO_2 thin films (on 0.5 wt% *N-ST* substrates) at 1.2 V (a) and 1.6 V (b). For each thickness (including pure substrate), at least two samples were measured, which are almost identical, indicating the reliability of storage capacity measurements. It is obvious that the respective data points fall on the same line.

Table 4.4a Bulk storage capacity (the slope, q_{bulk}) and interfacial storage capacity (the intercept, Q_{int}/a) of TiO_2 thin films at different degrees of storage (voltage, Li-activity) (TiO_2 (deposited by ALD) on 0.5 wt% *N-ST* substrates).

Voltage (Li-activity)/V	Bulk storage capacity (the slope)/ $\mu C/cm^3$	Interfacial storage capacity (the intercept)/ $\mu C/cm^2$
1.6	$0.97(\pm 0.03) \times 10^9$	48 ± 19
1.5	$1.13(\pm 0.06) \times 10^9$	54 ± 16
1.4	$1.30(\pm 0.03) \times 10^9$	59 ± 16
1.3	$1.51(\pm 0.03) \times 10^9$	66 ± 16
1.2	$1.83(\pm 0.03) \times 10^9$	73 ± 19
1.1	$2.07(\pm 0.01) \times 10^9$	82 ± 8
1.0	$2.26(\pm 0.02) \times 10^9$	94 ± 15

Table 4.4b Bulk storage capacity (the slope, q_{bulk}) and interfacial storage capacity (the intercept, Q_{int}/a) of TiO_2 on 0.5 wt% *N-ST* and Ru substrates at 1 V (TiO_2 thin films were deposited by ALD).

Substrate	Bulk storage capacity (the slope)/ $\mu C/cm^3$	Interfacial storage capacity (the intercept)/ $\mu C/cm^2$
0.5 wt% *N-ST*	$2.26(\pm 0.02) \times 10^9$	94 ± 15
Ru	$2.31(\pm 0.01) \times 10^9$	203 ± 8

Table 4.4c Bulk storage capacity (the slope, q_{bulk}) and interfacial storage capacity (the intercept, Q_{int}/a) for TiO_2 thin films on differently doped substrates (0.5 wt% *N-ST*, 0.05 wt% *N-ST*, *ST*, 0.13 wt% *F-ST*) at 1 V (TiO_2 thin films were deposited by PLD and MBE).

Substrate	Bulk storage capacity (the slope)/ $\mu C/cm^3$	Interfacial storage capacity (the intercept)/ $\mu C/cm^2$
0.5 wt% *N-ST*	$2.20(\pm 0.02) \times 10^9$	71 ± 11
0.05 wt% *N-ST*	$2.23(\pm 0.02) \times 10^9$	97 ± 12
ST	$2.27(\pm 0.05) \times 10^9$	116 ± 20
0.13 wt% *F-ST*	$2.40(\pm 0.04) \times 10^9$	161 ± 29

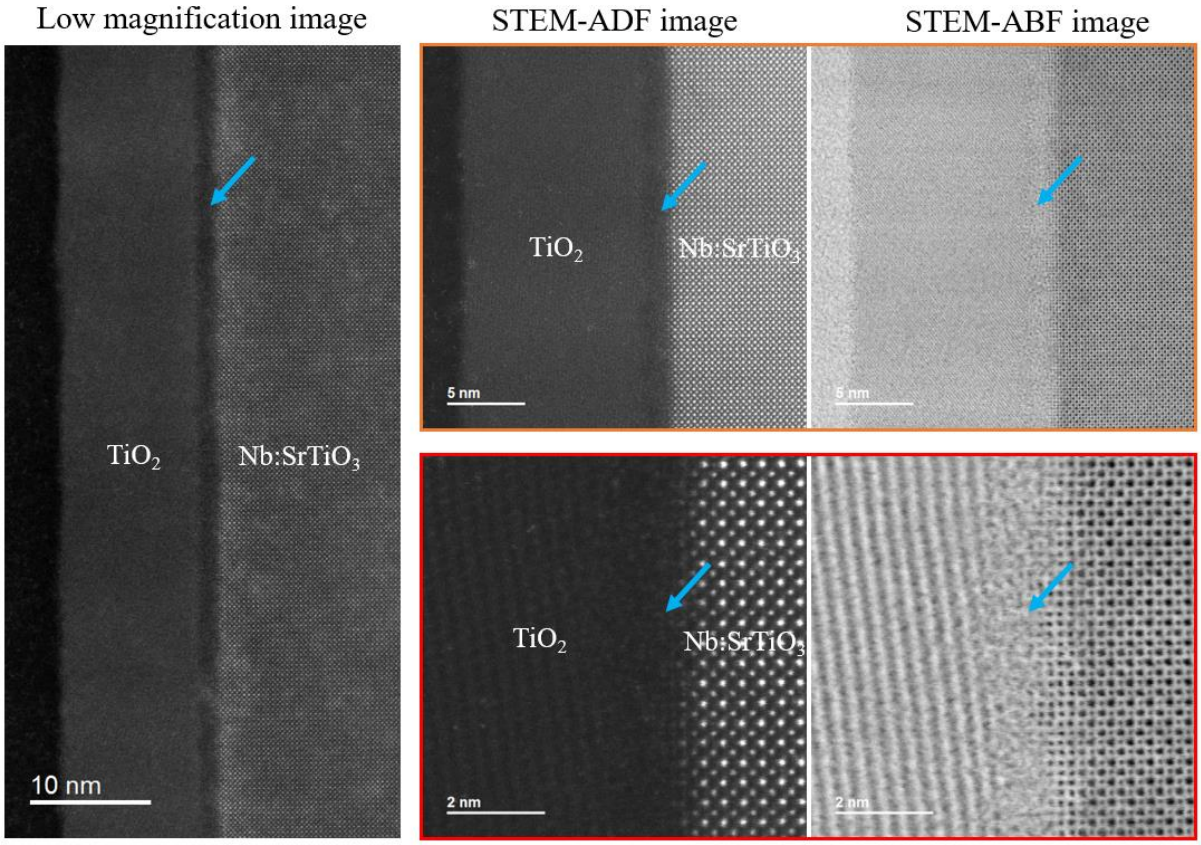

Fig. 4.10 Atomic-resolution HAADF-STEM images (along the cross-sectional direction) of TiO_2 sample deposited by ALD (on lowly Nb doped *ST* substrate (0.05 wt%)). There is an amorphous layer between substrate and deposited TiO_2 thin film.

4.3.2 Electrochemical Impedance

Charge redistribution at the interface region also plays a very important role for the transport properties. Therefore, bias dependent impedance measurements (across the interfaces) are performed, yielding interfacial resistance as well as interfacial capacitance, to investigate the interfacial contributions. The results of battery capacity measurements show that space charge effects at the Ru/TiO_2 interface are more pronounced, leading to a higher interfacial storage capacity. Consequently, in terms of the perpendicular electric measurements the most resistive interface is the Ru/TiO_2 interface (see the cell arrangement given in Fig. 4.11).

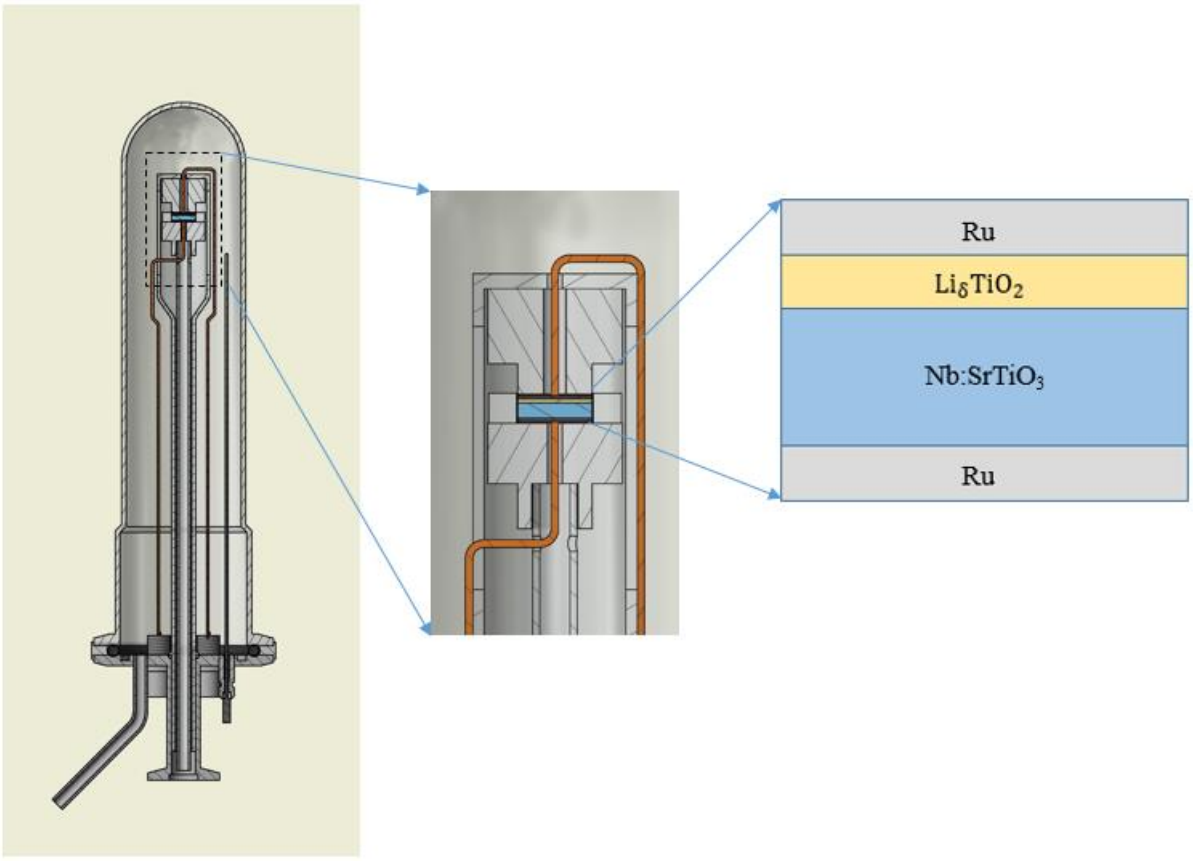

Fig. 4.11 Sketch of specially designed test cell for bias dependent impedance measurements.

To evaluate the response of resistance and capacitance as a function of bias, Li-interstitials (i) and excess electrons (n) are referred to and a Gouy-Chapman profile is considered. Both defects are in spatial equilibrium. In the TiO_2 bulk, $c_{n\infty}(TiO_2) = c_{i\infty}(TiO_2) = c_\infty$. Owing to

$$\frac{c_{ix}(\mathrm{TiO_2})}{c_\infty} = \frac{c_\infty}{c_{nx}(\mathrm{TiO_2})} = e^{-\frac{F(\phi-\phi_\infty)}{RT}} \tag{4.15}$$

the integral of $\frac{1}{c_{nx}(\mathrm{TiO_2})}$ leads to

$$\int \frac{1}{c_{nx}(\mathrm{TiO_2})}dx = \frac{1}{c_\infty^2}\int c_{ix}(\mathrm{TiO_2})dx = 2\lambda\frac{1}{c_\infty^2}\sqrt{c_{i0}(\mathrm{TiO_2})c_\infty} = \frac{2\lambda}{\sqrt{c_{n0}(\mathrm{TiO_2})c_\infty}} \tag{4.16}$$

Normalizing the resistance with respect to the area (i.e., defining $Z^\perp \equiv R^\perp A$), the excess resistance can be obtained (*7*) as

$$\Delta Z^\perp = -\frac{2\lambda}{Fu}\frac{2}{c_\infty}\frac{\vartheta}{1+\vartheta} \tag{4.17}$$

where the parameter $\vartheta \equiv \frac{\left(\frac{c_0}{c_\infty}\right)^{1/2}-1}{\left(\frac{c_0}{c_\infty}\right)^{1/2}+1}$, u is mobility.

In the extreme case of pronounced depletion, it follows that

$$\Delta Z^\perp = \Delta Z_n^\perp = \sqrt{\frac{2\varepsilon RT}{c_{n0}c_\infty^2F^4u_n^2}} \tag{4.18}$$

where $\varepsilon = \varepsilon_r\varepsilon_0$. If the bias voltage η is applied, the concentration as a function of bias can be obtained as follows:

$$\begin{aligned}\sqrt{c_{n0}} &= \sqrt{c_\infty}\exp\frac{F(\phi_0-\phi_\infty)}{2RT}\\ &= \sqrt{c_\infty}\exp\frac{F(\widehat{\phi_0}-\phi_\infty)}{2RT}\exp\frac{F\eta}{2RT}\end{aligned} \tag{4.19}$$

where $\widehat{\phi_0}-\phi_\infty$ is the potential difference existing at equilibrium. Then the resistance can be obtained as

$$\begin{aligned}Z^\perp \simeq \Delta Z^\perp &= -\frac{2\lambda}{Fu_nc_\infty}\exp-\frac{F\left(\widehat{\phi_0}-\phi_\infty\right)}{2RT}\exp-\frac{F\eta}{2RT}\\ &= Z^\perp(\eta=0)\exp-\frac{F\eta}{2RT}\end{aligned} \tag{4.20}$$

$$\rightarrow \quad \frac{\partial \ln \frac{Z^{\perp}}{Z^{\perp}(\eta=0)}}{\partial -\frac{F\eta}{RT}} = \frac{1}{2}$$

which gives the square root dependence with regard to resistance response as a function of bias.

Regarding space charge capacitance, in terms of Gouy-Chapman profile, $\rho = -|z|Fc_{\infty}\sinh\frac{|z|F(\phi-\phi_{\infty})}{RT}$, which results in space charge capacitance $C^{\perp} \propto \cosh\frac{|z|F(\phi_0-\phi_{\infty})}{2RT}$. The space charge capacitance can be obtained as (*7*)

$$\frac{C^{\perp}}{a} = \frac{\varepsilon}{\lambda}\cosh\frac{|z|F(\phi_0-\phi_{\infty})}{2RT} = \frac{\varepsilon}{\lambda}\cosh\frac{|z|F(\eta-\eta^*)}{2RT} \tag{4.21}$$

where $\eta^* \equiv -(\widehat{\phi_0} - \phi_{\infty})$.

For large $(\phi_0 - \phi_{\infty})$ $(|F\eta| \gg RT)$, it leads to

$$\frac{C^{\perp}}{a} = \frac{\varepsilon}{2\lambda}\exp\mp\frac{|z|F(\phi_0-\phi_{\infty})}{2RT} = \frac{\varepsilon}{2\lambda}\exp\mp\frac{|z|F(\eta-\eta^*)}{2RT}$$

$$= \frac{\varepsilon}{2\lambda}\exp\mp\frac{|z|F\left(\widehat{\phi_0}-\phi_{\infty}\right)}{2RT}\exp\mp\frac{|z|F\eta}{2RT}$$

$$= \frac{C^{\perp}(\eta=0)}{a}\exp\mp\frac{|z|F\eta}{2RT} \tag{4.22}$$

$$\rightarrow \quad \frac{\partial \ln \frac{C^{\perp}}{C^{\perp}(\eta=0)}}{\partial \mp\frac{|z|F\eta}{RT}} = \frac{1}{2}$$

which also gives the square root dependence.

Let us come back to the discussion of the results. Bias sweep DC measurements (across the $Li_{\delta}TiO_2$/Ru interface, Fig. 4.12) corroborate the model presented in this work: Li is accumulated at the TiO_2 side, while electrons are depleted. On the Ru side, electrons are accumulated. For positive bias (positive at Ru side) the space charge splitting is decreased, leading to a decrease of impedance, for negative bias (positive at $Li_{\delta}TiO_2$ side) the impedance increased.

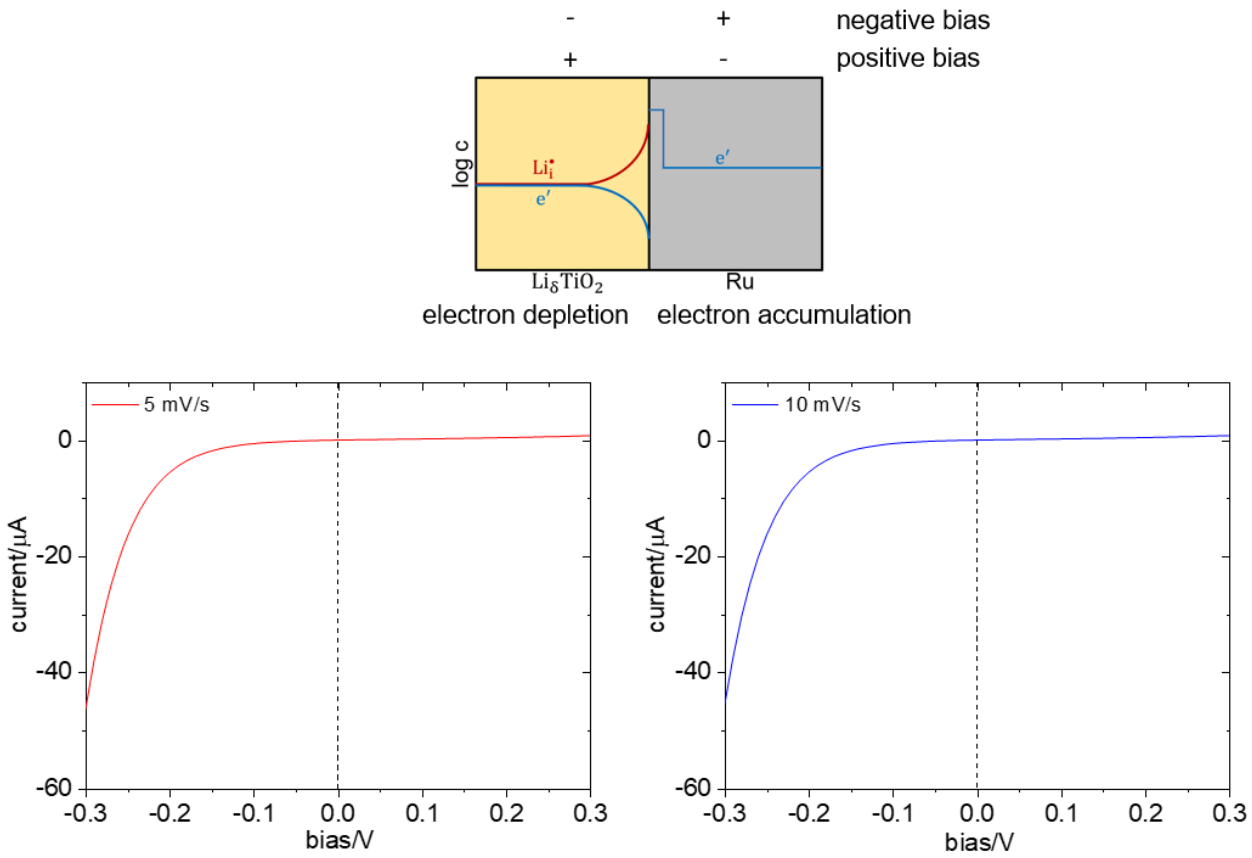

Fig. 4.12 Bias sweep measurements (across the $Li_\delta TiO_2$/Ru interface). For negative bias (positive at Ru side) the space charge splitting is decreased, for positive bias (positive at $Li_\delta TiO_2$ side) increased.

More conclusive results are obtained from bias dependent impedance measurements (Fig. 4.13), which indicate electronic depletion layers in TiO_2 according to the presented model. The resistance result in Fig. 4.13c follows accurately the expected square root dependence ($\frac{\partial \ln \frac{R^{\perp}}{R^{\perp}(\eta=0)}}{\partial -\frac{F\eta}{RT}} = \frac{1}{2}$) before saturation effects become perceptible. In fact, the whole bias range (five regimes) can be well explained based on the presented space charge model as shown in Fig. 4.14: (1) When a positive bias is applied at Ru side, the space charge splitting is decreased and the space charge potential decreases. The impedance change follows the square root dependence; (2) The initial equilibrium state is obtained for a zero bias (charge redistribution at interfaces forms equilibrium built-in potential); (3) When a negative bias is applied at the Ru side, the space charge splitting is increased and the space charge potential increases, leading to an increased impedance; (4) The resistance

does not change on varying bias due to saturation effects. (5) For large negative bias at the Ru side, the resistance begins to decrease because Li^+ ions could be forced to migrate to Ru side.

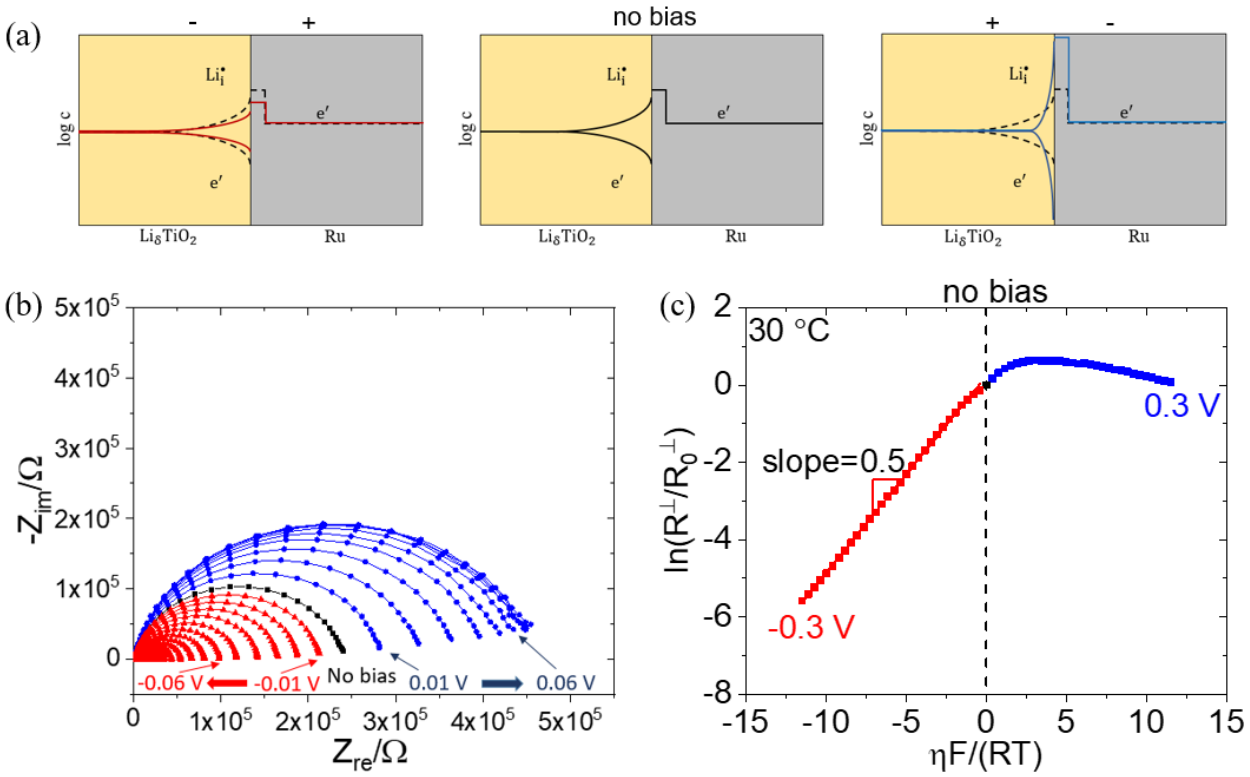

Fig. 4.13 Impedance measurement (perpendicular to the interface). (a) Charge carrier concentration profiles (across the $Li_\delta TiO_2$/Ru interface) as a function of bias. (b) Impedance spectrum. (c) Resistance as a function of bias. For negative bias (red) the space charge splitting is decreased, for positive bias (blue) increased. At positive bias saturation effects occur. The resistance decreases for large positive bias.

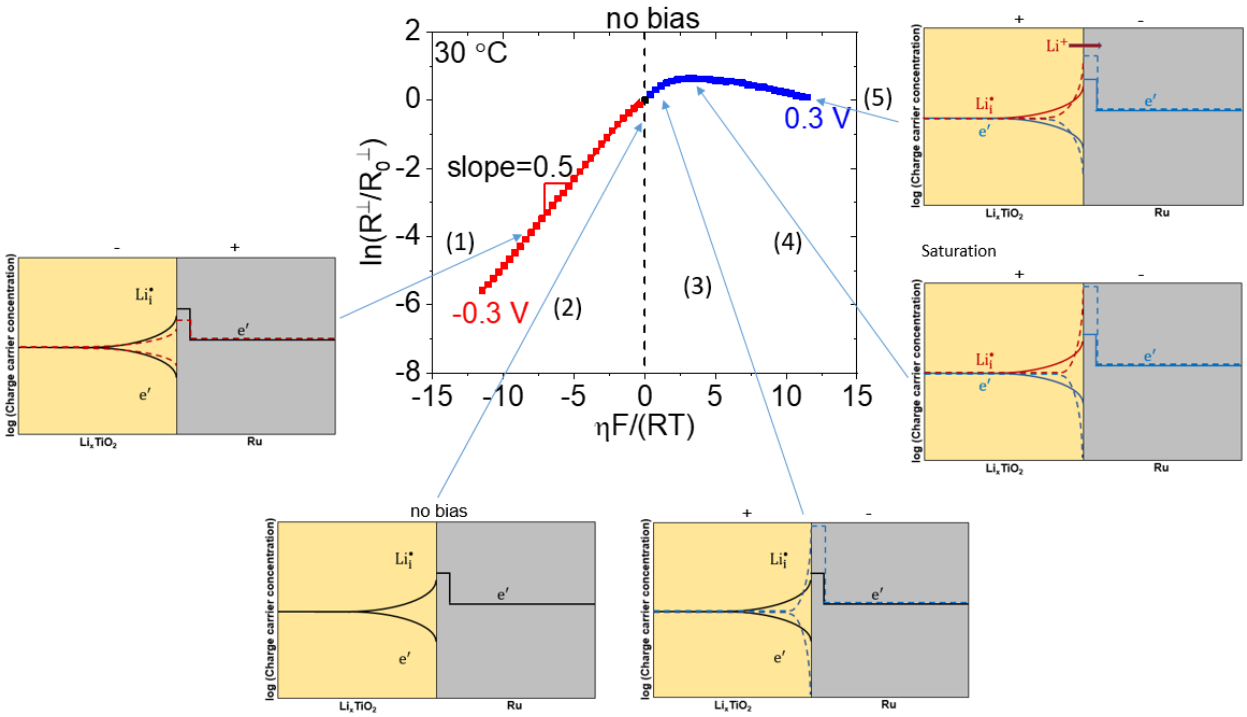

Fig. 4.14 Impedance measurement. Resistance response as a function of bias (five regimes).

The space charge capacitance can also be extracted from impedance measurements. As far as the evaluation of the interfacial electric capacitance (Fig. 4.15) is concerned, various interfaces ($Li_\delta TiO_2$/Ru and $Li_\delta TiO_2$/*N-ST* interfaces comprising a series of capacitors) might contribute. In fact, the smallest one is dominant and the response from one capacitor might be compensated by the others. As a result, the rather low bias dependence can be explained (the slope is 0.1, which is smaller than 0.5).

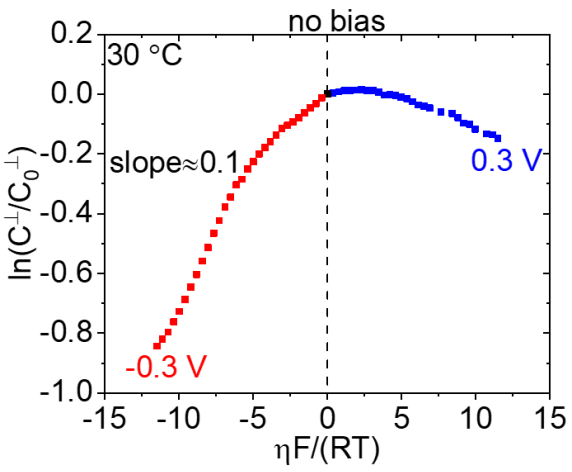

Fig. 4.15 Impedance measurement (perpendicular to the interface): Capacitance as a function of bias.

As a control experiment, the pure TiO_2 sample (Li-free, same thickness) on 0.5 wt% *N-ST* substrate has also been measured. The impedance is on the order of 100 Ω (Fig. 4.16), which is much lower than that when the pronounced space charge effects are present (lithiated sample ($Li_\delta TiO_2$)), which is another strong evidence that space charge effects play an important role in this investigated system. Again, the nice features of the impedance spectrum and good data quality indicate that the investigated model system is of high quality.

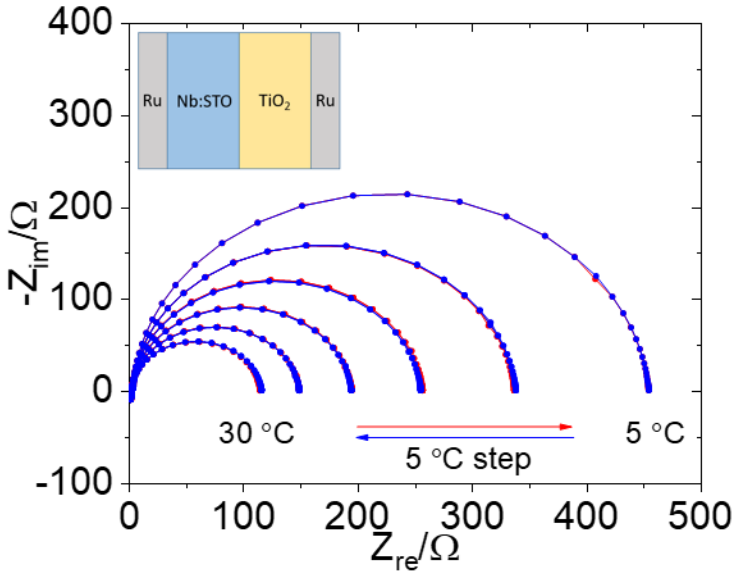

Fig. 4.16 Impedance measurement spectrum (perpendicular to the interface) of (Li-free) TiO_2 on 0.5 wt% *N-ST* substrate at different temperatures.

The space charge model proposed in this study is clearly corroborated by bias dependent transport measurements: Li is accumulated at TiO_2 side, while electrons are depleted. At the side of an electron-accepting substrate, electrons are accumulated. The results (especially the resistance data) are fully in accord with the theoretical prediction.

4.3.3 Electron and Li Distribution Obtained by STEM and EELS

The storage capacity of lithium in TiO_2 as a function of thickness for various electron-accepting substrates as well as different degrees of storage has been measured precisely, from which contributions from bulk and boundary storage were deconvoluted precisely. Supplemented by bias dependent impedance measurements, the proposed space charge model is evidenced. In order to determine electron and Li distribution using independent techniques in addition to electrochemical measurements, STEM and EELS measurements were performed. Atomic-resolution HAADF-STEM images of lithiated samples (Fig. 4.17) show that the investigated TiO_2 thin films keep good crystalline quality after electrochemical lithiation.

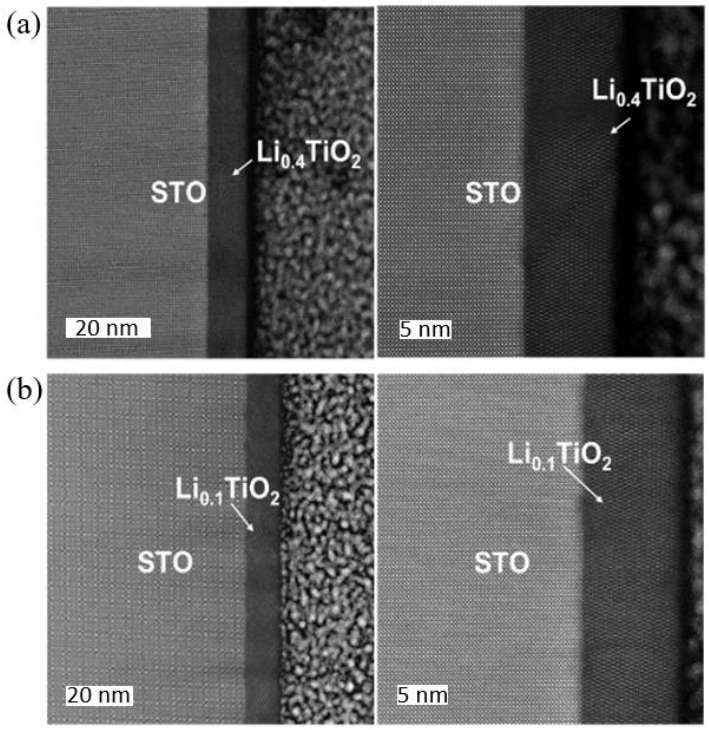

Fig. 4.17 Atomic-resolution HAADF-STEM images of lithiated samples across the interfaces: (a) $Li_{0.4}TiO_2$/*N-ST* and $Li_{0.1}TiO_2$/*N-ST*. TiO_2 thin films were deposited by MBE.

Moreover, atomic-resolution EELS maps of the constituent elements (Fig. 4.18a, 4.18e and 4.18i) clearly indicate that the interfaces between $Li_\delta TiO_2$ and *N-ST* under concern stay atomically sharp after lithiation. The detailed characteristics of the O-K and Ti-$L_{2,3}$ edges (Fig. 4.18b, 4.18f and 4.18j) appear to vary noticeably in different regions (from the $Li_\delta TiO_2$ bulk, across the interface, to the *N-ST* bulk). Especially near the interfaces, O-K edges change abruptly from the $Li_\delta TiO_2$ side to the *N-ST* side. At the interface of $Li_{0.4}TiO_2$/*N-ST*, the degree of splitting in the Ti-$L_{2,3}$ peaks is less prominent, accompanied by a downward shift of the Ti-L_3 peak (to lower energy), indicating variations in the electronic structure and bonding states. The analysis of energy-loss near-edge structure was performed based on the Ti-$L_{2,3}$ edges (Fig. 4.18d, 4.18h, and 4.18l) to quantitatively assess the evolution of the Ti valence state across the interfaces. In the case of low storage (Fig. 4.18h), the Ti valence in TiO_2 bulk is +3.9 and increases close to the boundary region owing to the electronic depletion. In the interface region of the *N-ST* side, the valence is lower than +4 near the interface (electronic accumulation) and increases towards +4 as it approaches the bulk. Regarding the case of large storage (Fig. 4.18l), the same trend is obtained, herein the Ti valence transitions from +3.6 to +4 when being from the bulk of $Li_\delta TiO_2$, across the interface, to the bulk of *N-ST*. The Ti valence variations (attributed to charge redistribution at the interfaces) exactly reflect the storage model: electrons accumulate at the *N-ST* side and deplete at the $Li_\delta TiO_2$ side, while Li accumulate at the $Li_\delta TiO_2$ side.

Furthermore, the fine structure EELS results explicitly demonstrate the Debye screening length in terms of the *N-ST* side, which is shown to be slightly larger than 1 nm (Fig. 4.18h and 4.18l) for both lithiated samples ($Li_{0.1}TiO_2$/*N-ST* and $Li_{0.4}TiO_2$/*N-ST*). It is worth noting that the calculated Debye screening length in 0.5 wt% *N-ST* is 1.1 nm, which is impressively consistent with the EELS results. In contrast, the interfacial effect on the TiO_2 side is very short-ranged owing to very high bulk concentration, which is less than the atomic spacing for both samples ($Li_{0.1}TiO_2$/*N-ST* and $Li_{0.4}TiO_2$/*N-ST*).

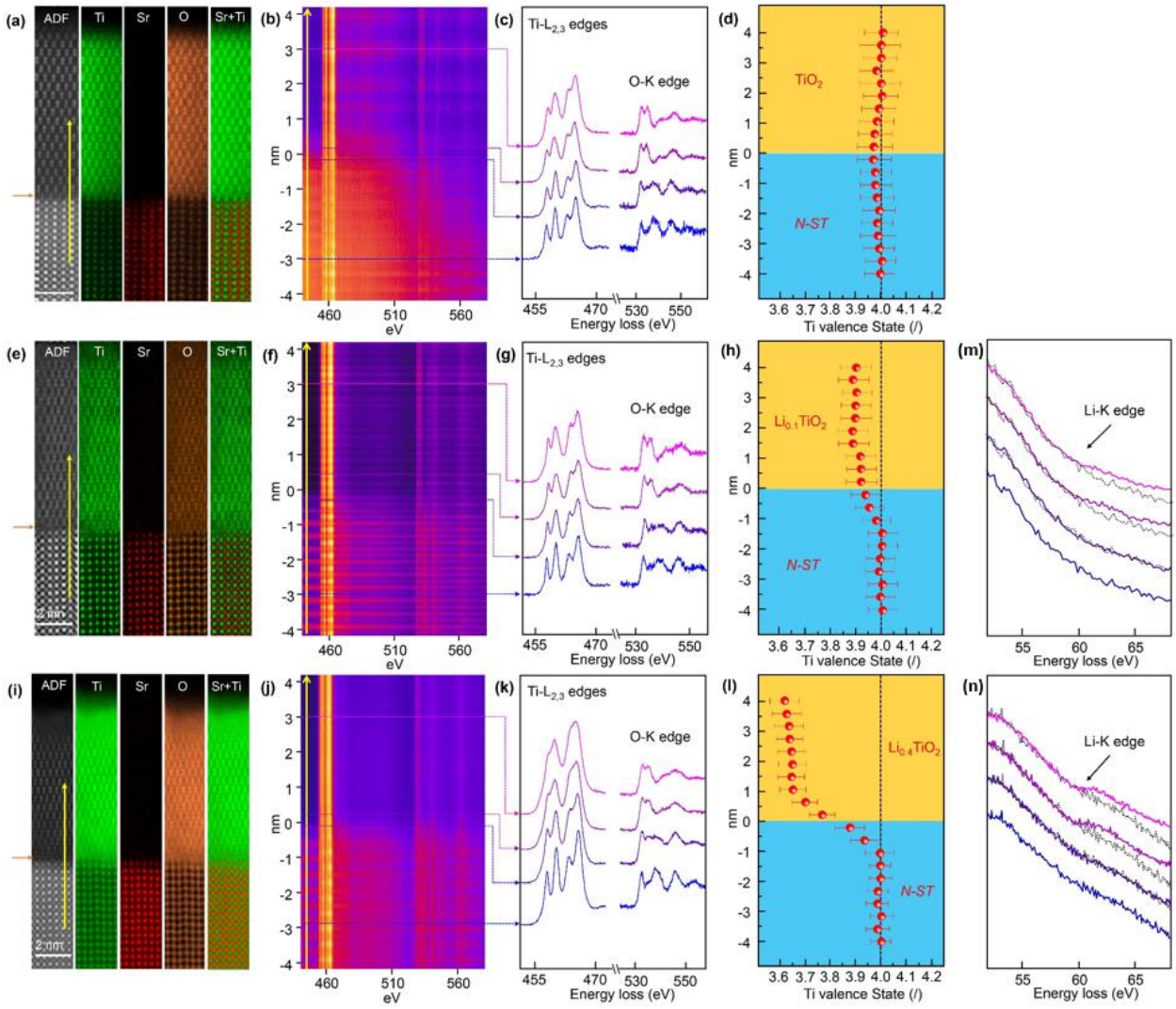

Fig. 4.18 STEM and EELS measurements. (a), (e), (i) STEM-EELS elemental maps across the interface of TiO_2/*N-ST*, $Li_{0.1}TiO_2$/*N-ST* and $Li_{0.4}TiO_2$/*N-ST*, respectively. (b), (f), (j) EELS line scan across the interface of TiO_2/*N-ST*, $Li_{0.1}TiO_2$/*N-ST* and $Li_{0.4}TiO_2$/*N-ST*, corresponding EELS spectra of Ti-$L_{2,3}$ and O-K edges (e), (g), (k) from four different regions (substrate, substrate-side close to the interface, TiO_2-side close to the interface, TiO_2), and fine structure analysis of Ti-$L_{2,3}$ edges (d), (h), (l) across the interface. (m), (n) EELS spectra of Li-K edge at the *N-ST* side and lithiated TiO_2 side. The doping content (Nb) of *ST* substrate is 0.5 wt%. TiO_2 thin films were deposited by MBE. These experiments have been performed by Hongguang Wang in the "Stuttgart Center for Electron Microscopy (StEM)". See also Refs. (*114, 117*).

The abovementioned results clearly indicate the electron distribution, based on which Li distribution is reflected indirectly. In fact, the intercalated Li has also been identified in the ABF image of lithiated sample $Li_\delta TiO_2$ (as indicated by green arrows in Fig. 4.19b) compared to pure

TiO_2 (Fig. 4.19a, anatase structure). ABF results of *N-ST* do not show any change after lithiation, indicating the absence of Li (see Fig. 4.20). More impressively, EELS spectra of Li-K edge for lithiated samples unambiguously demonstrate the presence of Li signal in TiO_2, but not in *N-ST* (Fig. 4.18m and 4.18n), which is consistent with ABF results and in agreement with the space charge model (as shown in Fig. 4.21 (bottom)). Owing to the interference of Ti signal, a more quantitative evaluation is not possible. The signal intensity of Li-K edge at the interface region seems stronger than that in the bulk, which might evidence that there exists more Li at the interface (Li accumulation).

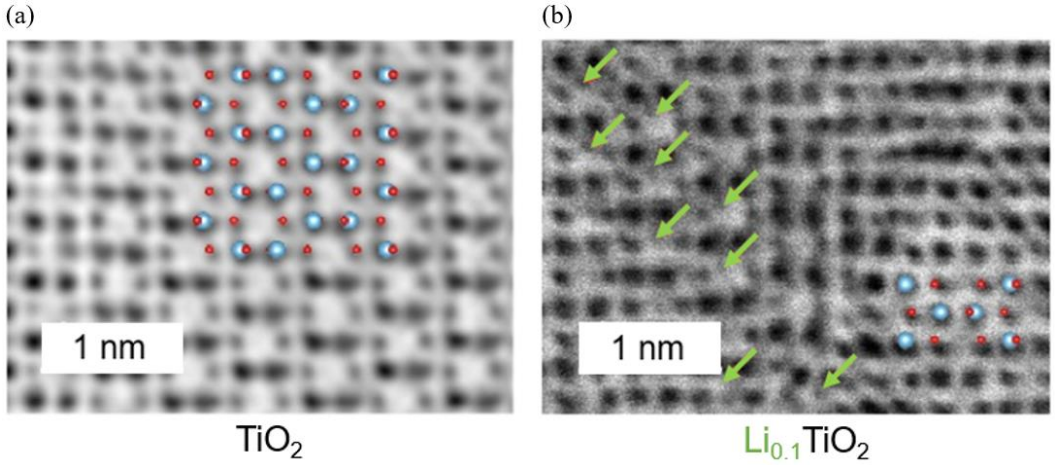

Fig. 4.19 ABF images of TiO_2 (a) and $Li_{0.1}TiO_2$ (b). TiO_2 thin films were deposited by MBE. These experiments have been performed by Hongguang Wang in the "Stuttgart Center for Electron Microscopy (StEM)". See also Refs. (*114*, *117*). (blue spheres: Ti, red spheres: O)

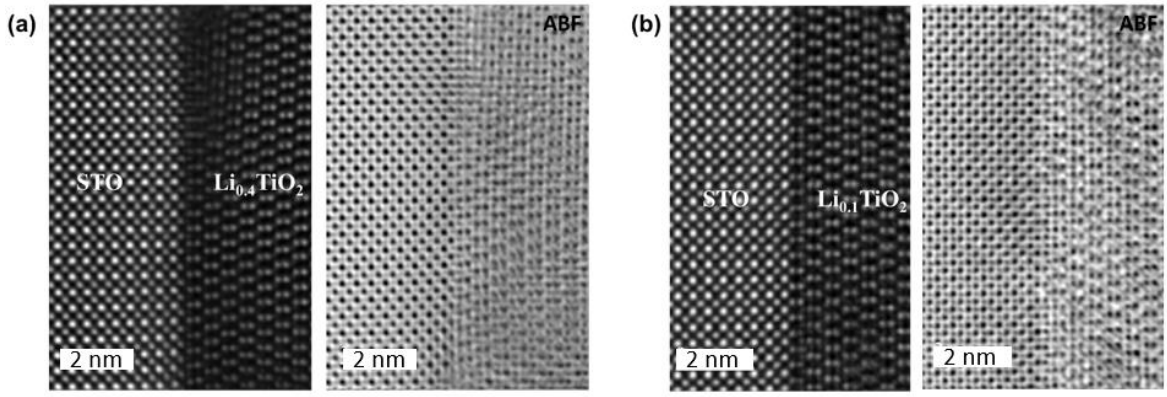

Fig. 4.20 Simultaneously-acquired HAADF and ABF images for lithiated samples $Li_{0.4}TiO_2$ (a) and $Li_{0.1}TiO_2$ (b) at the interfacial region (across the $Li_\delta TiO_2$/*N-ST* interfaces). TiO_2 thin films were deposited by MBE. These experiments have been performed by Hongguang Wang in the "Stuttgart Center for Electron Microscopy (StEM)". See also Refs. (*114*, *117*).

The STEM and EELS results clearly corroborate the space charge model in this study. Combining the electrochemical storage and transport results, bulk and boundary contributions are precisely decoupled, leading to a generalized thermodynamic picture (unification of bulk and interfacial storage).

4.3.4 Generalized Picture: Unification of Intercalation Electrode and Supercapacitor Storage

Contributions from bulk and boundary storage were deconvoluted precisely based on the aforementioned electrochemistry and electron microscopy results. Such experimental investigation allows for deriving the entire profile, which can be quantitatively given as a function of the positional coordinate (x) with temperature, pressure, doping content (C) and Li-activity (cell voltage) as control parameters. A common generalized thermodynamic model (see Fig. 4.21) is obtained by unifying the bulk and interfacial defect chemistry into a generalized thermodynamic framework.

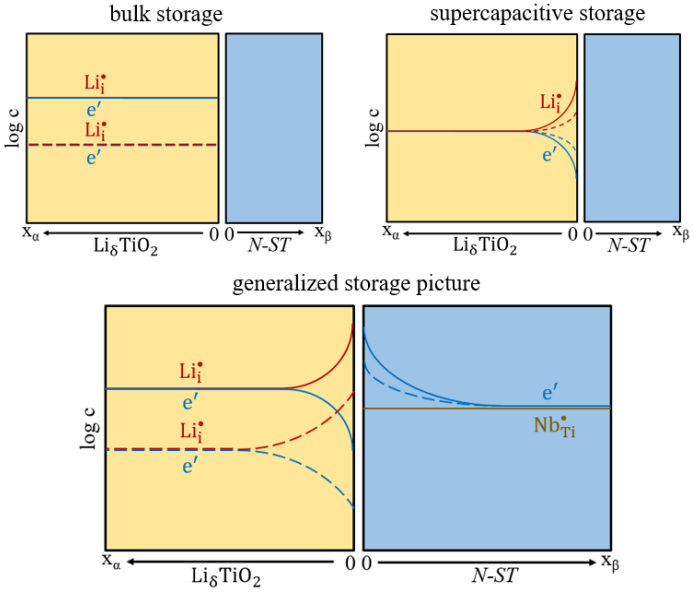

Fig. 4.21 The charge carrier concentration profiles for bulk storage, supercapacitive storage and generalized storage for TiO_2, here contacted with *N-ST* highlight the basic message of the contribution. For the sake of illustration, different scales are used for x_α and x_β. Owing to the much smaller Debye length in $Li_\delta TiO_2$, the space charge zone (not more than one unit cell even for the smaller $\delta \approx 0.1$) is much narrower than for *N-ST*.

For the sake of clarity, Li-interstitials (i) and excess electrons (n) are referred to, and dilute conditions are considered.

Then the equilibrium space charge profile can be written as

$$\frac{c_i(x,T,C,a_{\mathrm{Li}})}{c_{i\infty}(T,C,a_{\mathrm{Li}})} = \left[\frac{1+\vartheta_i(T,C,a_{\mathrm{Li}})exp-\frac{x}{\lambda(T,C,a_{\mathrm{Li}})}}{1-\vartheta_i(T,C,a_{\mathrm{Li}})exp-\frac{x}{\lambda(T,C,a_{\mathrm{Li}})}}\right]^2$$

$$= \left[\frac{c_n(x,T,C,a_{\mathrm{Li}})}{c_{n\infty}(T,C,a_{\mathrm{Li}})}\right]^{-1} \tag{4.23}$$

C is the effective dopant concentration (*7*).

The parameter ϑ measures the impact of the neighbouring phase (substrate (S)) and is correlated with $c(x=0) \equiv c_0$ as

$$\vartheta_i \equiv \frac{\left(\frac{c_{i0}}{c_{i\infty}}\right)^{1/2}-1}{\left(\frac{c_{i0}}{c_{i\infty}}\right)^{1/2}+1} \tag{4.24}$$

The two parameters c_∞ and c_0 can be obtained as follows:

If i and n are the defects of relevance

$$c_{i\infty} \cdot c_{n\infty} = K \cdot a_{\mathrm{Li}} \tag{4.25}$$

whereby K is the mass action constant of Li incorporation into the bulk

$$\mathrm{Li} + V_i(\mathrm{TiO_2}) \rightleftharpoons \mathrm{Li}_i^{\cdot}(\mathrm{TiO_2}) + e'(\mathrm{TiO_2}) \tag{4.26}$$

It is given by $\exp -\frac{\mu_i^0(\mathrm{TiO_2})+\mu_n^0(\mathrm{TiO_2})}{RT}$, where μ^0 is the standard chemical potential.

Owing to electroneutrality

$$c_{i\infty} = c_{n\infty} = \sqrt{K \cdot a_{\mathrm{Li}}} \tag{4.27}$$

If association is ignored, the same results for the total Li-concentration in the bulk, which is proportional to q. Then $q \propto K^{1/2} a_{\mathrm{Li}}^{1/2}$ is obtained.

The boundary concentration c_0 can be obtained as follows:

Here heterogeneous Li-incorporation is considered, and it is formulated as

$$\mathrm{Li} + V_i(\mathrm{TiO_2}) \rightleftharpoons \mathrm{Li}_i^{\cdot}(\mathrm{TiO_2}) + e'(\mathrm{S}) \tag{4.28}$$

In equilibrium

$$c_{i0}(\mathrm{TiO_2}) \cdot c_{n0}(\mathrm{S}) = K_{het} \cdot a_{\mathrm{Li}} \cdot æ \tag{4.29}$$

where æ $(= \exp - F\frac{\phi(\mathrm{TiO_2},0)+\phi(\mathrm{S},0)}{RT})$ stands for the electrical field effect between the two outermost layers in TiO_2 and substrate, which is determined by the electrical potential drop between these outermost layers. The heterogeneous mass action constant K_{het} is given by $\exp - \frac{\mu_i^0(\mathrm{TiO_2})+\mu_n^0(\mathrm{S})}{RT}$. Again, association is ignored. (*6, 40*)

As dilute effects are considered, æ is considered as a constant. Instead of local electroneutrality, only global electroneutrality is valid, leading (for the same dielectric constant) to $c_{i0} \simeq c_{n0}$ as $Q_i \propto \sqrt{c_{i0}}$ and $Q_n \propto \sqrt{c_{n0}}$ for Gouy-Chapman profiles on both sides. The same result is also obtained if both phases exhibit single-layer storage, i.e., $Q_i \propto c_{i0}$, $Q_n \propto c_{n0}$ (For other cases, cf. Ref (*40*)). If e.g. Gouy-Chapman profiles are relevant for both sides, $Q_{int} \propto \sqrt{c_{i0}}$ while $c_{i0} = c_{n0} = \sqrt{K_{het} a_{\mathrm{Li}} æ}$ and hence $Q_{int} \propto K_{het}^{1/4} a_{\mathrm{Li}}^{1/4}$, while $q \propto K^{1/2} a_{\mathrm{Li}}^{1/2}$ is obtained for the bulk.

Therefore, different power laws for the stored charge (Q_{int} *or* q) as a function of the lithium activity (power: *N*) is expected, where $N \leq 1/4$ for boundary and $N \geq 1/2$ for bulk. Hence the ratio of boundary and bulk storage depends on the degree of storage. For dilute conditions, this ratio then follows a power law with a power smaller than -1/4.

For higher concentrations, activity coefficients for ions and electrons are to be considered due to long-range interaction and saturation effects as well as association effects. Furthermore, the variation of æ becomes important.

For details and extensions, see Refs. (*6, 7, 28, 40, 118*).

Since the mass action constants are determined by the standard reaction free energies, ultimately the standard chemical potentials of e' in TiO_2 and in substrate as well as the standard potential of the Li^+-defects in TiO_2 are the only materials constants needed, and the entire profile follows from them given the thermodynamic control parameters.

In this thesis, TiO_2 and Nb_2O_5 thin films, which have well-defined geometry and are of high quality, have been used as the model system to study the fundamental issues related to charge storage and transport in solids. In addition to the main text of the thesis, two other fundamentally important investigations are worth mentioning here. First, bias-dependent resistance and capacitance measurements across the Li_xTiO_2/electronic conductor interface have also been operated at "frozen-in" temperature. The classic Mott-Schottky profiles are not only unrealistic in most cases, they are also hard to establish. The frozen-equilibrium approach provides a way to improve beyond the Mott-Schottky model. Second, cyclic voltammetry (CV) measurements under wide range of sweep rates using TiO_2 and Nb_2O_5 thin films of different thicknesses were also performed, which allows for testing and correcting the cyclic voltammetry method for solid state. The classical analyses are based on liquid-state electrochemistry. For solid state, however, the analysis must be modified to account for fundamental differences between solid-state and liquid-state storage. All these fundamental studies are very relevant to energy-related application. Even though they are not belonging to the focus of the thesis, they are fundamentally interesting and important. For the details, one should refer to the upcoming publications (*119*, *120*).

5
Conclusions

The present study comprehensively investigates the general view of storage in a mixed conductor (general materials case). This leads to a unification of battery intercalation electrode and supercapacitor concepts, which are unnecessarily considered as two separate phenomena. Following and extending the quantitative concept of job-sharing storage, a generalized picture that includes bulk and space charge storage (intercalation electrode and supercapacitor storage) is developed.

In the first part of the thesis, the history and developments of space charge theory are reviewed, from liquid electrochemistry to solid-state ionics. A variety of problems and shortcomings with the classic continuous Gouy–Chapman solution that occur for pronounced space charge potentials are discussed. Besides the inherent problems of internal consistency (identifying the mean potential appearing in Poisson's equation (potential not changed by a spy-particle) with the potential of mean force appearing in the Boltzmann expression (potential referring to the distribution that self-consistently includes the particle)), it is essentially the extremely steep profile close to the interface which makes this continuum approach questionable when the space charge effects are pronounced. In addition, involving crystallographic details and non-idealities close to the interface in realistic solids into the classic continuous solution is unfeasible. Therefore, in this context, it is extended in terms of discrete modeling of space charge zones in solids, which reveals details on the difference between space charge capacitance and measured capacitance. This difference is not completely removed by a Helmholtz correction, in more precise terms also an inherent small shift of the centroid of charge has to be considered. More importantly, in the discretized zone (first layers), knowledge from atomistic modelling or experiments about non-idealities (such as energetic variations owing to structural or elastic effects, variations in the dielectric permittivity or saturation effects) can be included in a straightforward way. MgO and

$SrTiO_3$ examples clearly show how discretization combining with the continuum description is utilized to handle non-idealities in realistic solid-state system by inserting the calculated data (e.g., from DFT). Hence, a more realistic space charge picture is obtained. Simultaneously, the discretization is relevant for the electrochemical storage systems under concern in the core part of this thesis (TiO_2), where the significance of single-layer storage is stressed during the analysis. In this way a more precise definition and demarcation of electrode and double layer capacity is achieved.

The core part of the thesis investigates the unification of bulk storage and interfacial storage by carefully investigating the storage of lithium in titania films as a function of thickness. Complemented by bias dependent impedance measurements, STEM and EELS measurements, the generalized picture including bulk and interfacial storage, in terms of charge carrier concentrations as function of spatial coordinate with cell voltage and substrate conditions as parameters, is obtained.

First, the investigated model TiO_2 thin films on various electron-accepting substrates such as Nb doped $SrTiO_3$ (*N-ST*), undoped $SrTiO_3$ (*ST*), Fe doped $SrTiO_3$ (*F-ST*), Ruthenium have been deposited utilizing three methods: atomic layer deposition (ALD), pulsed laser deposition (PLD) and molecular beam epitaxy (MBE). Various techniques including x-ray diffraction (XRD), transmission electron microscopy (TEM), electron energy loss spectroscopy (EELS), atomic force microscopy (AFM) and X-ray photoelectron spectroscopy (XPS) have been applied for the characterization. One of the key parameters in this context is the film thickness, which has been determined accurately using x-ray reflectivity (XRR), TEM, stylus profilometry. All the three techniques show consistent results. Well-prepared TiO_2 films with sharp interface and precise thickness control are obtained for the electrochemical experiments and electron microscope measurements.

Second, the battery storage capacity measurements of TiO_2 thin films as a function of thickness are performed, with Li-activity (cell voltage – different degrees of storage) as well as the nature of substrates (electronic situation in the substrates) as control parameters. The precise thickness dependent storage capacity measurements allow for deconvoluting bulk (the slope) and interfacial (the intercept) storage with high accuracy. In terms of different degrees of storage, both bulk and boundary values depend differently on the Li activity (degree of storage). Consequently, the ratio

of the two linked storage capacities varies with Li content. This ratio was shown to be significantly beyond the dilute limit. The expected crystallographic and electronic saturation effects lead to a flattening of the $Q(a_{Li})$ curve. As extrapolated from the dilute situation, saturation will set in earlier for the boundaries, leading to a reversed tendency for the ratio. The effect of the electronic situation in the substrate, which affects the Li-uptake in TiO_2, is corroborated by the experimental results, too. From more highly donor doped *ST* to less doped, from donor doped to undoped, from undoped to acceptor doped (*F-ST*), the storage capacity increases owing to the decrease of electron concentration already present in the substrate (increasing the capability for accepting excess electrons). Highest interfacial storage capacities are obtained by using Ru substrate, because Ru has a more favorable heterogeneous mass action constant, essentially due to the lower energy for accepting excess electrons. This thermodynamic prediction is in accord with the experimental results.

The proposed space charge model is clearly corroborated by bias dependence transport measurements, where the bias dependent resistance of the dominating interface ($Li_\delta TiO_2/Ru$) exactly follows the theoretical square root dependence. The interfacial capacitance follows a similar trend, however, with a lower bias dependence, due to possible contributions from various interfaces. In combination with aberration-corrected scanning transmission electron microscopy (STEM) and electron energy loss spectroscopy (EELS) measurements, accurate spatial information on electron and Li distribution is obtained, which reproduces the space charge model: Li is accumulated at the TiO_2 side, while electrons are depleted. At the side of an electron-accepting substrate, electrons are accumulated.

As a result, not only bulk and boundary storage contributions are precisely decoupled, but they can be traced back to a common generalized thermodynamic conception, leading to a unification of battery intercalation electrode and supercapacitor concepts. In fact, by taking account of the (free) energies of the electronic carriers in TiO_2 and the substrate as well as the formation (free) energy of the Li-ions in TiO_2 (three bulk materials parameters) as control parameters, the entire profile including interfacial and bulk effects can be derived. This treatment that unifies bulk intercalation and supercapacitive storage mechanisms provides a way of better understanding and mitigating the energy and power density conflict of storage devices, which becomes particularly

important for nanoionic systems. It is hoped that this may form the basis of building a bridge between the two important fields.

Appendix I

Poisson-Boltzmann equation Eq. (2.2) can be obtained by combining Poisson's equation and Boltzmann distribution

$$\nabla^2\phi = -\frac{F}{\varepsilon\varepsilon_0}\sum_m z_m c_{m\infty} e^{\frac{-Fz_m(\phi-\phi_\infty)}{RT}} \tag{A. I. 1}$$

Abbreviating $\frac{d\phi}{dx} = f$, then $\frac{d^2\phi}{dx^2}$ can be rewritten as $\frac{df}{dx} = \frac{df}{d\phi}\frac{d\phi}{dx} = \frac{df}{d\phi}f$ and equation (A.I.1) can be rewritten as

$$\int f df = -\frac{F}{\varepsilon\varepsilon_0}\int \sum_m Z_m c_{m\infty} exp\left(\frac{-Fz_m(\phi-\phi_\infty)}{RT}\right) d\phi \tag{A. I. 2}$$

Considering the boundary condition $\phi(x=\infty) - \phi_\infty = 0 = f(x=\infty)$, it yields

$$-\frac{d\phi}{dx} = -\sqrt{\frac{2RT}{\varepsilon\varepsilon_0}\sum_m \left(c_{m\infty} exp\left(\frac{-Fz_m(\phi-\phi_\infty)}{RT}\right) - c_{m\infty}\right)} \tag{A. I. 3}$$

For the case of monovalent defect, the term in the bracket of Eq. (A. I. 3) can be rewritten as

$$\begin{aligned} &c_{m\infty}\left(exp\left(\frac{-F(\phi-\phi_\infty)}{RT}\right) - 2 + exp\left(\frac{F(\phi-\phi_\infty)}{RT}\right)\right) \\ &= \left(\sqrt{c_{m\infty}}\right)^2\left(exp\left(\frac{-F(\phi-\phi_\infty)}{2RT}\right) - exp\left(\frac{F(\phi-\phi_\infty)}{2RT}\right)\right)^2 \end{aligned} \tag{A. I. 4}$$

and then

$$-\frac{d\phi}{dx} = -\sqrt{\frac{2RT}{\varepsilon\varepsilon_0}}\left(\sqrt{c_i(x)} - \sqrt{c_v(x)}\right) \tag{A. I. 5}$$

The total stored charge thus can be obtained, according to Poisson equation ($\rho = -\varepsilon\varepsilon_0\frac{d^2\phi}{dx^2}$) and the boundary condition $\frac{d\phi_\infty}{dx} = 0$, by integrating the charge density from $x = 0$ to $x = \infty$

$$Q = \int_0^\infty \rho(x)dx = \sqrt{2\varepsilon\varepsilon_0 RT}\left(\sqrt{c_i(0)} - \sqrt{c_v(0)}\right) \tag{A. I. 6}$$

Appendix II

Regarding conductance and resistance, in a measurement parallel to the interface it is the conductance $Y^{\parallel}$ (conductance per area) that is of significance. Assuming a negative excess charge on the metal side, then singly-charged anion vacancies as the positive charged defects are enriched and the negative carriers, singly-charged cation vacancies, are depleted. When measuring the excess conductance parallel to the interface, the focus of the interest is a situation where the excess conductance stems from the first. If the effects are significant, then $Y^{\parallel}$ can be approximated by the total excess charge, and in this case, there is no distinction between the continuum and the discrete description, as long as the continuous profile is adequately chosen. As demonstrated in the text, a continuous profile that starts exactly at the first layer (i.e. $x = x' = 0$) results in a lower total charge. In a measurement perpendicular to the interface, the most interesting case is a situation, where the depleted carrier possesses the highest mobility, such that it determines the normalized resistance $Z^{\perp}$ ($1/Y^{\perp}$). Due to the fact that

$$\frac{c_+}{c_\infty} = \frac{c_\infty}{c_-} = e^{-\psi} \tag{A. II. 1}$$

and hence $Y^{\parallel} \propto \int c_+ dx = \int \frac{1}{c_-} dx \propto Z^{\perp}$, The same conclusion can be drawn for $Z^{\perp}$ (resistance times area). In Eq. (A. II. 1), $\frac{F\phi}{RT}$ has been abbreviated by ψ to simplify the notation. Once $x - x' = \frac{a}{2}$, differences between conductances (resistances) for the two models occur only if the respective counter carrier is of significance (i.e. rather small $|\psi|$).

Appendix III

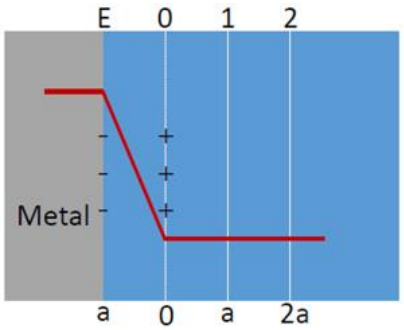

$$\frac{\mathcal{L}}{a} = \frac{0 \times 3}{3} = 0$$

$$\frac{1}{C_{tot}} = \frac{\partial(\phi_E - \phi_0)}{\partial Q} = \frac{a}{\varepsilon}$$

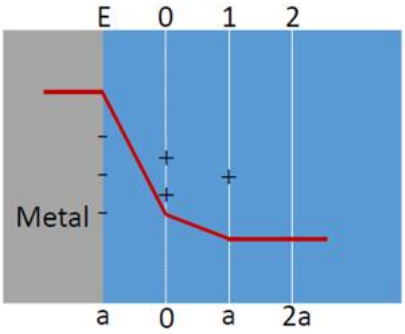

$$\frac{\mathcal{L}}{a} = \frac{0 \times 2 + 1 \times 1}{3} = \frac{1}{3}$$

$$\frac{1}{C_{tot}} = \frac{\partial(\phi_E - \phi_0)}{\partial Q} + \frac{\partial(\phi_0 - \phi_1)}{\partial Q} = \frac{a}{\varepsilon} + \frac{a}{3\varepsilon}$$

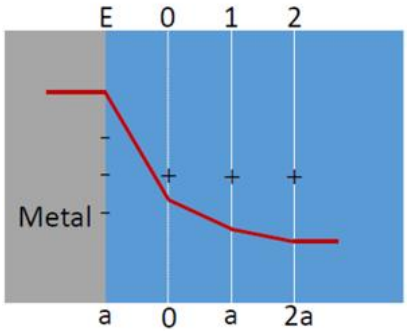

$$\frac{\mathcal{L}}{a} = \frac{0 \times 1 + 1 \times 1 + 2 \times 1}{3} = 1$$

$$\frac{1}{C_{tot}} = \frac{\partial(\phi_E - \phi_0)}{\partial Q} + \frac{\partial(\phi_0 - \phi_1)}{\partial Q} + \frac{\partial(\phi_1 - \phi_2)}{\partial Q} = \frac{a}{\varepsilon} + \frac{a}{\varepsilon}$$

Fig. A III. 1 A few simple examples for centroid calculations.

Appendix IV

To compare the discrete with the continuum model, it is very illustrative to first use the well-known exponential limit of the Poisson-Boltzmann equation that follows for $|\psi| \ll 1$. This approach is useful for the following reasons:

(i) The exponential solution is simple to test.

(ii) It does not have any consistency issues since it corresponds to a linear relation between ψ and ρ which fulfills the superposition principle of electrostatics.

(iii) Even for large effects, one can handle the first layers discretely such that the remaining part is, to be a good approximation, exponential.

Regarding the Debye-Hückel approximation, for small $|\psi|$ it holds that

$$\frac{c_+}{c_\infty} = e^{-\psi} \approx 1 - \psi \qquad \text{(A. IV. 1)}$$

due to the constancy of the electrochemical potential $\tilde{\mu}_+$ (equilibrium) and of the standard potential μ_+^0 (structure uniformity).

Coupling with Poisson's equation demands

$$\nabla^2\psi = \frac{1}{\lambda^2}\psi \qquad \text{(A. IV. 2)}$$

with $\lambda = \sqrt{\frac{RT\varepsilon\varepsilon_0}{2F^2 c_\infty}}$ giving rise to the indicated solution $\psi = \psi_0 e^{-\frac{x}{\lambda}}$.

All the individual concentrations and concentration changes (the same holds for the charge density) are proportional to ψ and exhibit exponential variation with position:

$$\frac{c_-}{c_\infty} = e^{\psi} \approx 1 + \psi \approx \frac{1}{1 - \psi} \qquad \text{(A. IV. 3)}$$

$$\frac{c_- - c_\infty}{c_\infty} = \psi = -\frac{c_+ - c_\infty}{c_\infty} \qquad \text{(A. IV. 4)}$$

$$\frac{c_- - c_\infty}{c_{-0} - c_\infty} = \frac{\psi}{\psi_0} = -\frac{c_+ - c_\infty}{c_{+0} - c_\infty} \qquad \text{(A. IV. 5)}$$

$$\frac{q}{aF} = c_+ - c_- = -2c_\infty \psi \qquad \text{(A. IV. 6)}$$

For the discrete model, as the charges at $x' = 0, a, 2a, \ldots$ can be given as $q_i = q_0 e^{-\frac{ia}{\lambda}}$, the total charge follows as geometrical series, which due to $e^{-\frac{a}{\lambda}} < 1$, converges, hence

$$\mathrm{Q} = \sum_{i=0}^{\infty} q_i = q_0 \sum_{i=0}^{\infty} e^{-\frac{ia}{\lambda}} = q_0 \frac{1}{1 - e^{-\frac{a}{\lambda}}}$$

$$\simeq q_0 \frac{1}{1 - \left(1 - \frac{a}{\lambda}\right)} \simeq \frac{q_0 \lambda}{a} \left(1 + \frac{a}{2\lambda}\right) \qquad \text{(A. IV. 7)}$$

The solution for the total charge obviously is larger by $\frac{q_0}{2}$. (The only profile that hits the discrete points and yields the same total charge is a sectionally linear profile.) The shift by $\frac{a}{2\lambda}$ when compared to 1 disappears in a rougher approximation, resulting in the same result as the continuous solution.

To compare the continuous and discrete distributions for the same Q, two possible options are available: introducing a different λ ($\rightarrow \lambda(1 + \frac{a}{2\lambda})$) or utilizing a different q_0.

The first option is inadequate as the screening length λ is defined by bulk parameters ($\sqrt{\frac{\varepsilon\varepsilon_0 RT}{2F^2 c_\infty}}$).

The second way provides a very insightful possibility. The above continuous profile with q_0 at $x' = 0$ is adopted but the profile is prolonged towards the interface up to $x' = -\frac{a}{2}$ (i.e. $x = 0$). As can be straightforwardly seen, this introduces an additional contribution to the total charge which is given by

$$\Delta\mathrm{Q} = \frac{q_0}{a} \int_{-\frac{a}{2}}^{0} e^{-\frac{x'}{\lambda}} \, \mathrm{d}x' = \frac{q_0 \lambda}{a} \left(e^{\frac{a}{2\lambda}} - 1\right)$$

which indeed simplifies for $a \ll 2\lambda$ to $\frac{q_0}{2}$, the missing contribution.

Obviously starting at $x' = -\frac{a}{2}$ (defining $x = 0$) yields a profile that hits all discrete values properly and results in a corrected total charge. If $\lambda \to a$ or a large space charge potential is established, $q(x = 0)$ is still larger than $q(x' = 0)$. As the discrete charge is systematically smeared out, the continuous profile $q(x)$ adopts the discrete values q_i in the interval $x' \pm \frac{a}{2}$ provided the potential does not become too high.

The centroids for the low field approximation are calculated next. In the continuum model, $\mathcal{L}_c = \lambda$ is obtained straightforwardly, while this value is obtained for the discrete model only approximately. Here we made use of the fact that not only the geometrical series $\sum_{i=0}^{\infty} q_i$ converges (as $e^{-\frac{a}{\lambda}} < 1$) (Eq. (A. IV. 7)) but also the geometrical series $\sum_{i=0}^{\infty} i q_i$:

$$\sum_{i=0}^{\infty} i q_i = \frac{q_0 e^{-\frac{a}{\lambda}}}{(1 - e^{-\frac{a}{\lambda}})^2} \qquad \text{(A. IV. 8)}$$

Hence, with $x_i' \equiv ia$,

$$\frac{\mathcal{L}_d}{a} = \frac{1}{a}\frac{\sum_i x_i' q_i}{\sum_i q_i} = \frac{e^{-\frac{a}{\lambda}}}{1 - e^{-\frac{a}{\lambda}}} = \frac{1}{e^{\frac{a}{\lambda}} - 1} \qquad \text{(A. IV. 9)}$$

is obtained, which can be approximated by $\mathcal{L}_d = \lambda\left(1 - \frac{a}{2\lambda}\right) \equiv \mathcal{L}_d^{(1)}$, and even further to $\mathcal{L}_d^{(0)} \equiv \lambda$.

$\mathcal{L}_d^{(0)}$ is identical to $\mathcal{L}_c$, but for the precise centroid it holds that $\mathcal{L}_d \approx \mathcal{L}_d^{(1)} \approx \lambda - \frac{a}{2}$. The numerical check corroborates this deviation, and $\mathcal{L}_d^{(1)}$ is indeed a much better approximation to $\mathcal{L}_d$.

Using Eq. (2.10) with $\frac{1}{C_{\mathrm{SC}}} = \frac{\mathcal{L}_d}{\varepsilon}$, the rather precise result can be obtained as

$$\frac{1}{C} = \frac{b}{\varepsilon} + \frac{\lambda - \frac{a}{2}}{\varepsilon} \qquad \text{(A. IV. 10)}$$

This result is also numerically checked and investigated for various $\frac{b}{a}$ values (Table IV. 1(a), (b)). Furthermore, according to the numerical calculations, the deviation by $\frac{a}{2}$ is perceptible even though the validity of the exponential solution demands λ to exceed a.

Table IV. 1 (a) $\frac{\lambda}{a}$ = e

$\frac{b}{a}$	$\frac{\varepsilon}{b}\frac{1}{C}$	$\frac{\varepsilon}{b}\frac{1}{C}-\frac{\lambda}{b}$	$\frac{b-a/2}{b}$
2	2.1244	0.7653	0.7500
3	1.7496	0.8435	0.8333
4	1.5622	0.8826	0.8750
8	1.2811	0.9413	0.9375
16	1.1406	0.9707	0.9688

Table IV. 1 (b) $\frac{\lambda}{a}$ = 5e

$\frac{b}{a}$	$\frac{\varepsilon}{b}\frac{1}{C}$	$\frac{\varepsilon}{b}\frac{1}{C}-\frac{\lambda}{b}$	$\frac{b-a/2}{b}$
2	7.5488	0.7531	0.7500
3	5.3658	0.8353	0.8333
4	4.2744	0.8765	0.8750
8	2.6372	0.9383	0.9375
16	1.8186	0.9691	0.9688

Appendix V

Realistic Model: Structural Variations

First, the effect of μ^0-variations on the potential and concentration profiles is inspected. Even in the case of an ideally abrupt junction, it is clear that the first layer ($\frac{x'}{a} = 0$) perceives a different environment than the other layers ($\frac{x'}{a} > 0$). Consider the extreme case in which interactions between the atoms in the first layer and the electron conductor are ignored. Then the bonding situation resembles that of a surface ion while for the layers $\frac{x'}{a} = 1, 2, \ldots$ a bulk environment would approximately apply. In such a model μ^0 is reduced to $\beta\mu^0$ at $\frac{x'}{a} = 0$, whereby a typical value of β may be $\frac{2}{3}$. Then, even if the Poisson-Boltzmann picture is stuck to, the analysis becomes marginally more complicated.

Now the GC-solution applies only from $\frac{x'}{a} = 1$ to ∞ which we formally write as $\psi\left(\frac{x'}{a} \geq 1\right) = \psi_{GC}(\psi_1; \frac{x'}{a})$. In particular, the integrated charge Q_1 from $\frac{x'}{a} = 1$ to $\frac{x'}{a} = \infty$ can be obtained as $Q_1 = f_{GC}(\psi_1)$.

For the position x' between $-b$ and 0 and x' between 0 and a, Gauss' law and the constancy of the electrochemical potential have to be applied separately, which together with charge conservation supplies enough equations set to solve the problem.

In detail for $b = a$:

(i) $\frac{\psi_0 - \psi_s}{a}\frac{RT}{F} = \frac{Q}{\varepsilon}$

(ii) $\left(\frac{\psi_0 - \psi_s}{a} - \frac{\psi_1 - \psi_0}{a}\right)\frac{RT}{F} = \frac{q_0}{\varepsilon}$

(iii) $q_0 = c_\infty a F e^{-\frac{\Delta\mu^0}{RT}}(e^{-\psi_0} - e^{\psi_0})$

(iv) $Q_1 = f_{GC}(\psi_1)$

(v) $Q = Q_1 + q_0$

The five unknowns ψ_s, ψ_0, ψ_1, Q_1, q_0 can be calculated from these five equations if Q is taken as independent variable.

In terms of Eq. (iii), it follows from the constancy of $\tilde{\mu}_+$ and $\tilde{\mu}_-$, whereby now μ^0 at $x' = 0$ differs from $\mu^0(x' > 0)$ by $\Delta\mu^0$, leading to

$$\frac{c_\pm(\frac{x'}{a} = 0)}{c_\infty} = e^{-\frac{\Delta\mu^0}{RT}} e^{\mp\psi_0} \tag{A.V.1}$$

and hence $q_0 = Fa(c_+ - c_-)$ follows as Eq. (iii). In the case of low potential ($\psi \ll 1$) where from $\frac{x'}{a} = 1$ on an exponential solution is valid. The solutions for the potentials then follow as

$$\psi\left(\frac{x'}{a} > 1\right) = \psi_1 e^{-\frac{x-a}{\lambda}} \tag{A.V.2a}$$

$$\psi\left(\frac{x'}{a} = 1\right) = Q(-2c_\infty F e^{-\frac{\Delta\mu^0}{RT}} - \frac{2c_\infty \lambda RTF a^{-1}}{RT + 2ac_\infty \lambda F^2 \varepsilon^{-1}})^{-1} \frac{RT}{F} (\frac{RT}{F} + \frac{2ac_\infty \lambda F}{\varepsilon})^{-1} \tag{A.V.2b}$$

$$\psi\left(\frac{x'}{a} = 0\right) = Q(-2c_\infty F e^{-\frac{\Delta\mu^0}{RT}} - \frac{2c_\infty \lambda RTF a^{-1}}{RT + 2ac_\infty \lambda F^2 \varepsilon^{-1}})^{-1} \tag{A.V.2c}$$

If we nullify $\Delta\mu^0$, we obtain

$$\frac{\psi_1}{\psi_0} \approx \frac{RT}{F} \frac{1}{\frac{RT}{F} + \frac{a}{\lambda}\frac{RT}{F}} \approx 1 - \frac{a}{\lambda} \approx e^{-\frac{a}{\lambda}} \tag{A.V.3}$$

as it should be.

While the consideration of the conductance is essentially unaffected (given total charge), the profiles for concentrations and electric potentials are now more realistic close to the interface. Fig. A.V.1 shows a comparison between the profiles for electric potential and the charge carrier concentration if in the first layer μ^0 differs from the value in the bulk by $\Delta\mu^0$, but the same overall excess charge is assumed. If $\Delta\mu^0$ is such that now the occupation of the first layer is favored (disfavored), the higher (lower) occupancy is naturally at the cost of lower (higher) c-values in the layers beneath (constant total charge assumed). Such results might provide a better understanding of the concentration profiles at heterojunctions involving solid electrolytes.

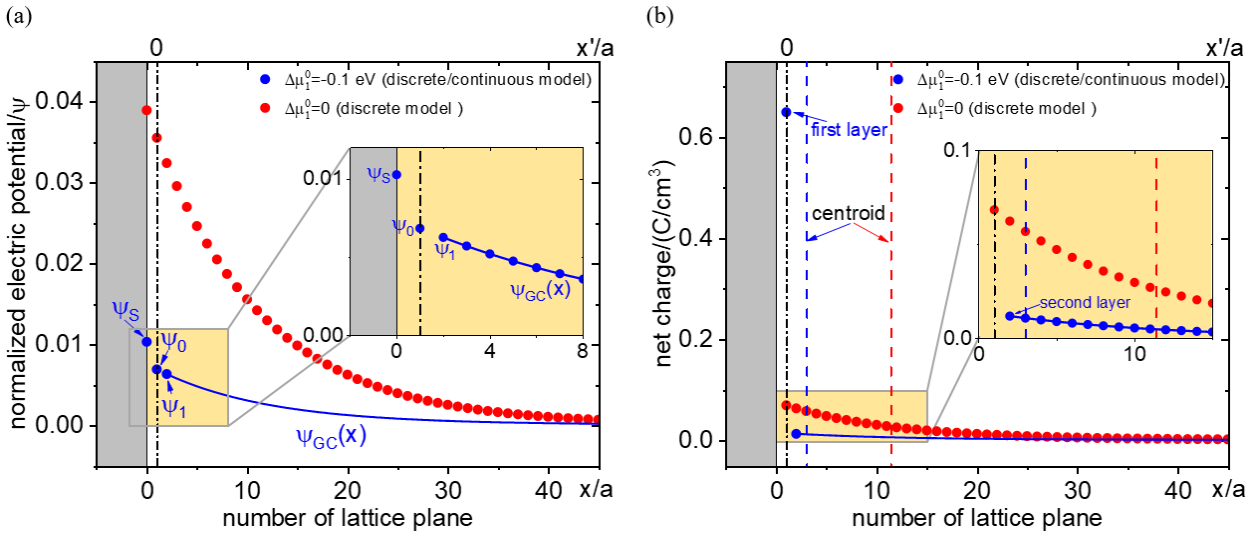

Fig. A. V. 1 The profiles of (a) electric potential and (b) charge carrier concentration shown as a function of number of lattice plane. The blue data shows the model with μ^0-variation in the first layer adjacent to an electron conductor by $\Delta\mu^0$(=-0.1 eV) with respect to the bulk (all the other layers). From second layer on the bulk value is applied. The blue curve shows the continuum model from second layer on. The red data shows the discrete model without μ^0-variation. Blue and red dashed lines in (b) indicate the positions of centroid for both cases (with or without μ^0-variation). Black dash-dotted line refers to the position of first layer. ψ_s, ψ_0 and ψ_1 in (a) refer to the normalized electric potential on the surface of electron conductor, in the first and second layer of ionic conductor, respectively. Simulation parameters: lattice spacing $\Delta x'$=0.1 nm; dielectric constant ε=10; $\phi_s - \phi_\infty$=-1 mV; c_∞=1 ×10^{-5} mol/cm^3; T=298 K. Same total charge is applied for both models.

Fig. A.V.2 shows the examples of centroid and space charge capacitance at various $\Delta\mu^0$-values in the first layer adjacent to an interface. As an example of practical worth, defect formation values for $SrTiO_3$ derived from DFT modelling are taken (*121*) and apply the present approach to it (Fig. A.V.3). Another practical example is the results for fully ionized oxygen vacancies in MgO using the formation values calculated in Ref. (*122*) (Fig. A.V.4). The examples demonstrate that the consideration of atomistic modeling of the near-surface situation and the application of the composite approach is a simple powerful tool to tackle structural or elastic perturbations close to the interface.

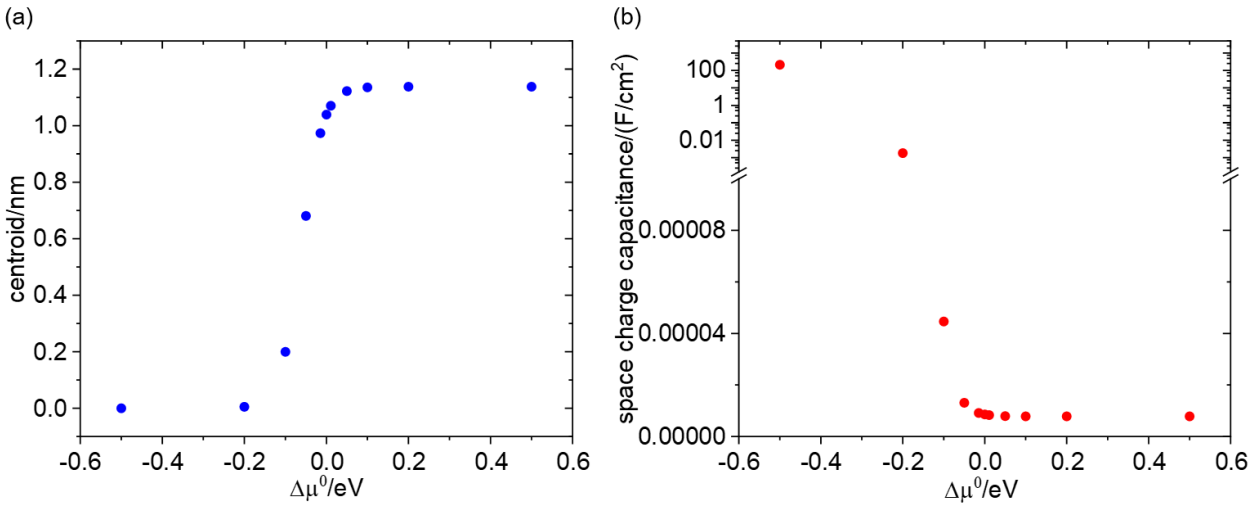

Fig. A. V. 2 Centroid (a) and space charge capacitance (b) as a function of μ^0-variation in the first layer ($\Delta\mu^0$). From second layer on the bulk value is applied. Simulation parameters: lattice spacing $\Delta x'$=0.1 nm; dielectric constant ε=10; $\phi_0 - \phi_\infty$=-1 mV; c_∞=1 ×10^{-5} mol/cm^3; T=298 K. Same total charge is applied.

Table A. V. 1 Set of equations for solving the space charge problem if μ^0 varies.

(1)	$\frac{\psi_0 - \psi_s}{a}\frac{RT}{F} = \frac{Q}{\varepsilon}$
(2)	$\left(\frac{\psi_0 - \psi_s}{a} - \frac{\psi_1 - \psi_0}{a}\right)\frac{RT}{F} = \frac{q_0}{\varepsilon}$
(3)	$\left(\frac{\psi_1 - \psi_0}{a} - \frac{\psi_2 - \psi_1}{a}\right)\frac{RT}{F} = \frac{q_1}{\varepsilon}$
…	…
(p+1)	$\left(\frac{\psi_{p-1} - \psi_{p-2}}{a} - \frac{\psi_p - \psi_{p-1}}{a}\right)\frac{RT}{F} = \frac{q_{p-1}}{\varepsilon}$
(p+2)	$q_0 = c_\infty aFe^{-\frac{\Delta\mu_1^0}{RT}}(e^{-\psi_0} - e^{\psi_0})$
…	…
(2p+1)	$q_{p-1} = c_\infty aFe^{-\frac{\Delta\mu_p^0}{RT}}(e^{-\psi_{p-1}} - e^{\psi_{p-1}})$
(2p+2)	$Q_p = f_{GC}(\psi_p)$
(2p+3)	$Q = Q_p + q_0 + q_1 + \cdots + q_{p-1}$

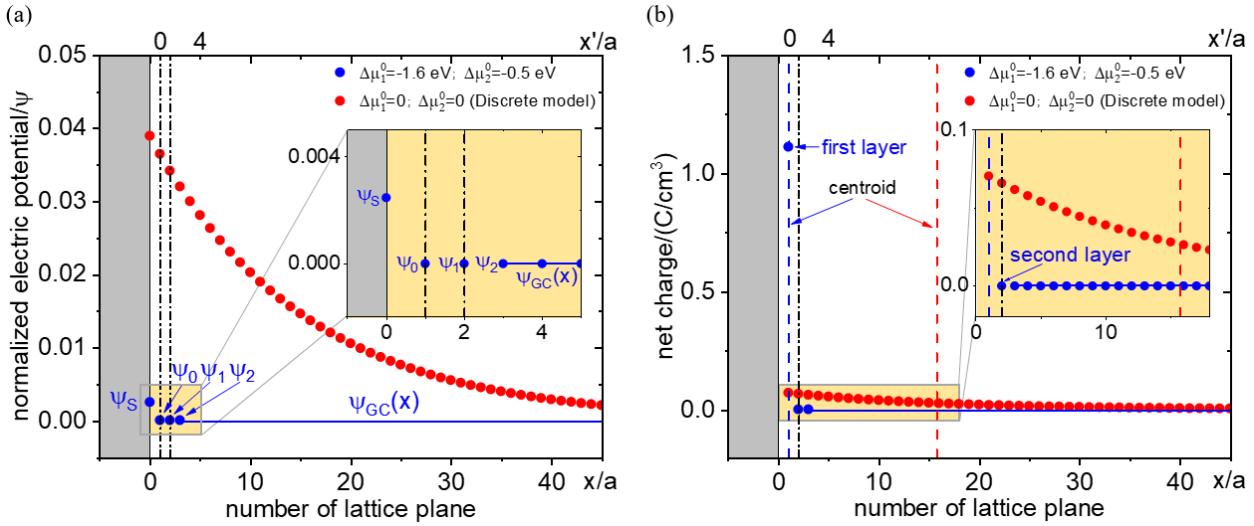

Fig. A. V. 3 The profiles of (a) electric potential and (b) charge carrier concentration for oxygen vacancies in $SrTiO_3$. The blue data shows the model with μ^0-variation in the first two layers adjacent to the surface by $\Delta\mu_1^0$, $\Delta\mu_2^0$ with respect to the bulk. From third layer on the bulk value is applied. The blue curve shows the continuum model from third layer on. The red data shows the discrete model without μ^0-variation. Blue and red dashed lines in (b) indicate the positions of centroid for both cases (with or without μ^0-variation). Black dash-dotted lines refer to the positions of first two layers. Simulation parameters: lattice spacing $\Delta x'$ =0.39 nm; dielectric constant ε =300; $\phi_0 - \phi_\infty$ =-1 mV; $c_\infty = 1 \times 10^{-5}$ mol/cm^3. Oxygen vacancy formation energy: first layer (5.9 eV); second layer (7 eV); bulk (7.5 eV), $\Delta\mu_1^0 = -1.6$ eV; $\Delta\mu_2^0 = -0.5$ eV (F^0, neutral) Ref. (*121*); T=298 K. Same total charge is applied for both models.

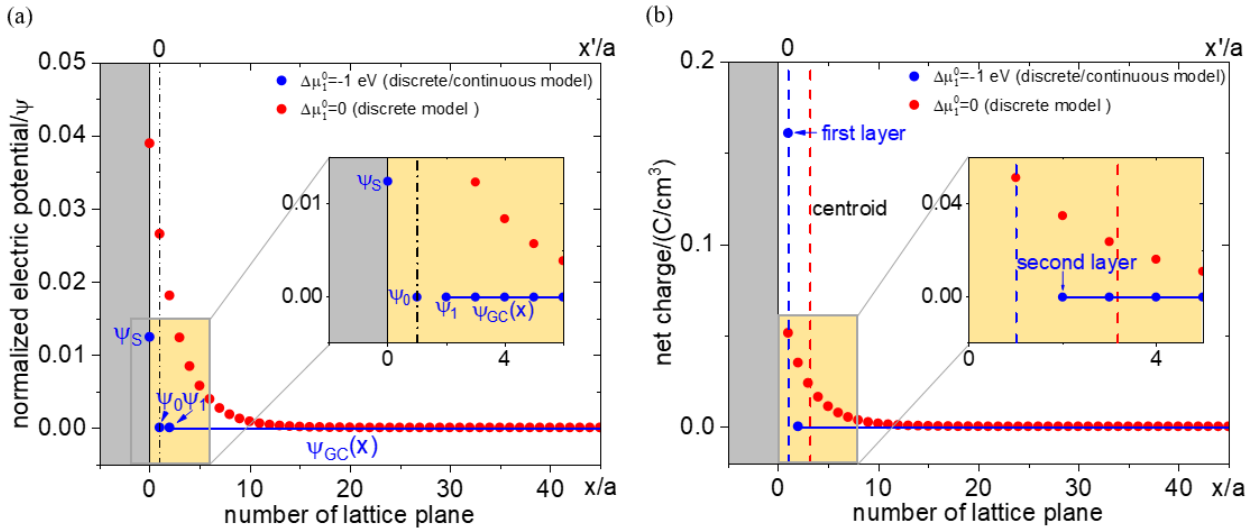

Fig. A. V. 4 The profiles of (a) electric potential and (b) charge carrier concentration for fully ionized oxygen vacancies in MgO. The blue data shows the model with μ^0-variation in the first layer adjacent to

the surface by $\Delta\mu^0$ (=-1 eV) with respect to the bulk according to Ref. (*122*). From second layer on the bulk value is applied. The blue curve shows the continuum model from second layer on. The red data shows the discrete model without μ^0-variation. Blue and red dashed lines in (b) indicate the positions of centroid for both cases (with or without μ^0-variation). Black dash-dotted line refers to the position of first layer. Simulation parameters: lattice spacing $\Delta x'$ =0.42 nm; dielectric constant ε =10; $\phi_0 - \phi_\infty$ =-1 mV; c_∞=1 $\times 10^{-5}$ mol/cm^3; T=298 K. Same total charge is applied for both models.

Appendix VI

Saturation Effects

Not only can μ^0-variations be implemented in a straightforward way, also entropic saturation effects can be included. Here a Boltzmann distribution has to be replaced by a Fermi-type of distribution, i.e. $\frac{c_\pm}{c_{total,\pm}-c_\pm}$ where $c_{total,\pm}$ is the concentration of $\pm$ lattice sites (such effects on the electron conductor side are ignored). This correction is needed as the number of available sites (lattice sites) are no longer constant but become critical. The approach that splitting into discretization close to the interface and a continuous description further away is very valuable, as saturation effects are expected to play a major role only close to the interface. In order to concentrate on this effect, $\Delta\mu^0 = 0$ for $\frac{x'}{a} > 0$ is set and consider low potential ($\psi \ll 1$). The exponential profile then can be used for $\frac{x'}{a} \geq 1$. At $x' = 0$, $\frac{c_\pm(0)}{c_\infty}$ in Eq. (A. V. 1) has been replaced by $\frac{c_\pm(0)}{c_{total,\pm}-c_\pm(0)}\frac{c_{total,\pm}}{c_\infty}$ with the results for local charge and potential (see Table A. VI. 1).

Now saturation effects in the first layer are considered. As shown in Fig. A. VI. 1**,** evidently the qualitative effect is similar as if in the first layer $\Delta\mu^0$ were positive. The lower occupancy (at given total charge) leads then to a shift of $\mathcal{L}$ towards bulk corresponding to a lower space charge capacitance. Clearly the depression in the first layer to values lower than in the second layer (where saturation is neglected, Fig. A. VI. 1a,b) would indicate the necessity to consider saturation also in the other layers or to restrict to smaller effects (Fig. A. VI. 1c,d).

A limited charge per layer has also been considered in Ref. (*36*). In addition, the charge on the metal side may be subjected to restrictions of the density of states.

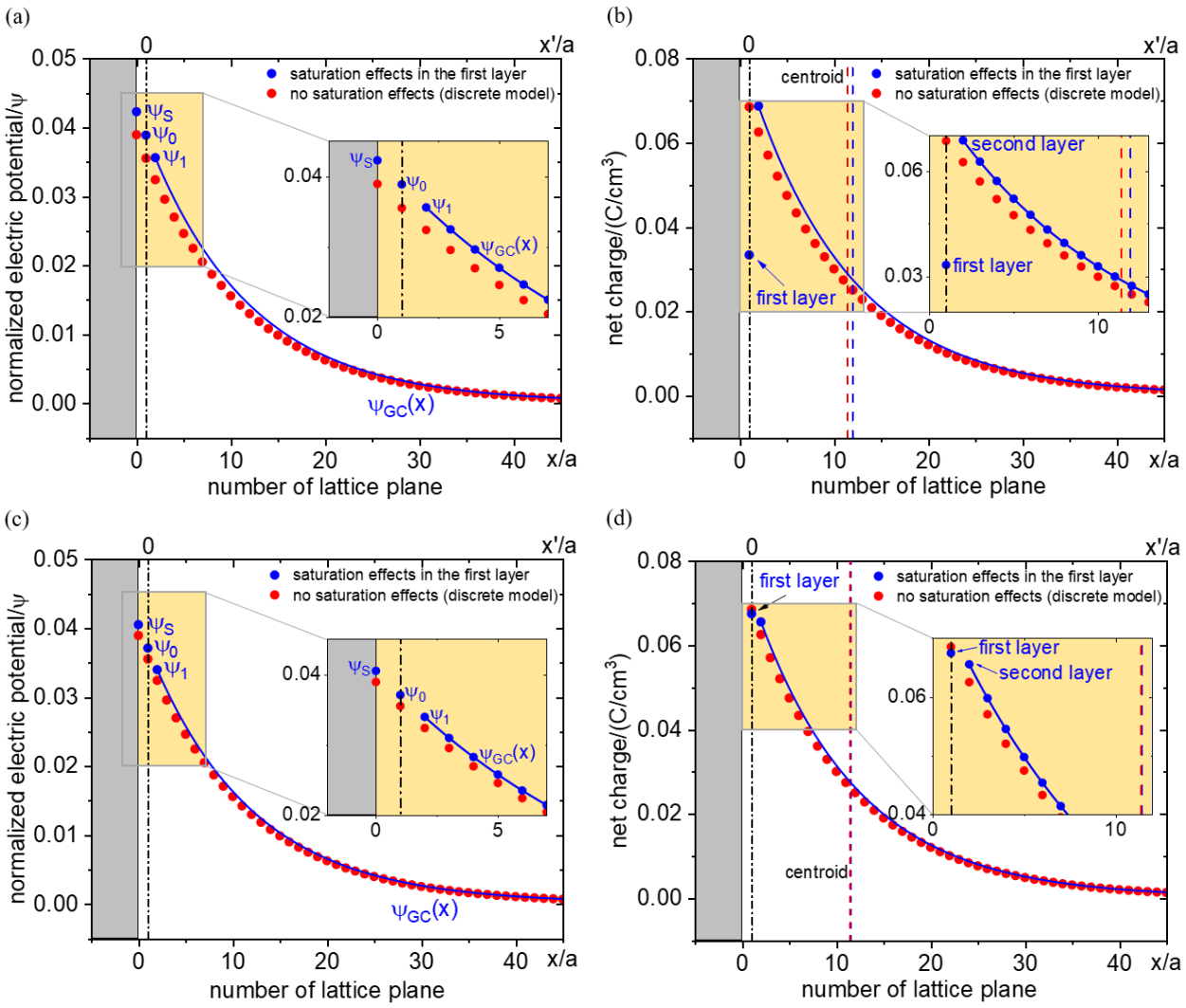

Fig. A. VI. 1 The profiles of (a), (c) electric potential and (b), (d) charge carrier concentration as a function of number of lattice plane. The blue data shows the model with saturation effects in the first layer adjacent to the interface. The blue curve shows the continuum model from second layer on. The red data shows the discrete model with absence of saturation effects. Blue and red dashed lines in (b), (d) indicate the positions of centroid for both cases (with or without saturation effects). Black dash-dotted line refers to the position of first layer. Simulation parameters: lattice spacing $\Delta x'$=0.1 nm; dielectric constant ε=10; $\phi_s - \phi_\infty$=-1 mV; μ^0 is constant; T=298 K. (a), (b) c_∞/c_{total}= 0.5 (unrealistic value). The charge concentration at first layer is smaller than that at next layers. Then considering saturation effects on next layers is necessary. (c), (d) c_∞/c_{total}= 0.03. In this situation, the charge concentration at first layer is suppressed, but still higher than that at second layer. The qualitative effect is similar as if in the first layer $\Delta\mu^0$ were positive (the centroid shift towards bulk direction slightly).

Table A. VI. 1 Set of equations for solving the space charge problem if saturation occurs.

(1)	$\frac{\psi_0 - \psi_s}{a}\frac{RT}{F} = \frac{Q}{\varepsilon}$
(2)	$\left(\frac{\psi_0 - \psi_s}{a} - \frac{\psi_1 - \psi_0}{a}\right)\frac{RT}{F} = \frac{q_0}{\varepsilon}$
(3)	$\left(\frac{\psi_1 - \psi_0}{a} - \frac{\psi_2 - \psi_1}{a}\right)\frac{RT}{F} = \frac{q_1}{\varepsilon}$
…	…
(p+1)	$\left(\frac{\psi_{p-1} - \psi_{p-2}}{a} - \frac{\psi_p - \psi_{p-1}}{a}\right)\frac{RT}{F} = \frac{q_{p-1}}{\varepsilon}$
(p+2)	$q_0 = c_\infty aF\left(\frac{e^{-\frac{\Delta\mu_1^0}{RT}}e^{-\psi_0}}{1 + \frac{c_\infty}{c_{total,\pm}}e^{-\frac{\Delta\mu_1^0}{RT}}e^{-\psi_0}} - \frac{e^{-\frac{\Delta\mu_1^0}{RT}}e^{\psi_0}}{1 + \frac{c_\infty}{c_{total,\pm}}e^{-\frac{\Delta\mu_1^0}{RT}}e^{\psi_0}}\right)$
…	…
(2p+1)	$q_{p-1} = c_\infty aFe^{-\frac{\Delta\mu_p^0}{RT}}(e^{-\psi_{p-1}} - e^{\psi_{p-1}})$
(2p+2)	$Q_p = f_{GC}(\psi_p)$
(2p+3)	$Q = Q_p + q_0 + q_1 + \cdots + q_{p-1}$

List of Symbols

A	Atomic size in the electron conductor
a	Atomic size in the solid ion conductor or the area (depending on the context)
a_{Li}	The activity of lithium
a_M	The activity of M
b	The distance between the two adjacent discretely charged layers
c_h	Concentration of electron hole
c_i	Concentration of metal ion interstitial
c_m	Concentration (number of moles per volume) of species m
c_n	Concentration of electron
$\mathrm{c_n(x)}$	The amount of active electrons in the substrate
c_v	Concentration of metal ion vacancy
c_∞	Bulk concentration
c_+	Local concentration of positive charge
c_-	Local concentration of negative charge
C	The total interfacial capacitance
C	Doping content
C_{H}	Helmholtz capacitance
C_{SC}	The space charge capacitance (per area)
$C^{\perp}$	Space charge capacitance (perpendicular to the interface)
d	Oxide thickness
e'	Electron
F	Faraday constant

List of Symbols

$h^{\cdot}$	Electron hole
I	Current or the area of the Ru component before sputtering in XPS spectra (depending on the context)
I_0	The area of the Ru component after sputtering in XPS spectra
i	Li-interstitials
IMFP	The inelastic mean free path
K_M	Mass action constant for M storage
K_B	Mass action constant of electron-hole equilibrium
K_F	Frenkel constant
K_{het}	Heterogeneous mass action constant
L	Thickness of film
M	Metal
$M_i^{\cdot}$	Metal ion interstitial
M_M	Cation on its regular site
N	The exponent in power laws for Q as a function of the lithium activity
n	Excess electrons
Q	Total stored charge
q_i	The area-specific charge at the i-th plane (positioned at x_i')
q_{bulk}	The neutral bulk charge density
Q_{int}	Interfacial storage capacity
R	Universal gas constant
$R^{\perp}$	Interfacial resistance (perpendicular to the interface)
s	Charge free zone distance
T	Temperature
u	Mobility
V	Molar volume
V_i	Vacancy on the interstitial site
V_{Li}'	Lithium ion vacancy
V_M'	Metal ion vacancy
x	Origin of coordinate for continuum model

x'	Origin of coordinate for discrete model
$Y^{\parallel}$	The conductance parallel to the interface
z_m	Charge number of species m
Z'	The real part of the impedance
Z''	The imaginary part of the impedance
$Z^{\perp}$	Normalized interfacial resistance (perpendicular to the interface) with respect to the area
δ	The molar fraction of Li
ε	Relative permittivity
$\bar{\varepsilon}$	Mean relative permittivity
ε_α	Relative permittivity of phase α
ε_β	Relative permittivity of phase β
ε_0	Vacuum permittivity
ε_1	Relative permittivity in the first layer adjacent to an interface
λ	Debye length
μ^0	The standard chemical potentials of the respective charge carriers
$\tilde{\mu}_{e'}$	Electrochemical potential of e'
$\tilde{\mu}_M$	Electrochemical potential of M
$\tilde{\mu}_{M_i^{\cdot}}$	Electrochemical potential of $M_i^{\cdot}$
ρ	Charge density
ϕ	Electrostatic potential
ϕ_∞	Electric potential of bulk
$\mathcal{L}$	The centroid
$\mathcal{L}_c$	The centroid in the continuum model
$\mathcal{L}_d$	The centroid in the discrete model
η	The applied bias voltage
ζ	The concentration enhancement (the concentration relative to that in the bulk (c_∞))
ξ	The local coordinate normalized to the Debye length ($\xi = \frac{x}{\lambda}$)
æ	The electrical field effect between the two outermost layers in TiO_2 and substrate

References

1. B. Dunn, H. Kamath, J.-M. Tarascon, Electrical Energy Storage for the Grid: A Battery of Choices. *Science* **334**, 928-935 (2011).
2. M. Armand, J. M. Tarascon, Building better batteries. *Nature* **451**, 652-657 (2008).
3. P. G. Bruce, B. Scrosati, J.-M. Tarascon, Nanomaterials for Rechargeable Lithium Batteries. *Angewandte Chemie International Edition* **47**, 2930-2946 (2008).
4. M. S. Whittingham, Electrical Energy Storage and Intercalation Chemistry. *Science* **192**, 1126-1127 (1976).
5. K. Mizushima, P. Jones, P. Wiseman, J. B. Goodenough, Li_xCoO_2 (0< x<-1): A new cathode material for batteries of high energy density. *Materials Research Bulletin* **15**, 783-789 (1980).
6. J. Maier, Thermodynamics of electrochemical lithium storage. *Angewandte Chemie International Edition* **52**, 4998-5026 (2013).
7. J. Maier, *Physical chemistry of ionic materials: ions and electrons in solids*. (John Wiley & Sons, 2023).
8. C. Xiao, R. Usiskin, J. Maier, Passivation Layers in Lithium and Sodium Batteries: Potential Profiles, Stabilities, and Voltage Drops. *Advanced Functional Materials* **31**, 2100938 (2021).
9. B. E. Conway, *Electrochemical supercapacitors: scientific fundamentals and technological applications*. (Springer Science & Business Media, 2013).
10. P. Simon, Y. Gogotsi, B. Dunn, Where Do Batteries End and Supercapacitors Begin? *Science* **343**, 1210-1211 (2014).
11. P. Simon, Y. Gogotsi, Materials for electrochemical capacitors. *Nature Materials* **7**, 845-854 (2008).
12. Y. Shao, M. F. El-Kady, J. Sun, Y. Li, Q. Zhang, M. Zhu, H. Wang, B. Dunn, R. B. Kaner, Design and Mechanisms of Asymmetric Supercapacitors. *Chemical Reviews* **118**, 9233-9280 (2018).
13. M. Salanne, B. Rotenberg, K. Naoi, K. Kaneko, P. L. Taberna, C. P. Grey, B. Dunn, P. Simon, Efficient storage mechanisms for building better supercapacitors. *Nature Energy* **1**, 16070 (2016).

14. W. Gu, G. Yushin, Review of nanostructured carbon materials for electrochemical capacitor applications: advantages and limitations of activated carbon, carbide-derived carbon, zeolite-templated carbon, carbon aerogels, carbon nanotubes, onion-like carbon, and graphene. *Wiley Interdisciplinary Reviews: Energy and Environment* **3**, 424-473 (2014).
15. A. C. Forse, C. Merlet, J. M. Griffin, C. P. Grey, New Perspectives on the Charging Mechanisms of Supercapacitors. *Journal of the American Chemical Society* **138**, 5731-5744 (2016).
16. J. M. Griffin, A. C. Forse, W.-Y. Tsai, P.-L. Taberna, P. Simon, C. P. Grey, In situ NMR and electrochemical quartz crystal microbalance techniques reveal the structure of the electrical double layer in supercapacitors. *Nature Materials* **14**, 812-819 (2015).
17. J. M. Griffin, A. C. Forse, C. P. Grey, Solid-state NMR studies of supercapacitors. *Solid State Nuclear Magnetic Resonance* **74-75**, 16-35 (2016).
18. V. Augustyn, P. Simon, B. Dunn, Pseudocapacitive oxide materials for high-rate electrochemical energy storage. *Energy & Environmental Science* **7**, 1597-1614 (2014).
19. J. Wang, J. Polleux, J. Lim, B. Dunn, Pseudocapacitive Contributions to Electrochemical Energy Storage in TiO_2 (Anatase) Nanoparticles. *The Journal of Physical Chemistry C* **111**, 14925-14931 (2007).
20. Q. Wei, X. Chang, D. Butts, R. DeBlock, K. Lan, J. Li, D. Chao, D.-L. Peng, B. Dunn, Surface-redox sodium-ion storage in anatase titanium oxide. *Nature Communications* **14**, 7 (2023).
21. V. Augustyn, J. Come, M. A. Lowe, J. W. Kim, P.-L. Taberna, S. H. Tolbert, H. D. Abruña, P. Simon, B. Dunn, High-rate electrochemical energy storage through Li^+ intercalation pseudocapacitance. *Nature Materials* **12**, 518-522 (2013).
22. S. Lou, Y. Zhao, J. Wang, G. Yin, C. Du, X. Sun, Ti-Based Oxide Anode Materials for Advanced Electrochemical Energy Storage: Lithium/Sodium Ion Batteries and Hybrid Pseudocapacitors. *Small* **15**, 1904740 (2019).
23. S. Fleischmann, J. B. Mitchell, R. Wang, C. Zhan, D.-e. Jiang, V. Presser, V. Augustyn, Pseudocapacitance: From Fundamental Understanding to High Power Energy Storage Materials. *Chemical Reviews* **120**, 6738-6782 (2020).
24. C. Liang, Conduction characteristics of the lithium iodide-aluminum oxide solid electrolytes. *Journal of the Electrochemical Society* **120**, 1289 (1973).
25. J. Maier, Space charge regions in solid two-phase systems and their conduction contribution—I. Conductance enhancement in the system ionic conductor-'inert'phase and application on AgC1: Al_2O_3 and AgC1: SiO_2. *Journal of Physics Chemistry of Solids* **46**, 309-320 (1985).

26. J. Maier, Nanoionics: ion transport and electrochemical storage in confined systems. *Nature materials* **4**, 805-815 (2005).
27. C.-C. Chen, J. Maier, Decoupling electron and ion storage and the path from interfacial storage to artificial electrodes. *Nature Energy* **3**, 102-108 (2018).
28. J. Maier, Ionic conduction in space charge regions. *Progress in Solid State Chemistry* **23**, 171-263 (1995).
29. L. Fu, C.-C. Chen, D. Samuelis, J. Maier, Thermodynamics of Lithium Storage at Abrupt Junctions: Modeling and Experimental Evidence. *Physical Review Letters* **112**, 208301 (2014).
30. H. Li, G. Richter, J. Maier, Reversible formation and decomposition of LiF clusters using transition metal fluorides as precursors and their application in rechargeable Li batteries. *Advanced Materials* **15**, 736-739 (2003).
31. H. Li, P. Balaya, J. Maier, Li-storage via heterogeneous reaction in selected binary metal fluorides and oxides. *Journal of the Electrochemical Society* **151**, A1878 (2004).
32. C.-C. Chen, L. Fu, J. Maier, Synergistic, ultrafast mass storage and removal in artificial mixed conductors. *Nature* **536**, 159-164 (2016).
33. S.-K. Jung, H. Kim, M. G. Cho, S.-P. Cho, B. Lee, H. Kim, Y.-U. Park, J. Hong, K.-Y. Park, G. Yoon, Won M. Seong, Y. Cho, Myoung H. Oh, H. Kim, H. Gwon, I. Hwang, T. Hyeon, W.-S. Yoon, K. Kang, Lithium-free transition metal monoxides for positive electrodes in lithium-ion batteries. *Nature Energy* **2**, 16208 (2017).
34. Q. Li, H. Li, Q. Xia, Z. Hu, Y. Zhu, S. Yan, C. Ge, Q. Zhang, X. Wang, X. Shang, S. Fan, Y. Long, L. Gu, G.-X. Miao, G. Yu, J. S. Moodera, Extra storage capacity in transition metal oxide lithium-ion batteries revealed by in situ magnetometry. *Nature materials* **20**, 76-83 (2021).
35. X. Li, J. Su, Z. Li, Z. Zhao, F. Zhang, L. Zhang, W. Ye, Q. Li, K. Wang, X. Wang, H. Li, H. Hu, S. Yan, G.-X. Miao, Q. Li, Revealing interfacial space charge storage of $Li^+/Na^+/K^+$ by operando magnetometry. *Science Bulletin*, (2022).
36. N. Sata, K. Eberman, K. Eberl, J. Maier, Mesoscopic fast ion conduction in nanometre-scale planar heterostructures. *Nature* **408**, 946-949 (2000).
37. L. Fu, K. Tang, H. Oh, K. Manickam, T. Bräuniger, C. V. Chandran, A. Menzel, M. Hirscher, D. Samuelis, J. Maier, "Job-Sharing" Storage of Hydrogen in Ru/Li_2O Nanocomposites. *Nano Letters* **15**, 4170-4175 (2015).
38. C. Barlow Jr, in *Physical Chemistry, An Advanced Treatise*, H. Eyring, Ed. (Academic Press Inc. , New York, 1970), vol. IXA, pp. 167-246.
39. R. D. Armstrong, B. R. Horrocks, The double layer structure at the metal-solid electrolyte interface. *Solid State Ionics* **94**, 181-187 (1997).

40. C.-C. Chen, J. Maier, Space charge storage in composites: thermodynamics. *Physical Chemistry Chemical Physics* **19**, 6379-6396 (2017).
41. H. Helmholtz, Ueber einige Gesetze der Vertheilung elektrischer Ströme in körperlichen Leitern, mit Anwendung auf die thierisch-elektrischen Versuche (Schluss.). *Annalen der Physik* **165**, 353-377 (1853).
42. H. Helmholtz, Studien über electrische Grenzschichten. *Annalen der Physik* **243**, 337-382 (1879).
43. M. Gouy, Sur la constitution de la charge électrique à la surface d'un électrolyte. *J. Phys. Theor. Appl.* **9**, 457-468 (1910).
44. D. L. Chapman, A contribution to the theory of electrocapillarity. *The London, Edinburgh, Dublin philosophical magazine journal of science* **25**, 475-481 (1913).
45. E. Huckel, P. Debye, Zur theorie der elektrolyte. i. gefrierpunktserniedrigung und verwandte erscheinungen. *Phys. Z* **24**, 185-206 (1923).
46. O. Stern, Zur theorie der elektrolytischen doppelschicht. *Zeitschrift für Elektrochemie und angewandte physikalische Chemie* **30**, 508-516 (1924).
47. D. C. Grahame, The electrical double layer and the theory of electrocapillarity. *Chemical reviews* **41**, 441-501 (1947).
48. O. K. Rice, Application of the Fermi statistics to the distribution of electrons under fields in metals and the theory of electrocapillarity. *Physical Review* **31**, 1051 (1928).
49. N. Lang, W. Kohn, Theory of metal surfaces: charge density and surface energy. *Physical Review B* **1**, 4555 (1970).
50. N. Lang, W. Kohn, Theory of metal surfaces: work function. *Physical Review B* **3**, 1215 (1971).
51. S. M. Sze, K. K. Ng, *Physics of semiconductor devices*. (John wiley & sons, 2006).
52. J. M. Bockris, A. K. Reddy, *Modern Electrochemistry: Volume 1: Ionics*. (Plenum Press, 1998).
53. C. Li, L. Gu, X. Guo, D. Samuelis, K. Tang, J. Maier, Charge Carrier Accumulation in Lithium Fluoride Thin Films due to Li-Ion Absorption by Titania (100) Subsurface. *Nano Letters* **12**, 1241-1246 (2012).
54. G. Gregori, R. Merkle, J. Maier, Ion conduction and redistribution at grain boundaries in oxide systems. *Progress in Materials Science* **89**, 252-305 (2017).
55. J.-Y. Shin, D. Samuelis, J. Maier, Sustained Lithium-Storage Performance of Hierarchical, Nanoporous Anatase TiO_2 at High Rates: Emphasis on Interfacial Storage Phenomena. *Advanced Functional Materials* **21**, 3464-3472 (2011).
56. I.-D. Kim, A. Rothschild, H. L. Tuller, Advances and new directions in gas-sensing devices. *Acta Materialia* **61**, 974-1000 (2013).

57. J. M. Thomas, W. J. Thomas, *Principles and practice of heterogeneous catalysis*. (VCH, Weinheim, 1997).
58. P. Lupetin, G. Gregori, J. Maier, Mesoscopic Charge Carriers Chemistry in Nanocrystalline $SrTiO_3$. *Angewandte Chemie International Edition* **49**, 10123-10126 (2010).
59. J. Maier, Space Charge Regions in Solid Two Phase Systems and Their Conduction Contribution — II Contact Equilibrium at the Interface of Two Ionic Conductors and the Related Conductivity Effect. *Berichte der Bunsengesellschaft für physikalische Chemie* **89**, 355-362 (1985).
60. L. Onsager, Theories of Concentrated Electrolytes. *Chemical Reviews* **13**, 73-89 (1933).
61. H. Casimir, Tweede Symposium over sterke Elektrolyten en de ElektrischeDubbellaag. *by Sectie voor Kolloid-chemie, Ned. Chem. Ver. Utrecht*, 1 (1944).
62. J. Mayer, M. Mayer, *Statistical Mechanics*. John Wiley. *New York,* (1940).
63. A. R. Allnatt, A. B. Lidiard, *Atomic transport in solids*. (Cambridge University Press, 2003).
64. A. Allnatt, E. Loftus, Physical cluster theory of point defect interactions. II. Application to AgCl doped with $CdCl_2$. *The Journal of Chemical Physics* **59**, 2550-2559 (1973).
65. A. Allnatt, E. Loftus, Erratum: Physical cluster theory of point defect interactions. II. Application to AgCl doped with $CdCl_2$. *The Journal of Chemical Physics* **71**, 5388-5388 (1979).
66. A. Münster, *Statistical thermodynamics II*, chapter 18, Springer, (1974).
67. J. O. M. Bockris, A. K. Reddy, *Modern Electrochemistry 1*. Plenum Press, New York (1977).
68. J. Lyklema, *Fundamentals of interface and colloid science*, Volume I, Fundamentals, chapter 4.3 c, Academic press, London, (1991).
69. J. Lyklema. *Fundamentals of interface and colloid science*, Volume II, Solid-liquid interfaces, chapter 3.6 a, Academic press, London, (2001).
70. B. Conway, *Physical Chemistry: An Advanced Treatise*. *Vol. IXA,"Electrochemistry," H. Eyring, Ed., Academic Press, New York, NY,* (1970).
71. K. K. Adepalli, M. Kelsch, R. Merkle, J. Maier, Influence of line defects on the electrical properties of single crystal TiO_2. *Advanced Functional Materials* **23**, 1798-1806 (2013).
72. A. Y. Shul'man, D. Posvyanskii, Solution of Self-Consistent Kohn–Sham and Poisson Equations for Quasi Two-Dimensional Electron Gas in the Accumulation Layer of Semiconductor with Nonparabolic Conduction Band. *Journal of Experimental Theoretical Physics* **130**, 903-934 (2020).

73. M. McEldrew, Z. A. Goodwin, A. A. Kornyshev, M. Z. Bazant, Theory of the double layer in water-in-salt electrolytes. *The journal of physical chemistry letters* **9**, 5840-5846 (2018).
74. M. Z. Bazant, B. D. Storey, A. A. Kornyshev, Double layer in ionic liquids: Overscreening versus crowding. *Physical review letters* **106**, 046102 (2011).
75. M. S. Kilic, M. Z. Bazant, A. Ajdari, Steric effects in the dynamics of electrolytes at large applied voltages. I. Double-layer charging. *Physical review E* **75**, 021502 (2007).
76. J. P. de Souza, M. Z. Bazant, Continuum theory of electrostatic correlations at charged surfaces. *The Journal of Physical Chemistry C* **124**, 11414-11421 (2020).
77. K. Vikrant, W. C. Chueh, R. E. García, Charged interfaces: electrochemical and mechanical effects. *Energy Environmental Science* **11**, 1993-2000 (2018).
78. D. S. Mebane, R. A. De Souza, A generalised space-charge theory for extended defects in oxygen-ion conducting electrolytes: from dilute to concentrated solid solutions. *Energy Environmental Science* **8**, 2935-2940 (2015).
79. S. Braun, C. Yada, A. Latz, Thermodynamically consistent model for space-charge-layer formation in a solid electrolyte. *The Journal of Physical Chemistry C* **119**, 22281-22288 (2015).
80. G. Fisicaro, L. Genovese, O. Andreussi, N. Marzari, S. Goedecker, A generalized Poisson and Poisson-Boltzmann solver for electrostatic environments. *The Journal of chemical physics* **144**, 014103 (2016).
81. C. Xiao, C.-C. Chen, J. Maier, Discrete modeling of ionic space charge zones in solids. *Physical Chemistry Chemical Physics* **24**, 11945-11957 (2022).
82. J. Jamnik, Analysis of the frequency response of schottky junctions in solid-state ionics. *Applied Physics A* **55**, 518-522 (1992).
83. F. Booth, The dielectric constant of water and the saturation effect. *The Journal of Chemical Physics* **19**, 391-394 (1951).
84. F. Booth, Dielectric constant of polar liquids at high field strengths. *The Journal of Chemical Physics* **23**, 453-457 (1955).
85. H. Wang, L. Pilon, Accurate simulations of electric double layer capacitance of ultramicroelectrodes. *The Journal of Physical Chemistry C* **115**, 16711-16719 (2011).
86. R. Van der Berg, P. Blom, J. Cillessen, R. Wolf, Field dependent permittivity in metal-semiconducting $SrTiO_3$ Schottky diodes. *Applied physics letters* **66**, 697-699 (1995).
87. D. J. Bonthuis, S. Gekle, R. R. Netz, Dielectric profile of interfacial water and its effect on double-layer capacitance. *Physical review letters* **107**, 166102 (2011).
88. J.-F. Olivieri, J. T. Hynes, D. Laage, Confined Water's Dielectric Constant Reduction Is Due to the Surrounding Low Dielectric Media and Not to Interfacial Molecular Ordering. *The Journal of Physical Chemistry Letters* **12**, 4319-4326 (2021).

89. H. Kim, Atomic layer deposition of metal and nitride thin films: Current research efforts and applications for semiconductor device processing. *Journal of Vacuum Science Technology B: Microelectronics Nanometer Structures Processing, Measurement, Phenomena* **21**, 2231-2261 (2003).
90. H. Kim, H.-B.-R. Lee, W.-J. Maeng, Applications of atomic layer deposition to nanofabrication and emerging nanodevices. *Thin solid films* **517**, 2563-2580 (2009).
91. H. Kiessig, Untersuchungen zur totalreflexion von röntgenstrahlen. *Annalen der Physik* **402**, 715-768 (1931).
92. H. Wang, V. Srot, B. Fenk, G. Laskin, J. Mannhart, P. A. van Aken, An optimized TEM specimen preparation method of quantum nanostructures. *Micron* **140**, 102979 (2021).
93. P. Poizot, S. Laruelle, S. Grugeon, L. Dupont, J. M. Tarascon, Nano-sized transition-metal oxides as negative-electrode materials for lithium-ion batteries. *Nature* **407**, 496 (2000).
94. K. K. Adepalli, M. Kelsch, R. Merkle, J. Maier, Enhanced ionic conductivity in polycrystalline TiO_2 by "one-dimensional doping". *Physical Chemistry Chemical Physics* **16**, 4942-4951 (2014).
95. Y. S. Hu, L. Kienle, Y. G. Guo, J. Maier, High Lithium Electroactivity of Nanometer-Sized Rutile TiO_2. *Advanced Materials* **18**, 1421-1426 (2006).
96. R. M. McFadden, T. J. Buck, A. Chatzichristos, C.-C. Chen, K. H. Chow, D. L. Cortie, M. H. Dehn, V. L. Karner, D. Koumoulis, C. P. Levy, Microscopic Dynamics of Li^+ in Rutile TiO_2 Revealed by ^8Li β-Detected Nuclear Magnetic Resonance. *Chemistry of Materials* **29**, 10187-10197 (2017).
97. J.-Y. Shin, J. H. Joo, D. Samuelis, J. Maier, Oxygen-deficient $TiO_{2-\delta}$ nanoparticles via hydrogen reduction for high rate capability lithium batteries. *Chemistry of Materials* **24**, 543-551 (2012).
98. J.-Y. Shin, D. Samuelis, J. Maier, Defect chemistry of lithium storage in TiO_2 as a function of oxygen stoichiometry. *Solid State Ionics* **225**, 590-593 (2012).
99. J.-Y. Shin, J. H. Joo, K. K. Adepalli, D. Samuelis, J. Maier, The effects of n-type doping on lithium storage in TiO_2. *Physical Chemistry Chemical Physics* **18**, 8963-8970 (2016).
100. Y. G. Guo, Y. S. Hu, W. Sigle, J. Maier, Superior Electrode Performance of Nanostructured Mesoporous TiO_2 (Anatase) through Efficient Hierarchical Mixed Conducting Networks. *Advanced Materials* **19**, 2087-2091 (2007).
101. J. S. Chen, Y. L. Tan, C. M. Li, Y. L. Cheah, D. Luan, S. Madhavi, F. Y. C. Boey, L. A. Archer, X. W. Lou, Constructing Hierarchical Spheres from Large Ultrathin Anatase TiO_2 Nanosheets with Nearly 100% Exposed (001) Facets for Fast Reversible Lithium Storage. *Journal of the American Chemical Society* **132**, 6124-6130 (2010).

102. A. R. Armstrong, G. Armstrong, J. Canales, R. García, P. G. Bruce, Lithium-Ion Intercalation into TiO_2-B Nanowires. *Advanced Materials* **17**, 862-865 (2005).
103. G. Armstrong, A. R. Armstrong, P. G. Bruce, P. Reale, B. Scrosati, TiO_2(B) Nanowires as an Improved Anode Material for Lithium-Ion Batteries Containing $LiFePO_4$ or $LiNi_{0.5}Mn_{1.5}O_4$ Cathodes and a Polymer Electrolyte. *Advanced Materials* **18**, 2597-2600 (2006).
104. Y. Ren, Z. Liu, F. Pourpoint, A. R. Armstrong, C. P. Grey, P. G. Bruce, Nanoparticulate TiO_2(B): An Anode for Lithium-Ion Batteries. *Angewandte Chemie International Edition* **51**, 2164-2167 (2012).
105. M. Wagemaker, R. van de Krol, A. P. M. Kentgens, A. A. van Well, F. M. Mulder, Two Phase Morphology Limits Lithium Diffusion in TiO_2 (Anatase): A ^{7}Li MAS NMR Study. *Journal of the American Chemical Society* **123**, 11454-11461 (2001).
106. M. Wagemaker, G. J. Kearley, A. A. Van Well, H. Mutka, F. M. Mulder, Multiple Li positions inside oxygen octahedra in lithiated TiO_2 anatase. *Journal of the American Chemical Society* **125**, 840-848 (2003).
107. S. Lunell, A. Stashans, L. Ojamäe, H. Lindström, A. Hagfeldt, Li and Na diffusion in TiO_2 from quantum chemical theory versus electrochemical experiment. *Journal of the American Chemical Society* **119**, 7374-7380 (1997).
108. A. Stashans, S. Lunell, R. Bergström, A. Hagfeldt, S.-E. Lindquist, Theoretical study of lithium intercalation in rutile and anatase. *Physical Review B* **53**, 159 (1996).
109. M. E. Orazem, B. Tribollet, *Electrochemical impedance spectroscopy*. vol. 48. John Wiley & Sons **1**, 383-389 (2008).
110. J.-Y. Shin, J. H. Joo, D. Samuelis, J. Maier, Oxygen-Deficient $TiO_{2-\delta}$ Nanoparticles via Hydrogen Reduction for High Rate Capability Lithium Batteries. *Chemistry of Materials* **24**, 543-551 (2012).
111. C. Pfaffenhuber, M. Göbel, J. Popovic, J. Maier, Soggy-sand electrolytes: status and perspectives. *Physical Chemistry Chemical Physics* **15**, 18318-18335 (2013).
112. J. Maier, Concentration Polarization of Salt-Containing Liquid Electrolytes. *Advanced Functional Materials* **21**, 1448-1455 (2011).
113. P. Balaya, H. Li, L. Kienle, J. Maier, Fully Reversible Homogeneous and Heterogeneous Li Storage in RuO_2 with High Capacity. *Advanced Functional Materials* **13**, 621-625 (2003).
114. C. Xiao, H. Wang, R. Usiskin, P. A. van Aken, J. Maier, Unification of intercalation electrode and supercapacitor concepts: Lithium storage in titania films as a function of position. *Submitted* (2023).
115. K. Xu, Nonaqueous Liquid Electrolytes for Lithium-Based Rechargeable Batteries. *Chemical Reviews* **104**, 4303-4418 (2004).

116. K. Xu, Electrolytes and Interphases in Li-Ion Batteries and Beyond. *Chemical Reviews* **114**, 11503-11618 (2014).
117. C. Xiao, H. Wang, P. A. van Aken, R. Usiskin, J. Maier, Lithium storage in titania films as a function of position: unification of intercalation electrode and super-capacitor concepts. arXiv:2303.10284 (2023).
118. Y. Zhu, J. Maier, How to adequately describe full range intercalation – a two-sided approach. *Submitted* (2023).
119. C. Xiao, J. Maier, Resistance and Capacitance of Depletion layers: A frozen-equilibrium approach. *In preparation*.
120. C. Xiao, R. Usiskin, J. Maier, Cyclic voltammetry in batteries: Differences between liquid-state and solid-state storage. *In preparation*.
121. E. Kotomin, private communication.
122. N. A. Richter, S. Sicolo, S. V. Levchenko, J. Sauer, M. Scheffler, Concentration of vacancies at metal-oxide surfaces: Case study of MgO (100). *Physical review letters* **111**, 045502 (2013).

Acknowledgments

Throughout the past five years of my PhD study in Stuttgart, I have been fortunate to collaborate with numerous outstanding scientists and engage in a variety of captivating and demanding projects. The work presented in this thesis would not have been possible without the help, support and input of many great people.

First and foremost, I would like to show my sincere and heartfelt gratitude to my supervisor Prof. Joachim Maier not only for giving me the precious opportunity to receive education, perform research in such an outstanding research group and initiating the scientific concept of the project but also for directly supervising me. The valuable discussion always inspires me and contributes to the emergence of new ideas and strategies. I really enjoy the time to work with him.

I am also grateful to Prof. Oliver Clemens and Prof. Frank Gießelmann for reviewing my thesis and being on my examination committee.

I also would like to show my sincere appreciation to my early day-to-day supervisor Dr. Robert Usiskin, who has given me a lot of guidance and advice in this project. He has spent a lot of time and effort to discuss with me and teach me new knowledge and skills. Scientific discussion with Yuanshan Zhang, Dr. Chia-Chin Chen, Dr. Rotraut Merkle, Dr. Davide Moia is deeply appreciated. Their insightful comments are very helpful for the experiment design and result interpretation. I thank Dr. Masahiko Isobe for being my external advisor.

Special thanks go to Dr. Laifa Shen, Dr. Changbao Zhu, Dr. Feixiang Wu, Dr. Shuangqiang Chen and Dr. Chao Wu who taught me a lot of battery knowledge when I started my study in this group. Many thanks go to my colleagues, who assisted me in performing experiments when I started my project. First, I highly appreciate Dr. Simon Lorger for showing me the electrochemical

measurements. His valuable suggestions and discussions are acknowledged. Moreover, I would like to thank Dr. Laifa Shen for training me to prepare batteries. I also would like to thank Dr. Gints Kucinskis for discussing the measurements of thin films. Many colleagues in the family of Prof. Maier's group contributed in many ways to my study at the MPI, and many thanks go to them, especially my fellows Ya-Ru Wang, Mina Jung, Dr. Yuanye Huang, Dr. Giulia Raimondi, Dr. Kyungmi Lim, Dr. Markus Joos, Dr. Alessandro Senocrate, Dr. Andreas Münchinger, Dr. Torben Saatkamp, Dr. Maximilian Hödl, Dr. Simon Lorger, Dr. Reihaneh Zohourian, Dr. Pinar Kaya, Dr. Maximilian Schaube, Dr. Maryam Nojabaee. In addition, I am also grateful to Dr. Christian Berger, Dr. Gee Yeong Kim, Dr. Chuanhai Gan, Dr. Yue Zhu, Dr. Eugene Kotomin, Dr. Igor Moudrakovski, Dr. Nina Krainyukova, Dr. Klaus-Dieter Kreuer, Dr. Jelena Popovic-Neuber, Prof. Yan Yu, Dr. Yan Zhang, Dr. Xiaolan Kang and Dr. Yue Guo for their help. Thank you all for the inspiring environment and pleasant collaborations during the long or short overlaps we had in Stuttgart.

Many thanks go to the scientists and technical staff at the MPI. I am particularly grateful to Dr. Hongguang Wang, Dr. Julia Deuschle, Dr. Xu Chen, Dr. Vesna Srot, Peter Kopold and Prof. Peter van Aken for the extensive TEM-lamella Preparation, TEM measurements and discussions, Georg Cristiani and Dr. Gennady Logvenov for film deposition (MBE and PLD), Dr. Wolfgang Braun and Dr. Gideok Kim for the discussions about thin film deposition, Thomas Reindl and Marion Hagel for ALD, Dr. Hoier Helga and Armin Sorg for XRD measurement, Kathrin Küster for XRS measurement, Barbara Baum for sample cutting, Samir Hammoud for ICP measurement, Udo Klock for furnace and thermostat preparation, Annette Fuchs for SEM measurement and chemical purchase, Uwe Traub for IT support, Florian Kaiser for a lot of technical support. The complex and systematic experiments could not have been done without the numerous technical support from Florian Kaiser (e.g., building measurement cells, set ups etc.). I would like to show my sincere gratitude to him. I especially appreciate that Thomas Reindl spent time training me to deposit thin films by using ALD and measure the thickness of thin films by utilizing Stylus Profilometry in the beginning of my research.

The administrative support from Madeleine Burkhardt and Sofia Weiglein is deeply acknowledged. Furthermore, I want to thank Dr. Hans-Georg Libuda and Dr. Eva Benckiser for their kind help in

the IMPRS program. In addition, I feel so grateful to Birgit King who took care of my registration and visa in Germany.

Many special thanks go to the “Büsnauer” Mahjong and Poker team: Yuanshan Zhang, Jiawei Zhang, Yiran Liu, Xianzhe Zeng. I really enjoyed our Friday evening’s activities. I would like to thank my other colleagues and friends at the MPI during the past years: Xinglu Que, Dr. Haonan Huang, Dr. Xu Wu, Dr. Hao Chu, Dr. Qingyu He, Dr. Xiaoyang Duan, Liwen Feng, Dr. Shenghan Gao, Dr. Yang Wang, Dr. Qiang Wei, Dr. Dong Zhao, Dr. Ke Liao, Dr. Wenbin Rui, Dr. Xianxin Wu, Dr. Lichen Wang, Dr. Jianxiong Li, Jihua Gu, Runze Zhang, Sida Tian, Xuejiao Zhang, Chao Yang, Yu-Jung Wu, Gabriele Domaine, Dr. Sander Smink, Dr. Matteo Minola, and I also would like to thank my other friends in Stuttgart: Liyu Shi, Yang Xiao, Tian’ao Guo, Zezhao Chen, Ziyi Wang, Hanwen Chen, Tiyao Li, Shuo Wang, Qiwei Hu, Jiwei Sun, and Yanqiu Zhao. Thank you for all the great time we spent together in Germany. Especially, I thank Liyu Shi and Chuanhai Gan for the enjoyable gatherings at their beautiful home, where I had the opportunity to have the best Chinese food in Germany.

Last but not least, I would show my deepest gratitude to my family. Thank my parents for their support and love as always. My deep thanks go to my dear girlfriend Yue Ren, who always supports me with love and encouragement. They are my powerful backing all the time. This thesis is dedicated to you.

List of Publications

Preprints

1. **Xiao, C.**; Wang, H.; Usiskin, R.; van Aken, P.; Maier, J., Lithium Storage in Titania Films as a Function of Position: Unification of Intercalation Electrode and Supercapacitor Concepts, *under review* [arXiv preprint, arXiv:2303.10284].

2. **Xiao, C.**; Maier, J., Resistance and Capacitance of Depletion Layers: A Frozen-equilibrium Approach, *in preparation*.

3. **Xiao, C.**; Usiskin, R.; Maier, J., Cyclic Voltammetry in Batteries: Differences between Liquid-state and Solid-state Storage, *to be submitted*.

Journal Articles

4. **Xiao, C.**; Chen, C.-C.; Maier, J., Discrete Modeling of Ionic Space Charge Zones in Solids, *Physical Chemistry Chemical Physics* 2022, 24, 11945-11957.

5. **Xiao, C.**; Usiskin, R.; Maier, J., Passivation Layers in Lithium and Sodium Batteries: Potential Profiles, Stabilities, and Voltage Drops. *Advanced Functional Materials* 2021, 31 (25), 2100938.

6. **Xiao, C.**; Li, M.; Wang, B.; Liu, M.-F.; Shao, C.; Pan, H.; Lu, Y.; Xu, B.-B.; Li, S.; Zhan, D.; Jiang, Y.; Tang, R.; Liu, X. Y.; Cölfen, H., Total Morphosynthesis of Biomimetic Prismatic-type $CaCO_3$ Thin Films. *Nature Communications* 2017, 8 (1), 1398.

7. Liu, M.-F.; Lu, Z.; Zhang, Z.; **Xiao, C.**; Li, M.; Huang, Y.-X.; Liu, X. Y.; Jiang, Y., Correlations of crystal shape and lateral orientation in bioinspired $CaCO_3$ mineralization. *CrystEngComm* 2018, 20 (35), 5241-5248.

8. Wang, B.; Mao, L.-B.; Li, M.; Chen, Y.; Liu, M.-F.; **Xiao, C.**; Jiang, Y.; Wang, S.; Yu, S.-H.; Liu, X. Y.; Cölfen, H., Synergistic Effect of Granular Seed Substrates and Soluble Additives in Structural Control of Prismatic $CaCO_3$ Thin Films. *Langmuir* 2018, 34 (37), 11126-11138.